Sensitive and mutiplexed microRNA quantification using amplified time-gated Förster resonance energy transfer

Jingyue Xu

université PARIS-SACLAY

Sensitive and Mutiplexed MicroRNA Quantification Using Amplified Time-Gated Förster Resonance Energy Transfer

Thèse de doctorat de l'université Paris-Saclay

École doctorale n°575 :
electrical, optical, bio : physics and engineering (EOBE)
Spécialité de doctorat: Physique
Unité de recherche : Université Paris-Saclay, CEA, CNRS, Institute for Integrative Biology of the Cell (I2BC), 91198, Gif-sur-Yvette, France
Référent : Faculté des sciences d'Orsay

Thèse présentée et soutenue en visioconférence totale, le 23/07/2020, par

Jingyue XU

Composition du Jury

Philippe MINARD Professeur, Université Paris-Saclay	Président
Yolanda VIDA Professeur, University of Málaga	Rapporteur & Examinatrice
Cristian A. STRASSERT Professeur, University of Münster	Rapporteur & Examinateur
Xavier LE GUEVEL Chargé de recherche, Université Grenoble-Alpes	Examinateur
Niko HILDEBRANDT Professeur, Université Paris-Saclay	Directeur de thèse

Thèse de doctorat

NNT : 2020UPASS137

Acknowledgment

I would like to express my sincere gratitude to my supervisor Prof. Niko Hildebrandt, the "Captain FRET" of our NanoBioPhotonics group, who offered me the opportunity to join this family and provided me the freedom to explore in the "FRET world". His continuous scientific tuitions help me a lot when I faced the difficulties in research. But nothing was more grateful than his enthusiasm and perpetual energy, which not only motivated me in my study but also encouraged me a lot in my life. I appreciate all his contributions of time, ideas, and funding to my PhD in the last four years.

My sincere thanks to Prof. Yolanda Vida and Prof. Cristian A. Strassert for being the reviewers of my PhD thesis.

Many thanks to all my former and current members of the NanoBioPhotonics group for the free and happy working atmosphere. Special thanks to Dr. Xue Qiu and Dr. Jiajia Guo for their technical guidance and continuous encouragement; to Dr. Shashi Bhuckory for his translation of my abstract and altruistic helps in my life; to Vjona Cifliku for spending the last period of PhD and tough writing period with me together; to Dr. Monique Chan-Huot and Dr. Thomas Plénat for teaching me French.

I thank China Scholarship Council for the funding and supporting of my PhD fellowship.

I also want to thank my family and dear friends for their love and company. Without them, this work would have never been possible.

Last but not least, my deepest gratitude and respect go to all the medical staff in the world during this COVID-19 health crisis. Life will get better, world will get better.

List of publications

Original publications

1. J. Xu, J. Guo, N. Golob-Schwarzl, J. Haybaeck, X. Qiu, and N. Hildebrandt. Single-measurement multiplexed quantification of microRNAs from human tissue using catalytic hairpin assembly and Förster resonance energy transfer. ACS Sensors **2020**, 5, 1768–1776.

2. J. Xu, L. Francés-Soriano, J. Guo, T. Hallaj, X. Qiu, and N. Hildebrandt. Energy transfer with nanoparticles for in vitro diagnostics. In: W. Parak and N. Feliu, Editors: Frontiers of Nanoscience, Volume 16, Colloids for Nanobiotechnology. Elsevier **2020**.

3. X. Qiu, J. Xu, J. Guo, A. Yahia-Ammar, N.-I. Kapetanakis, I. Duroux-Richard, J.J. Unterluggauer, N. Golob-Schwarzl, C. Regeard, C. Uzan, S. Gouy, M. DuBow, J. Haybaeck, F. Apparailly, P. Busson, and N. Hildebrandt. Advanced microRNA-based cancer diagnostics using amplified time-gated FRET. Chemical Science **2018**, 9, 8046-8055.

4. X. Qiu, J. Guo, J. Xu, and N. Hildebrandt. Three-Dimensional FRET Multiplexing for DNA Quantification with Attomolar Detection Limits. The Journal of Physical Chemistry Letters **2018**, 9, 4379−4384.

Poster presentations

1. Jingyue XU, Xue Qiu, Jiajia Guo, Akram Yahia Ammar, Niko Hildebrandt. Sensitive and Specific Nucleic Acid Detection Based on Rolling Circle Amplification and Förster Resonance Energy Transfer. 15th Conference on Methods and Applications in Fluorescence (MAF 15). Bruges, Belgium, 2017.

Contents

1. Introduction

MicroRNAs (miRNAs) are involved in virtually all physiologic processes, including differentiation and proliferation, metabolism, hemostasis, apoptosis or inflammation. To date, more than 30,000 miRNAs have been discovered, of which more than 2,500 can be found in humans. Especially, the discovery of many different circulating miRNAs (in biofluids of patients, *e.g.*, serum, plasma, urine, cerebrospinal fluid, *etc.*) specific for cancers (breast, colorectal, esophageal, gastric, liver, lung, ovarian, pancreatic, *etc.*), as well as many other diseases (infectious disease, immunological disorder, cardiovascular disease, neurological disease, *etc.*), have strongly driven the implementation of miRNAs as next-generation biomarkers for prediction of the diseases, treatment response or prediction of progression. Based on a new report by BCC Research *Inc.*, the global market for miRNA research tools, services, diagnostics, and drug discovery is estimated to reach nearly $1.4 billion in 2021 at a compound annual growth rate of 10.5% for 2016-2021. Compared to the very recent discovery of circulating miRNAs, the diagnostic section of this overall market is still extremely small, demonstrating the urgent need for developing approved clinical miRNA diagnostics. Despite their short lengths combined with strong sequence similarities between different miRNAs, many different technologies have been used for their detection, in which the most commonly applied methods are reverse transcription quantitative polymerase chain reaction (RT-qPCR), microarrays, next-generation sequencing (NGS), in situ hybridization (ISH), and northern blotting (NB). However, the main limitations are low sensitivity (microarray, NB) and throughput (ISH, NB, RT-qPCR), expenditure of costs (microarray, NGS), lack of absolute quantification (microarray, NGS) and high-order multiplexing from a single sample (RT-qPCR, NGS), time consuming procedures, and difficulties associated with comparable results across different platforms. Isothermal amplification has emerged as a powerful method for highly rapid, specific and sensitive miRNA assays, which also possesses the compatibility with diversified detection platforms, such as fluorescence, electrochemistry, and colorimetry.

The aim of this thesis is to address new routes of miRNA diagnostic tools, taking the simplicity of a homogeneous immunoassay, the multiplexing capability of microarrays, the sensitivity of RT-qPCR, and the throughput capacity of NGS within one single diagnostic tool. The original concept is to combine the versatility and multiplexing capability of luminescent Tb complexes (LTCs)-based time-gated Förster resonance energy transfer (TG-FRET) measurement with isothermal amplification technology to design ultra-sensitive and/or multiplexed miRNA biosensors. LTCs have long been used as an energy transfer donor, and possess unique advantages for multiplexing detection due to their multiple, sharp, and distinct emission peaks, as well as long excited-state lifetimes compared to organic dyes and quantum dots (QDs). Organic dyes can be used in biological systems with low toxicity. They have been the most frequently applied fluorophores for FRET, and in combination with LTCs as donors, multiplexed biosensing approaches are capable based on LTCs-to-dyes FRET. Notably, appropriate spectral crosstalk correction needs to be taken for spectral multiplexing due to the broad emission profiles of the most organic dyes. While QDs have unique advantages over organic dyes in FRET systems, especially in LTCs donors-based FRET assays. QDs have better spectral overlap as well as larger Förster distance with LTCs owing to their very broad absorption and extremely high molar extinction coefficient and quantum yield. The narrow and size-tunable emission bands make QDs excellent FRET acceptor candidates for multiplexing. Traditional FRET measurements are hampered by short-lived (in the ns range) and high-background fluorescence from buffers or samples. It can be eliminated by using TG-FRET, especially using long-lived LTCs as donors and short-lived dyes/QDs as acceptors. Upon pulsed excitation of a sample, by collecting photoluminescence (PL) intensities in time windows much longer than the natural decay of the dyes/QDs, but still within the lifetime of the LTCs decay, the direct excitation of the acceptors dyes/QDs and any background autofluorescence can be efficiently suppressed, greatly simplifying analysis of the system.

The thesis can be divided into eight chapters. Following the introduction, the theoretical and practical background of the research, and three individual studies are presented, then completing by summary and outlook, appendix, and bibliography. Each study is corroborated with introduction, materials and methods, results and discussion, and conclusion.

In the first study, I present a miRNA detection assay using enzymatic rolling circle amplification (RCA)-amplified LTCs-to-dye TG-FRET. My contribution to this study was the analysis of the clinical samples, including sample preparation, RCA-FRET experiments, RT-qPCR experiments, and data analysis. Dr. Jiajia Guo also contributed in the experimental work, and Dr. Xue Qiu designed the study and wrote the manuscript. All authors contributed in editing and writing of the manuscript and approved its final version to the journal (X. Qiu, J. Xu, J. Guo, A. Yahia-Ammar, N.-I. Kapetanakis, I. Duroux-Richard, J.J. Unterluggauer, N. Golob-Schwarzl, C. Regeard, C. Uzan, S. Gouy, M. DuBow, J. Haybaeck, F. Apparailly, P. Busson, and N. Hildebrandt. *Chemical Science* **2018**, 9, 8046-8055. Third paper in Section **List of publication**). The combination of RCA with TG-FRET between LTCs donors and Cy5.5 acceptors resulted in single-nucleotide variant specificity and sensitivity with limit of detection (LOD) down to 4.2 ± 0.5 attomole (30 ± 3 fM) for miR-21, 6.8 ± 0.8 attomole (48 ± 5 fM) for miR-132, and 14 ± 2 attomole (99 ± 10 fM) for miR-146a. Quantification of miR-21 from human tissues and plasma samples revealed the relevance for breast and ovarian cancer diagnostics. Analysis of miR-132 and miR-146a from acute monocytic leukemia cells (THP-1 cells) demonstrated the broad applicability to different miRNAs and other types of clinical samples. Direct comparison to the gold standard RT-qPCR showed advantages of amplified TG-FRET concerning precision and specificity when quantifying low concentrations of miRNAs as required for diagnostic applications. The results demonstrate that a careful implementation of RCA and TG-FRET into one straightforward nucleic acid detection method can significantly advance the possibilities of miRNA-based cancer diagnostics and research.

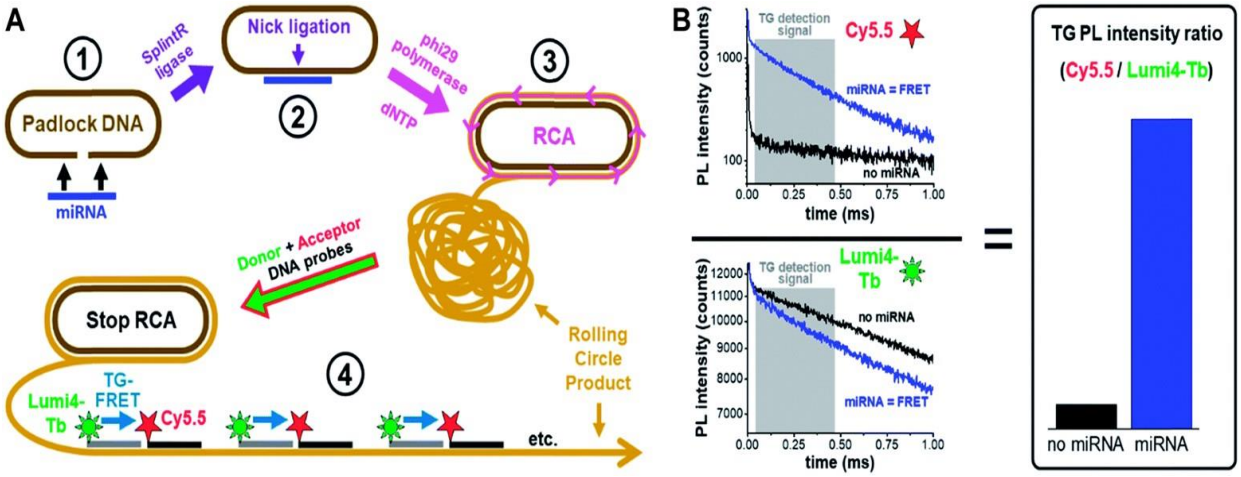

Figure 1.1 Schematic representation for miRNA detection assay using RCA-amplified LTCs-to-dye TG-FRET.

The second study presents a temporal multiplexing assay for miRNA detection assay using enzyme-free catalytic hairpin assembly (CHA)-amplified LTCs-to-dye TG-FRET. My contribution to this study was designing the study, performing experiments, analyzing the data, and writing the manuscript. Dr. Jiajia Guo and Dr. Xue Qiu also contributed in the study designing. All authors contributed in editing and writing of the manuscript and approved its final version to the journal (J. Xu, J. Guo, N. Golob-Schwarzl, J. Haybaeck, X. Qiu, and N. Hildebrandt. *ACS Sensors* **2020**, (accepted), DOI: 10.1021/acssensors.0c00432. First paper in **Section List of publication**). Implementing TG-FRET into CHA can be used for the simultaneous quantification of two miRNAs (miR-21 and miR-20a) with a single measurement from total RNA extracts of human tissues. A single LTCs-to-Cy5.5 FRET-pair was conjugated at two specific distances within target-specific CHA hairpin probes, such that each miRNA resulted in distinct amplified PL decays that could be distinguished and quantified by TG PL intensity detection. Enzyme-free amplification in a separation-free assay format and the absence of autofluorescence background allowed for simple, specific, and sensitive detection with LOD down to 380 ± 40 attomoles (2.7 ± 0.3 pM) for miR-21 and 250 ± 60 attomoles (1.8 ± 0.4 pM) for miR-20a. Reliable duplexed quantification of both miRNAs at low picomolar concentrations

was confirmed by analyzing total RNA extracts from different colon and rectum tissues with single and dual target CHA-TG-FRET and RT-qPCR for comparison. These rapid, simple and multiplexed miRNA biomarker assays present a capable method for clinical diagnostics.

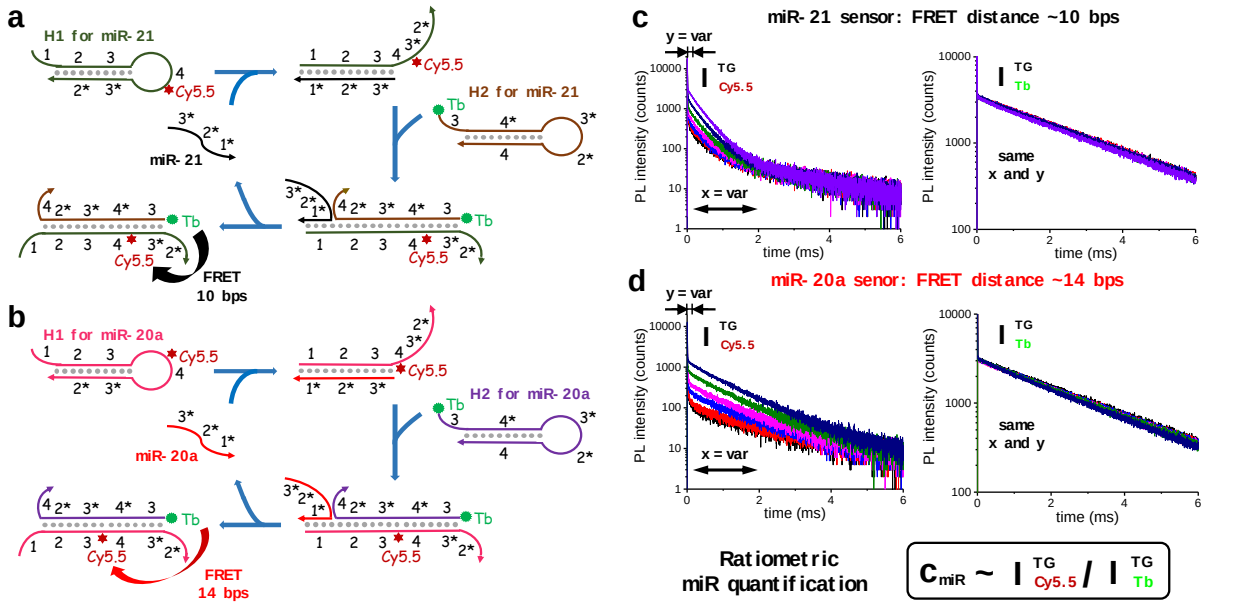

Figure 1.2 Schematic representation for multiplexed miRNAs (miR-21 and miR-20a) detection assay using CHA-amplified LTCs-to-dye TG-FRET.

In the third study, I investigated a miRNA detection assay using enzymatic hyperbranched rolling circle amplification (HRCA)-amplified LTCs-to-QD TG-FRET. My contribution to this study was designing the study, performing experiments, and analyzing the data. Dr. Xue Qiu also contributed in study design. The manuscript is under preparation. By integrating autofluorescence-suppressed TG measurement into HRCA with exponential amplification efficiency, it provides advantages of high sensitivity with a detection limit of 11 ± 4 attomole (80 ± 30 fM) and selectivity toward target miR-21 in extremely low background noise, quick and simple one-step assay format. Target-primed and reverse primer-initiated HRCA reaction can generate a large amount of single strand DNAs with different lengths (HRCA product). By hybridizing with Tb-labeled reporter DNA probes, and adaptor DNA probes that are on the surface of the QD *via* biotin and streptavidin

interaction, QD-DNA-LTCs complexes could from, inducing the shortened distance between LTCs, resulting in LTCs-to-QD FRET. Besides, the proposed assay shows great potential for broad applicability to different miRNAs and multiplexing capability, demonstrating that it can be a promising alternative to current miRNA diagnostic approaches.

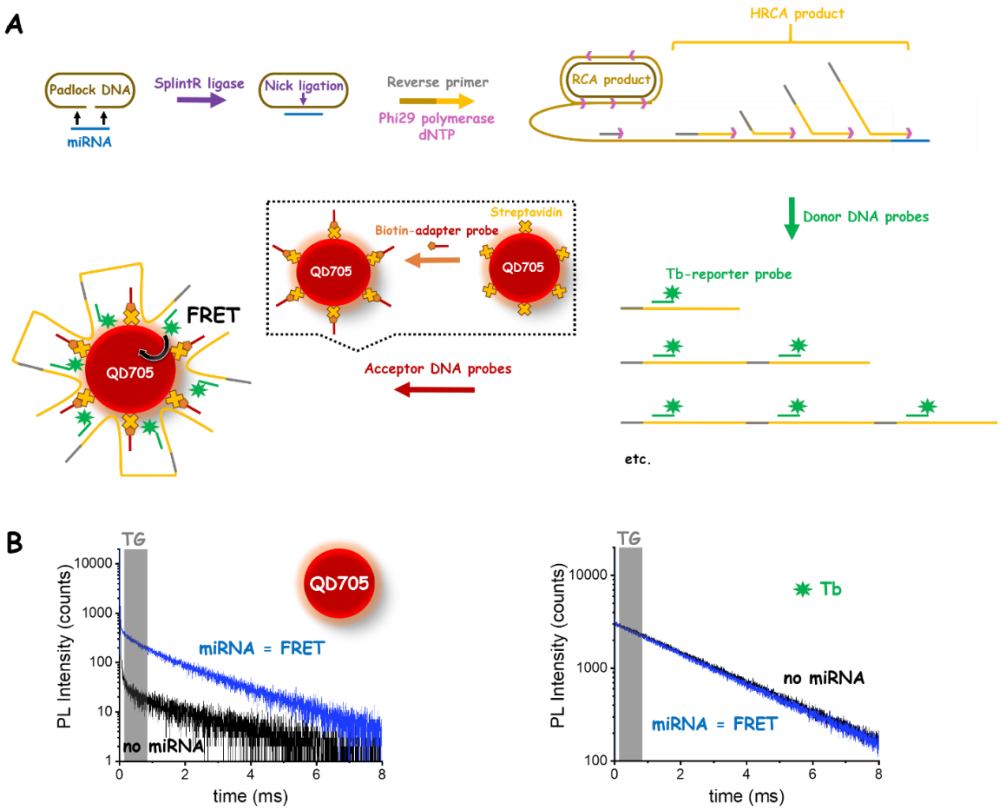

Figure 1.3 Schematic representation for miRNA detection assay using HRCA-amplified LTCs-to-QD TG-FRET.

2. Background

2.1 MiRNA biomarkers

MiRNAs are small (approximately 19-23 nucleotides) non-coding RNAs that were first discovered in the nematode *Caenorhabditis elegans* in 1993 [1]. The production of mature miRNA encompasses a great deal of RNA processing steps according to the biogenesis of miRNA [2-4]. The basic process of miRNA expression and maturation is outlined in **Figure 2.1**. MiRNA coding genes are generally transcribed in the nucleus producing large capped and polyadenylated primary miRNA transcript (pri-miRNA). The pri-miRNA sequence is cleaved by the Drosha-DGCR8 complex to produce a stem-loop hairpin structure precursor miRNA (pre-miRNA). This pre-miRNA is then transported to the cytoplasm by Exportin-5-Ran-GTP. In the cytoplasm, the RNase Dicer complex with the double-stranded RNA-binding protein TRBP cleaves the pre-miRNA hairpin to its mature length. The passenger strand (anti-sense strand) of the mature miRNA is degraded, whereas the functional strand (guide strand) is loaded together with Argonaute proteins (Ago) into the RNA-induced silencing complex (RISC), where it guides RISC to silence target mRNAs through mRNA cleavage, deadenylation or translational repression [2-5]. Acting as post-transcriptional regulators of gene expression [6], mature miRNAs can repress protein synthesis by binding to 3'-untranslated regions of mRNA and are involved in many biological processes, such as development, cell proliferation, differentiation, and apoptosis [7]. Therefore, miRNAs play an important role in the development and progression of cancer and various other diseases [8-10].

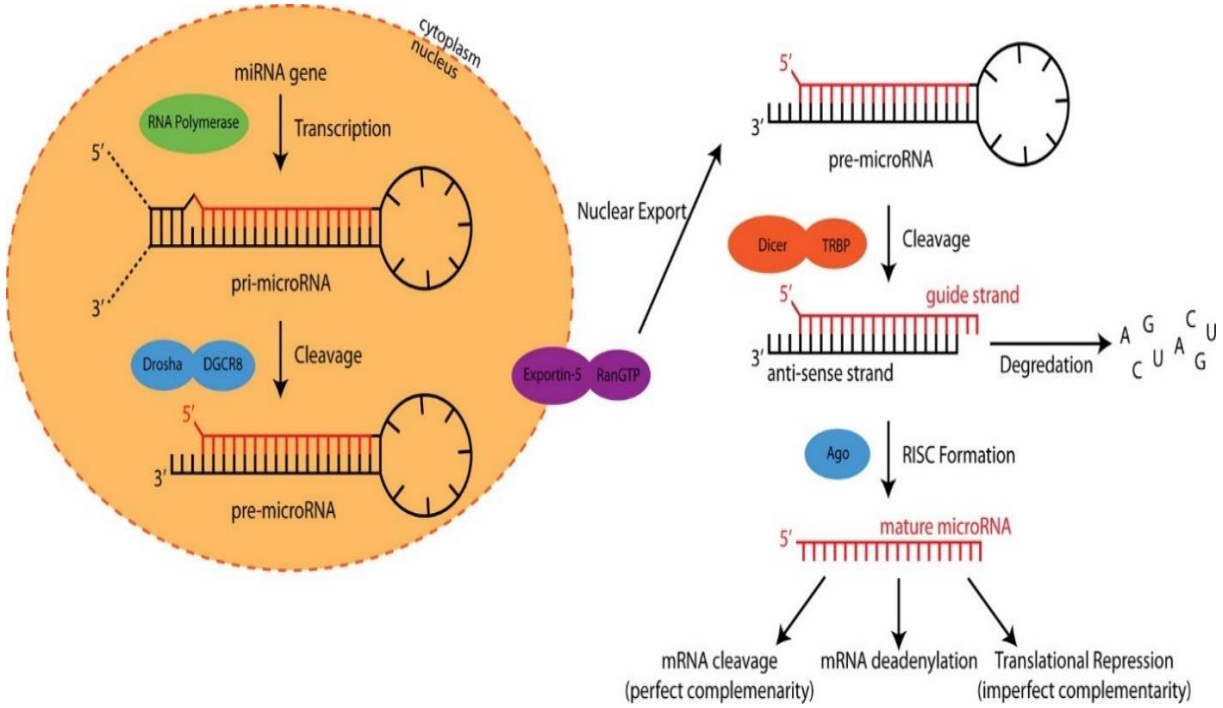

Figure 2.1 MiRNA biogenesis process starts with transcription in the nucleus and ends with affecting gene translation in the cytoplasm. (Reprinted with permission from reference [5]. Copyright 2016 American Chemical Society.)

Taking account into the cell-to-cell variations and complex stochastic nature of RNA expression in cells [11], considerable information connecting cell function and miRNA expression may be covered by cell population based miRNA analysis. Single-cells analysis and tissues/organs cells analysis are crucial for miRNA expression profiling to understand the involvement, functions and combinations of different miRNAs in disease development at cellular level [8, 12, 13]. Many miRNAs are identified as key regulators of various diseases via such analyses, which makes them very attractive therapeutic targets. Besides, analysis of extracellular miRNAs circulating in the blood and other biofluids, such as serum, urine and cerebrospinal fluid, is also highly relevant to the diagnosis of diseases. It is found that a large amount of circulating miRNAs derived from various tissues/organs are present in human serum and plasma in a remarkably stable form and are extremely resistant against endogenous RNases [14, 15]. One explanation of the stability of circulating miRNAs is

associated with RNA-binding proteins, such as nucleophosmin (NPM1) [16] and Argonaute2 (Ago2) [17]. Alternative explanation is that circulating miRNAs are contained within microvesicles (*e.g.*, exosomes, microparticles, and apoptotic bodies) and are protected from the membrane structure [18, 19]. For instance, exosomes, a sort of small membrane vesicles, have been reported to be abundant in plasma [20] and further have been revealed to contain miRNAs that can be released into body fluids such as blood and urine [21]. The possibility of direct detection in easily-accessible biofluid samples has opened up new clinical avenues for miRNAs to be used as next generation biomarkers for diagnosis and prognosis [13, 22-24].

2.1.1 MiRNA biomarkers for cancers/tumors

Human miRNAs appear to be frequently located at fragile sites or genomic regions related to cancers [25], and play important role in onset, progression, and metastasis of cancers [26]. The expression profiles of miRNAs differ between normal tissues and the tumors and differ between tumor types [27]. Many studies have shown the alterations of miRNA expression profiles in multiple cancers, including leukemia [28], breast cancer [29], lung cancer [30], ovarian cancer [31], prostate cancer [32], pancreatic cancer [33], liver cancer [34] and colorectal cancer [35]. Dysregulation of miRNAs in cancer can occur through epigenetic changes and genetic alterations, which can affect the production of the primary miRNA transcript, their processing to mature miRNAs and/or interactions with mRNA targets [27]. It is reported that the tumor-specific genetic defects in the miRNA biogenesis machinery, such as in the genes that encode TARBP2 [36], DICER1 [37, 38], Exportin-5 [39], DROSHA [40], DGCR8 [40] and AGO2 [40], are highly relevant to the cellular transformation and carcinogenesis/anti-carcinogenesis process in different tumor and cancer types.

MiRNAs can act as oncogenes as well as tumor suppressors [9, 41]. On one hand, miRNAs that function as oncogenes can facilitate tumorigenesis including proliferation, angiogenesis, invasion and migration [42]. For instance, miR-21, which locates in the chromosomal region 17q23.1, its increased expression is among the most frequently

associated with poor outcome in human cancer [43]. It has been shown that miR-21 can contribute to carcinogenesis through inhibition of apoptosis [44], or down-regulation of other tumor suppressors, such as phosphatase and tensin homolog [45], tropomyosin1 [46] and Sprouty2 [47]. Medina et al. found that the overexpression of miR-21 led to a pre-B malignant lymphoid-like phenotype *in vivo*, and when miR-21 was inactivated, the tumors regressed completely in a few days [48]. In addition, elevated expression levels of miR-21 have been found in a diverse subset of cancer cell lines and tissues (see **Table 2.1**). On the other hand, miRNAs that function as tumor suppressors can regulate the cell cycle, apoptosis, differentiation, DNA repair, angiogenesis, and metastasis [42]. For example, the let-7 family, which consists of 12 human homologues, was the first miRNA identified in humans [49]. Many human let-7 genes map to regions altered or deleted in human tumors, indicating that these genes may function as tumor suppressors [50]. The explanation for let-7 as a tumor suppressor is provided by the discovery that let-7 can regulate the expression of RAS oncogenes [51]. The RAS genes encode protein kinases that bind guanine nucleotides and are implicated in signal transduction processes [52]. About 20-30% of human tumors possess mutations in RAS genes, and approximately one-third of human lung adenocarcinomas carry RAS oncogenic mutations [52]. Besides, several studies show the tumor suppressor activity of let-7 encompasses other tumor types (see **Table 2.1**). Taken together, different or the same miRNAs can act as tumor suppressor or as oncogene in different kinds of cancers or tumors. **Table 2.1** summarizes several important miRNAs that are associated with human cancers/tumors. In view of these findings, differentially abundant miRNAs detected in blood [53], plasma [54, 55], serum [14], urine [56], cystic fluid [57], pancreatic juice [58], and sputum [59] samples have been proposed as candidate biomarkers of different types of cancer.

Table 2.1 Several important miRNAs that are associated with human cancers/tumors. (Adapted with permission from reference [52]. Copyright 2013 John Wiley and Sons.)

MiRNAs	Cancers/tumors association	Function
miR-21	colorectal, lung, breast, liver, stomach, and pancreatic cancers; chronic lymphocytic leukemia; neuroblastoma; glioblastoma; diffuse large B-cell lymphoma; acute myeloid leukemia; Hodgkin's lymphoma	oncogene
miR-17-92 cluster	breast, lung, colon, stomach, and pancreatic cancers; lymphomas	oncogene
miR-155	lung, breast, and colon cancers; chronic lymphocytic leukemia; B-cell lymphoma	oncogene
miR-221 and miR-222	chronic lymphocytic leukemia; thyroid carcinoma; hepatocellular carcinoma	oncogene
miR-372 and miR-373	testicular tumors	oncogene
let-7 family	lung, breast, colon, stomach, and ovarian cancers	tumor suppressor
miR-15a and miR-16-1	prostate cancer; chronic lymphocytic leukemia; multiple myelomas; pituitary adenomas	tumor suppressor
miR-29	lung and breast cancers; acute myeloid leukemia; chronic lymphocytic leukemia; cholangocarcinoma	tumor suppressor
miR-31	breast cancer	tumor suppressor
miR-34	colon, lung, breast, kidney, bladder, pancreatic, and liver cancers; neuroblastoma; melanoma	tumor suppressor
miR-126	colorectal, gastric, lung, prostate, bladder, and breast cancers	tumor suppressor
miR-145	breast and colon cancers	tumor suppressor
miR-203	hepatocellular and pancreatic tumors	tumor suppressor

2.1.2 MiRNA biomarkers for other diseases

In addition to cancers and tumors, miRNAs have shown to be associated with various diseases, including diabetes, neurological disorders and cardiovascular diseases.

In diabetic and pre-diabetic conditions, the miRNAs expression profiles are altered both in organs and in serum, consequently impairing insulin signaling, glucose, and lipid homeostasis [42]. The identification of specific miRNA signatures predicting the appearance of type 1 diabetes, type 2 diabetes, or their long-term complications would be very useful to permit the instauration of appropriate prevention strategies [52]. The expression of various serum miRNAs has been investigated in type 1 diabetes patients. As

a result, miR-152, miR-30a-5p, miR-181a, miR-24, miR-148a, miR-210, miR-27a, miR-29a, miR-26a, miR-27b, miR-25, and miR-200a are found to be upregulated in type 1 diabetes patients [60]. With regard to type 2 diabetes, studies revealed that serum miR-126 and serum miR-23a can be valuable biomarkers for pre-diabetes and early detection of type 2 diabetes [61, 62]. In addition, serum miRNAs such as miR-29a, miR-222, and miR-132 are proposed to be candidate biomarkers for predicting gestational diabetes mellitus [63].

MiRNAs are essential for the correct function of the nervous system, which has the broadest spectrum of miRNA expression of all human tissues. Around 70% of miRNAs are expressed in brain, and many of them are specific to neurons [64]. The brain-specific miR-9 and miR-134 are found to be involved in different aspects of neural development [65, 66]. Moreover, aberrant expression of miRNAs is associated with abnormal brain development and the pathogenesis of several neurodevelopmental diseases, such as Tourette's syndrome, Alzheimer's disease and Parkinson's disease [67]. For instance, low miR-107 expression is found in the cortex of Alzheimer's disease patients [68], and the expression levels of blood miR-1, miR-22*, and miR-29 can be useful biomarkers for Parkinson's disease [69].

MiRNAs have been found to be key regulators of cardiac development as well as multiple cardiovascular diseases [70]. MiRNAs are up or downregulated in vascular disease, heart failure, ischemic cardiomyopathy, dilated cardiomyopathy, and aortic stenosis [71, 72]. Since miRNAs in the systemic circulation may reflect tissue damage, circulating miRNAs such as miR-1, miR-208a, and miR-126 have been suggested as potential biomarkers for the acute myocardial infarction diagnosis [73-75].

Besides, miRNAs are used as biomarkers for the diagnosis of various other diseases. For example, circulating miR-122, miR-22, and miR-34a are found to be correlated with human immunodeficiency virus, and can serve as biomarkers for liver injury in human immunodeficiency virus patients [76]. Urinary miRNAs such as miR-1, miR-133, miR-223, and miR-199 are dysregulated in patients with autosomal-dominant polycystic kidney disease, and can be used as potential biomarkers of disease progression [77]. Plasma miR-122 is proposed as a biomarker for hepatic diseases [78]. In addition, circulating miR-323-3p is suggested as a biomarker for the diagnosis of ectopic pregnancy [79].

Taken together, understanding the functions of different individual and combined miRNAs, identifying disease-relevant signatures of miRNAs, and detecting them as biomarkers in tissues as well as in body fluids can be of paramount importance for both diagnostics and therapy of cancers or other diseases.

2.2 MiRNA detection methods

2.2.1 Introduction

As the clinical and biological implications of miRNAs have been sufficiently elucidated, it is of great significance to develop robust analytical technologies that facilitate routine miRNA detection. While owing to the unique characteristics of miRNA, such as small size, low abundance, sequence similarity, and their ability to regulate multiple targets, the progress in miRNA detection modalities meets many challenges and remains to be improved [6].

First, due to the small size as well as the GC content variation of miRNA, specific thermodynamic constraints should be taken into account, which can potentially introduces sequence-specific bias and significantly complicate the vast majority of hybridization-based, especially polymerase chain reaction (PCR)-based, detection methods [80]. Second, miRNAs are often expressed differing only by single nucleotides. The high sequence similarity among family members makes the specific detection more difficult. Third, miRNAs make up only a small fraction (roughly 0.01%) of the mass in total RNA extracted from a sample of interest, and miRNA concentration in cellular can be as low as a few molecules per cell [81]. The extremely low abundance of miRNA requires a highly sensitive assay. Moreover, the abundance of particular miRNA sequences varies by as much as four orders of magnitude from a few copies to over 50,000 copies per cell [82], thus, a wide dynamic range of miRNA detection is also a necessity. Importantly, beyond specificity, selectivity, and large dynamic range, another challenge is high-order multiplexing, whereby levels of more than one miRNA are quantitated simultaneously and from a single sample. Most mRNAs are regulated by one or more miRNAs [83], and further study revealed that

multiple miRNAs can target the same mRNA [84], adding complexity to the mechanisms through which miRNAs regulate gene expression. Hence, it requires methods to detect multiple miRNAs to fully understand the important and complex function of these regulation mechanisms.

Given the aforementioned analytical challenges, considerable effort has been continuously devoted to explore miRNA analysis strategies to meet the requirements for accuracy, sensitivity, specificity, high-throughput, and capacity to high-order multiplexing.

2.2.2 Conventional methods

At present, the major approaches used to analyze miRNAs are reverse transcription quantitative polymerase chain reaction (RT-qPCR), microarrays, next-generation sequencing (NGS), in situ hybridization (ISH), and northern blotting (NB).

RT-qPCR. As the current gold standard for miRNA analysis, there already exists some commercial assays and protocols, such as miRCURY LNA miRNA PCR Assays from QIAGEN, TaqMan Assays from Thermo Fisher Scientific, and Two-tailed miRNA Assays from TATAA Biocenter. As mentioned before, the small size of miRNA (roughly the same size as traditional primer) complicates most PCR-based detection schemes. To overcome this challenge, two strategies are most commonly used: (1) stem-loop RT-based miRNA assays using TaqMan probe; (2) poly (A) tailing-based and direct RT-based miRNA assays using SYBR green dye [85]. The overall workflow for both of these RT-qPCR approaches are illustrated in **Figure 2.2a**. The principle of these RT-qPCR methods mainly relies on reverse transcription of miRNA to complementary DNA (cDNA), followed by quantitative PCR with real-time monitoring of reaction product accumulation using either intercalating dye or TaqMan probe.

Microarray. Microarrays were among the first methods to be utilized for parallel analysis of large amounts of miRNAs, that rely on nucleic acid hybridization between target miRNAs and their corresponding complementary probes (**Figure 2.2b**). Several technical variations of the approach have been developed independently including the probe design, immobilization chemistry, sample labeling, and microarray chip signal detection methods [86]. GeneChip miRNA Array from Thermo Fisher Scientific is one of the well-known

platforms for studying the role of miRNAs and their involvement in a broad spectrum of developmental and physiological mechanisms.

NGS. The NGS technique has enabled another major approach for miRNA expression profiling, of which unique is the ability to identify novel miRNA sequences that are not already annotated in miRNA databases. The main NGS technologies have been reviewed [87]. Generally, NGS begins with the preparation of a small cDNA library from the miRNA sample of interest using a RT process similar to RT-qPCR. Adaptors are ligated to both the 5′ and 3′ ends of the cDNA products, and the resulting products are attached to either a planar or bead based substrate (**Figure 2.2c**). This is then followed by the massively parallel sequencing of millions of individual cDNA molecules from the library. Bioinformatic analysis of the sequence reads identifies both known and novel miRNAs in the data sets and provides relative quantification using a digital approach.

ISH. Since it was firstly used for miRNA detection in 2006 [88], ISH has become a common and unique technique for miRNA profiling which identifies the native locations of miRNA in a single cell, inside tissues, or in cell compartments. Depending on the detection method, ISH can be divided into chromogenic enzyme-based ISH and fluorescent ISH (FISH). Global miRNA expression analysis in tissues is typically performed with the help of chromogenic enzyme-based ISH detection methods, while for more precise small RNA localization studies, FISH imaging is more suitable [89]. Various approaches, including modification of hybridization probes, cell fixation and permeabilization, amplification of the target sequence and detection signal, enable the significant progress in single molecule RNA FISH techniques [89, 90].

NB. At present, NB for miRNA analysis is a readily available technology for molecular biology laboratories. Common protocol for NB involves miRNA isolation, polyacrylamide gel electrophoresis, transfer of the separated sample to the blotting membrane, and visualization via hybridization with a radioactively labeled DNA strand complementary to the miRNA of interest. As NB involves a size-based separation step, it can simultaneously detect both mature and precursor forms of a miRNA, which can be utilized for the studies on miRNA processing mechanisms [91].

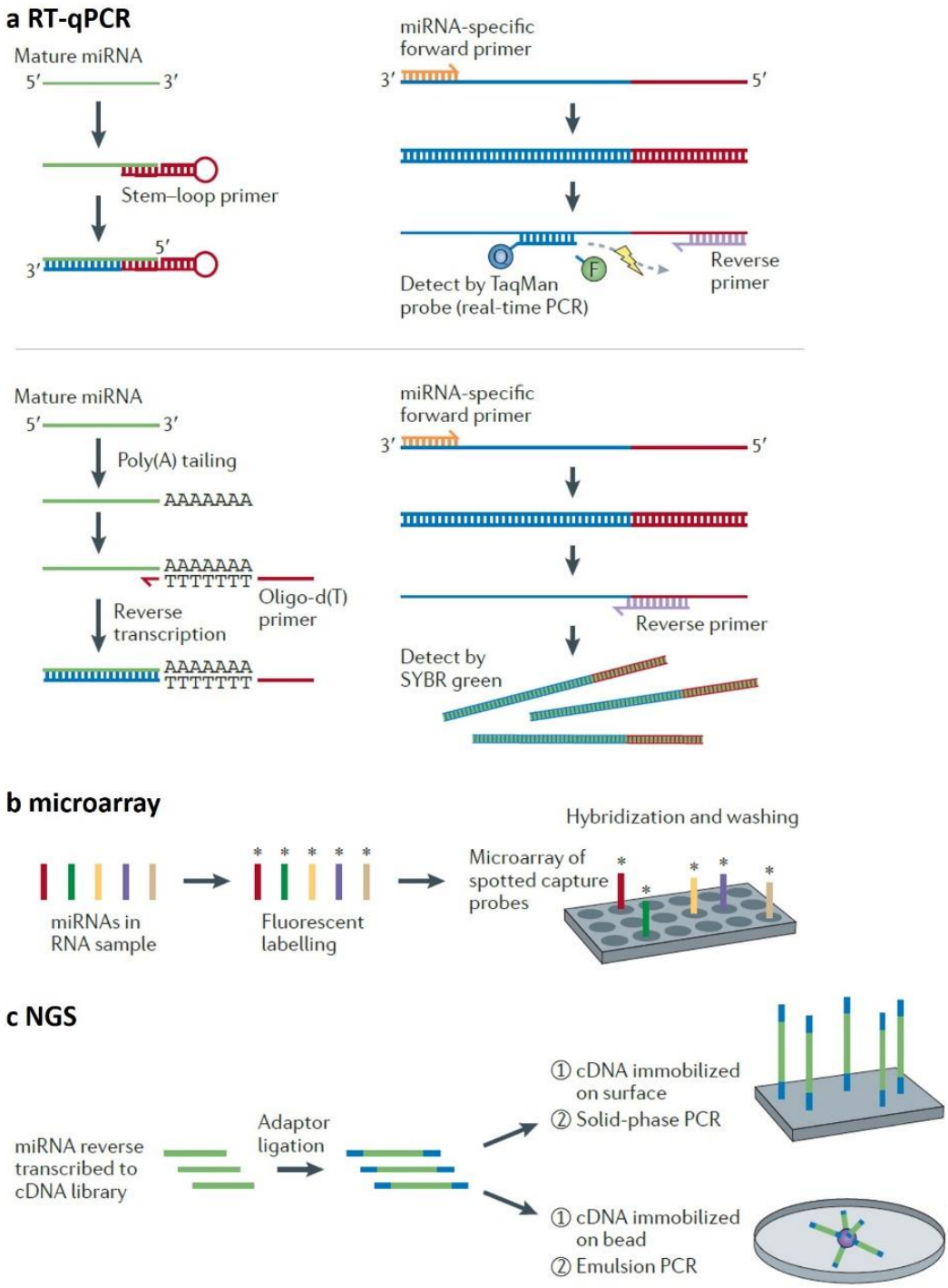

Figure 2.2 Schematic representation of major conventional methods for miRNA detection: **a.** reverse transcription quantitative polymerase chain reaction (RT-qPCR); **b.** microarray; **c.** next-generation sequencing (NGS). (Adapted with permission from reference [92]. Copyright 2012 Springer Nature.)

Recently, these conventional methods for miRNA detection were compared, and each method showed its strengths and weaknesses [86, 93] (**Table 2.2**). Owing to the high sensitivity, RT-qPCR and NGS are the most often applied approaches for detecting miRNAs, and have been used for commercial test. However, each method has limitations, such as low sensitivity (microarray, NB) and throughput (ISH, NB, RT-qPCR), expenditure of costs (microarray, NGS), specialized and expensive instruments (NGS, microarray, ISH), lack of absolute quantification (microarray, NGS) and high-order multiplexing from a single sample (RT-qPCR, NGS), time consuming procedures, and difficulties associated with comparable results across different platforms.

Table 2.2 Advantages and disadvantages of the conventional methods used to detect miRNAs. (Adapted with permission from reference [86]. Copyright 2019 Oxford University Press.)

Methods	Advantages	Disadvantages
RT-qPCR	- widely used for high sensitivity	- lack of multiplexing - biases and errors due to exponential amplification
microarray	- provides genome wide coverage - multiplexing capability	- low sensitivity - lack of absolute quantification - requires specialized instruments - requires specific probes - difficult data normalization - lack of reproducibility
NGS	- high sensitivity - provides genome-wide coverage - identifies novel miRNAs - identifies single nucleotide polymorphisms in miRNAs	- lack of absolute quantification - lack of multiplexing - requires specialized instruments - requires skilled bioinformatician - complicated data analysis
ISH	- spatiotemporal distribution in cells or tissue sections	- low throughput - requires specialized instruments - requires specialized skills - laborious - time consuming
NB	- detects non-amplified miRNAs	- low sensitivity - low throughput - requires many starting materials - laborious - time consuming - radioactivity

2.2.3 Isothermal amplification-based methods

Isothermal amplification has emerged as a powerful method for quantification of nucleic acids and has already proven its utility for developing highly specific and sensitive miRNA assays. Alternative to PCR methods that rely on the precise and complex thermocycling, isothermal amplification-based methods can rapidly and efficiently amplify the short target nucleic acids or the signal of a recognition event at constant temperature under simple conditions. Since the first isothermal amplification technique was introduced to detect miRNA [94], creative miRNA assays using isothermal amplification have been developed, achieving miRNA detection with high specificity (single-nucleotide resolution) and superior sensitivity (detection limit reaching femtomolar or attomolar level). Sequentially, these methods are demonstrated to be capable for miRNA quantification in clinical samples (tissues, serum, and plasma), and well suitable for miRNA in situ detection due to their mild reaction conditions and localized amplification ability [95]. A multitude of isothermal amplification techniques has been exploited. For instance, rolling circle amplification (RCA), duplex-specific nuclease signal amplification (DSNSA), loop-mediated isothermal amplification (LAMP), and strand-displacement amplification (SDA), that are mainly realized by enzyme-based replication or digestion. Besides, isothermal amplification can also be achieved via enzyme-free strand displacement processes, such as catalytic hairpin assembly (CHA) and hybridization chain reaction (HCR). **Table 2.3** summarizes the basic mechanism and **Figure 2.3** shows the schematic representation of these isothermal amplification-based methods for miRNA detection, respectively. The appealing attributes of isothermal amplification are: (1) the capability for rapid and high amplification (usually amplification efficiency of 10^3-10^6 within 3h); (2) the programmability allowing for construction of cascade amplification; (3) the compatibility with diversified detection platforms, such as fluorescence, electrochemistry, and colorimetry [95]. These advantages provide an excellent opportunity to build various sensitive and rapid bioassays for miRNA detection.

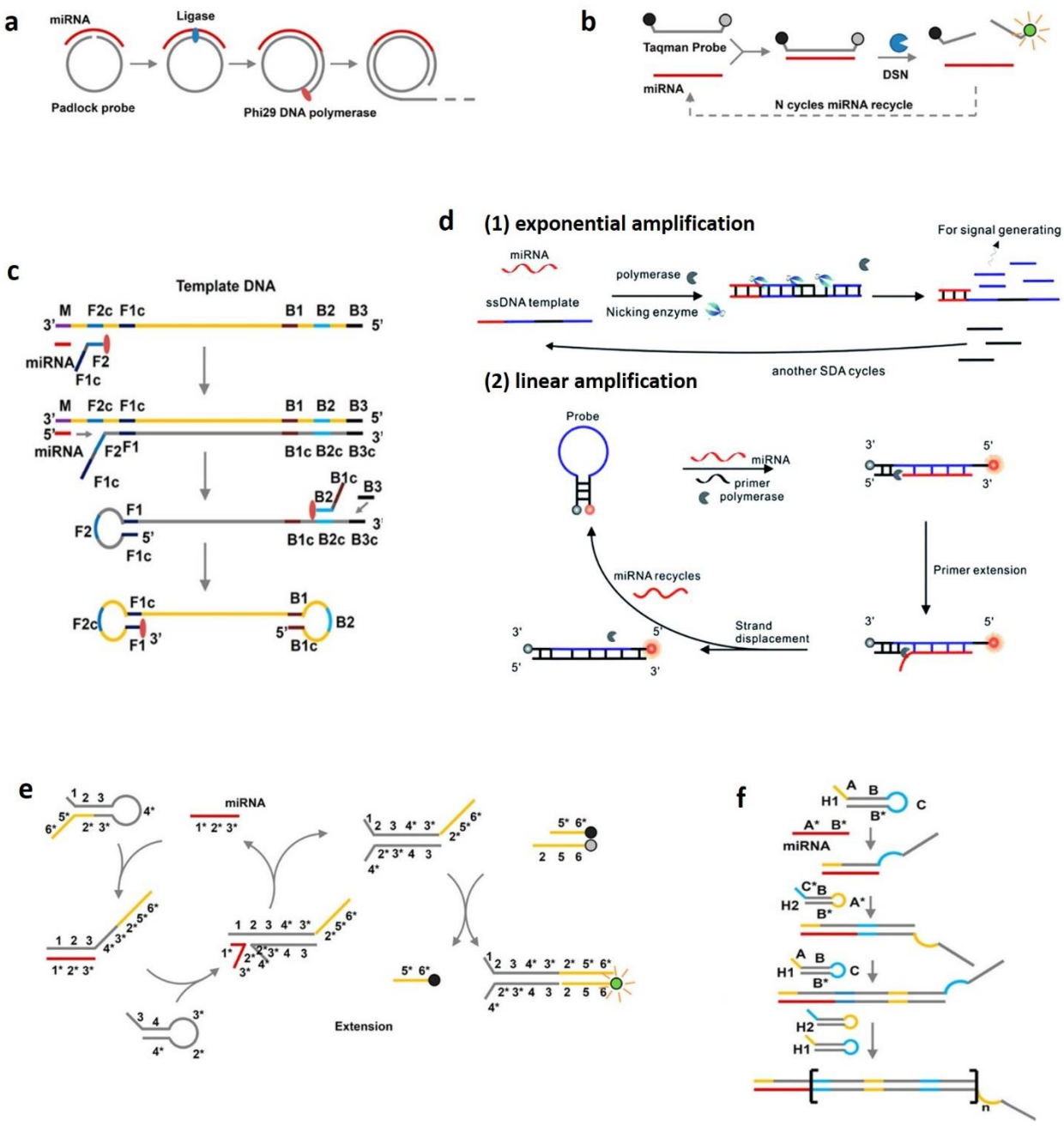

Figure 2.3 Schematic representation of isothermal amplification-based methods for miRNA detection: **a.** rolling circle amplification (RCA); **b.** duplex-specific nuclease signal amplification (DSNSA); **c.** loop-mediated isothermal amplification (LAMP); **d.** strand-displacement amplification (SDA); **e.** catalytic hairpin assembly (CHA); **f.** hybridization chain reaction (HCR). (Adapted with permission from reference [95]. Copyright 2017 American Chemical Society.)

Table 2.3 Summary of the isothermal amplification-based methods for miRNA detection. (Adapted with permission from reference [95]. Copyright 2017 American Chemical Society.)

Methods	Amplification mechanism	Enzyme	Role of miRNA	Linear or exponential amplification
RCA	polymerase extension, strand displacement	DNA polymerase, ligase	primer	both
DSNSA	cleaving DNA probe	duplex-specific nuclease	template	linear
LAMP	polymerase extension, strand displacement	DNA polymerase	primer	exponential
SDA	polymerase extension, strand displacement, nicking	DNA polymerase, nicking endonuclease	primer or initiator	both
CHA	strand displacement	enzyme-free	initiator	linear
HCR	strand displacement	enzyme-free	initiator	linear

RCA. In the 1990s, it was reported that DNA polymerase can utilize circular templates to make a long linear strand, containing multiple copies of a given sequence and this process was referred to as RCA [96, 97]. RCA can be coupled to the ligation of a padlock probe (in the presence of a target analyte) to provide sensitive detection of nucleic acids, and it was firstly used to detect miRNA in 2006 [98]. The padlock probe is a single probe that contains 3'- and 5'-end sequences that bind to target miRNA sequences in a juxtapose manner to aid a ligase-mediated circularization of the padlock probe if the 5'-end is phosphorylated. After circularization of the padlock probe, target miRNA (or an external primer) and DNA polymerase are used to produce long repeating DNA, which can generate amplification with high efficiency sequences (**Figure 2.3a**). Besides padlock probes, dumbbell probes-mediated RCA strategy is also widely used [99,100]. Subsequently, a target miRNA recycled RCA assay with specially designed dumbbell probe is proposed without utilization of ligases [101]. The dumbbell probe is already circularized but the primer-binding site is sequestered in the duplex region of the dumbbell. Upon target binding, the duplex region of dumbbell probe opens up to enable the primer to bind and the RCA process to begin.

In contrast to linear RCA techniques mentioned above, the proposal of exponential amplification method hyperbranched RCA (HRCA) leads to the sensitivity significantly

improved, which is reported that more than 10^9 copies of the circle can be produced within 90 min at approximately 60 °C [102]. The schematic representation of HRCA is shown in **Figure 2.4**. During the linear RCA process, the forward primer (usually the target miRNA) produces a multimeric ssDNA RCA product, which then becomes the template for the reverse primer. The DNA polymerase then extends the reverse primer, and during the extension process the downstream DNA is displaced to generate branching or a ramified DNA complex, which induces a discrete series of single-stranded DNA (ssDNA) or double-stranded DNA (dsDNA) fragments of various lengths comprising one or multiple units of the circular probe.

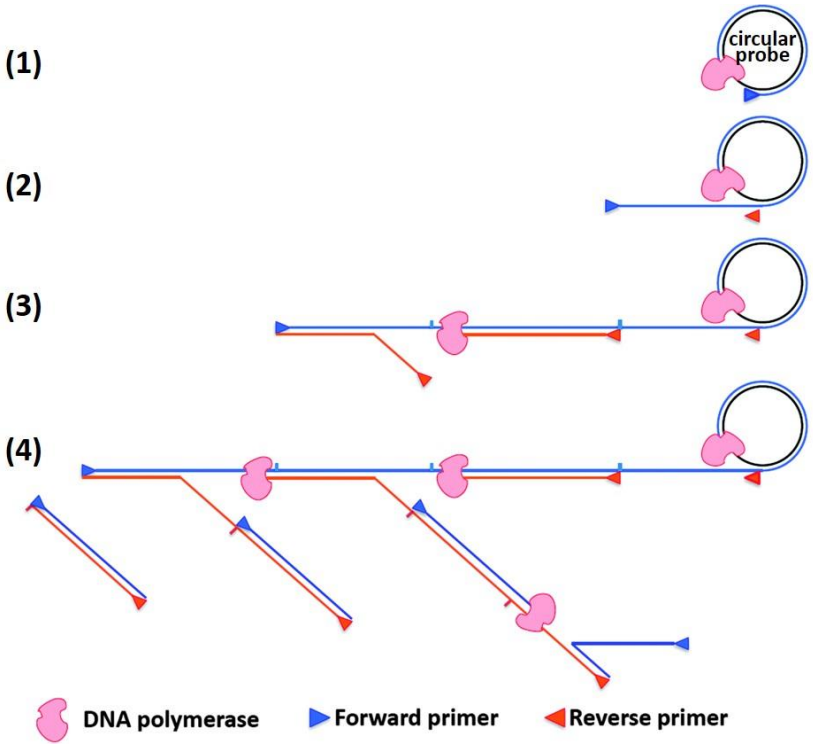

Figure 2.4 Schematic representation of HRCA strategy: (1) forward primer binds to ligated circular probe and is extended by DNA polymerase; (2) the continuous amplification generates a long ssDNA, which contains binding sites for reverse primer; (3) reverse primers bind to the long ssDNA and are extended by DNA polymerase; (4) the nascent ssDNA generated from reverse primer extension can also serve as templates to synthesize other primers. (Adapted with permission from reference [103]. Copyright 2014 The Royal Society of Chemistry.)

In most cases, target miRNA is generally used as the template for selective ligation of a padlock probe to generate the oligonucleotide circle. Due to the limited length of miRNA, mismatch between miRNA and ssDNA padlock, even if there is a mismatch of only one pair of bases, would lead to a significant decrease in melting temperature, which means an extremely low possibility of oligonucleotide circle generation and thus forbidden RCA [104]. In other words, using miRNA as a ligation template could provide improved specificity in miRNA assays and single-base differences between miRNAs have been correctly discriminated. Additionally, the exploitation of T4 RNA ligase 2 and SpintR ligase (*Chlorella* virus DNA ligase) leads to the higher selectivity and sensitivity than the commonly used T4 DNA ligase for RNA splinted DNA ligation [105-107]. RCA has been widely used in miRNA detection due to its high sensitivity and specificity.

DSNSA. Duplex specific nuclease is an enzyme that shows a strong preference for cleaving DNA in dsDNA or DNA-RNA hybrid duplexes with little activity against ssDNA or RNA, exhibits good capability to discriminate perfectly matched short DNA duplexes from non-perfectly matched ones [108]. By taking these particular properties of nuclease, DSNSA possesses an intrinsic advantage for miRNA assay. As shown in **Figure 2.3b**, DSNSA is achieved by the miRNA-mediated cycle of probe capturing, cleavage and fragment release. In typical DSNSA-based miRNA detection methods, target miRNAs can continuously capture specific DNA probes once they are released in reaction systems, no matter the probes are designed to be linear- or hairpin-structured [109], fluorophore-labeled or label-free [110]. Upon using differently labeled DNA probes, simultaneous detection of multiple miRNAs can be realized [111, 112]. Moreover, low error rates occur owing to the one-step amplification based on simple hybridization between the target miRNAs and probes.

LAMP. LAMP strategy was firstly introduced in 2000 [118], which exhibits great sensitivity as a result of its exponential amplification feature. As illustrated in **Figure 2.3c**, the LAMP system consists of a template DNA (M, F2c, F1c, B1, B2, B3), forward inner primer (F1c, F2), backward inner primer (B1c, B2) and outer primer B3. In the initial step, forward inner primer hybridizes to F2c in the template DNA and extends in the presence of DNA polymerase. Afterwards, target miRNA hybridizes to M in the template DNA and

initiates the extension along the DNA template and the strand displacement DNA synthesis with the help of DNA polymerase. Consequently, forward inner primer-linked ssDNA is released and forms a stem-loop structure at the 5'-end through the hybridization between F1 and F1c. At the 3'-end of this ssDNA, backward inner primer hybridizes to B2c to perform the primer extension and then the outer primer B3 hybridizes to B3c in the 3'-end of the ssDNA to perform the strand displacement DNA synthesis, releasing a backward inner primer-linked ssDNA, which can form dumbbell structures at 3'- and 5'-end, respectively. This auto-cycling strand displacement DNA synthesis can be repeated continuously and leads to exponential amplification of miRNA. LAMP can amplify a few copies of the target to 10^9 in less than one hour with high specificity [113].

However, the major disadvantages of LAMP strategy are the complicated design of primers for stem-loop formation, effected performance due to the synergistic hybridization and extension of the multiple primers along the long template, and the positive false signal caused by the indirect evaluation methods [114]. Though several new ideas have been put forward in order to overcome these shortcomings [115-117], there is still brilliant space for retrofitting primers and detection probes to adapt to the detecting requirement.

SDA. SDA is a kind of isothermal reaction, of which the mechanism relies on nicking, polymerase extension, and strand displacement. In terms of miRNA detection, two types of SDA strategies have been developed allowing for exponential and linear signal amplification (**Figure 2.3d**). In exponential amplification strategy, target miRNA works as a primer and hybridizes with a carefully designed ssDNA template. Once captured by the template, target miRNA is extended by DNA polymerase to generate one or more recognition sites for nicking enzyme, and the released DNA strands trigger a downstream detection signal. In some more complex cases, released DNA strands can be re-captured by the same or another ssDNA template, acting as primers to trigger another amplification SDA cycle. In linear amplification strategy, probe is designed as hairpin structure that the primer hybridization region is blocked in the stem region. The primer in the reaction solution can only be captured by probes that opened by target miRNA. Afterwards, a cycle

of miRNA-induced primer capturing, polymerase extension, and subsequent miRNA strand release are created, resulting in a linear amplification of the signal.

The commonly used polymerases in SDA are *Bst* DNA polymerase [118], Klenow fragment polymerase [119], and phi29 DNA polymerase [120], that have been widely reported to construct sensitive miRNA sensing platforms. However, the conventional utilization of enzymes hinders SDA from wider application because enzyme-mediated reactions are restricted by temperature, ionic composition, and other factors [114]. Hence, the developments of more transformational SDA methods are important.

CHA. Since originally developed in 2008 [121], CHA has received particular interest owing to its excellent property of enzyme-free signal amplification. As illustrated in **Figure 2.3e**, two complementary nucleic acid hairpins are designed and the reaction is inactivated in the absence of target. Only upon addition of the target miRNA which acts as initiator, one of the hairpins can be opened based on the toehold-mediated strand displacement, and then further enable the assembly of both hairpins to form double-stranded CHA product. Subsequently, the spontaneously displaced and recycled miRNA can act as a catalyst to induce more hairpin assembly events. However, the background signal caused by the nonspecific CHA products in the absence of target may counteract the specificity of signal amplification methodologies and compromise their analytical performance [122]. Aiming at this challenge, an improved CHA strategy is proposed by introducing mismatched base pairs into the breathing sites of the hairpin substrates [123]. This kind of mismatched CHA amplification significantly decreased the background reaction signal, which improved the properties of CHA-based biosensing strategies for miRNA detection [124-126].

CHA is a simple and nimble isothermal amplification method, which can be ascribed to its enzyme-free peculiarity. It avoids the disadvantages of enzymatic reactions, including particular reaction times and conditions to maintain the enzyme's activity. In addition, the cyclic utilization of the target miRNA during CHA procedure make designed biosensors achieve excellent sensitivity even in the low level of miRNA.

HCR. As another enzyme-free isothermal amplification method, the basic mechanism of HCR was firstly reported by Pierce and Dirks in 2004 [127]. As seen from **Figure 2.3f**, two species of hairpin DNA (H1, H2) are rationally designed, and one hairpin DNA (H1) comprises sequences complementary to the target miRNA and another hairpin DNA (H2). Only in the presence of initiator target miRNA, the hairpin structure of H1 can be opened, and then hybridize with H2, forming a nicked long double-stranded DNA structure to amplify the signal readout.

HCR shows great potential in biosensor because it can bind thousands of auxiliary hairpin probes to amplify signal [128]. What's more, the enzyme-free reaction eliminates the restrictions of enzyme-coupled methods. Nevertheless, deficiencies such as environmental sensitivity still need to be addressed for more extensive applications in clinical miRNA diagnostics.

2.3 Förster resonance energy transfer

Förster resonance energy transfer (FRET) is a well-established photophysical phenomenon, by which energy transfers from a donor molecule in excited state to an acceptor molecule in ground state over reasonable distances (typically 1-20 nm). Such energy transfer is a non-radiative process (without emission of photon) and is the result of dipole-dipole interactions between the donor and acceptor. If the donor-acceptor pair is correctly oriented and luminescence spectrum of the donor overlaps with the absorption spectrum of the acceptor, energy can be transferred leading to luminescence quenching of donor and emission from FRET-sensitized acceptor (when the acceptor is luminescent).

The discovery of the FRET phenomenon could be traced back to the beginning of the twentieth century [129, 130]. Afterwards in 1927, Jean Perrin [131] initially put forth a classical explanation of this phenomenon, and proposed the relationship between the dipole interactions and the transferred energy. Later in 1932, his son Francis Perrin [132] developed a corresponding quantum mechanical theory based on Kallmann's and London's results [133]. He recognized the influence of the spectral overlap between the emission

spectrum of donors and the absorption spectrum of acceptors on energy transfer efficiency. However, the relation between easily accessible spectroscopic data and theoretical equations was achieved by Theodor Förster [134-138]. By extending the Perrins' original ideas, he proposed a quantitative theory to describe the non-radiative energy transfer depending on the spectral overlap and the intermolecular distance that are still valid today thus enabling the possibility of many FRET applications in all kinds of natural sciences [139]. To date, FRET has become an outstanding tool for the study of intermolecular interactions with many applications in biological technologies, sensing, and conformational studies.

The discussion below presents some basic knowledge of mechanisms in terms of FRET theory (**Section 2.3.1**) and FRET measurement techniques (**Section 2.3.2**) that are mainly extracted from reference [140], and a short review of FRET-based applications in miRNA biosensing (**Section 2.3.3**).

2.3.1 FRET theory

The basic principle of FRET can be described in the Jablonski diagram. As illustrated in **Figure 2.5**, the donor and acceptor possess several different electronic states, and the energy transfer only happens when they share the same electronic transition (red, green and purple line). It takes place from the state in which the donor is excited (D*) to a state in which the acceptor is excited (A*), where an electronic transition from a higher to a lower energy level in donor leads to an electronic transition from a lower to a higher energy level in acceptor. Thus the shared electronic transition, the spectral overlap between donor emission and acceptor absorbance in terms of spectroscopy, is an indispensable condition for FRET. In addition, due to the dipole-dipole interaction, the distance between donor and acceptor must be close but not too close. In fact, this dipole-dipole coupling should be dominant at the usually considered FRET distance range of approximately 1-20 nm, where orbital overlap-related mechanisms (for very short distances) and radiative mechanisms (for long distances) play minor roles [140].

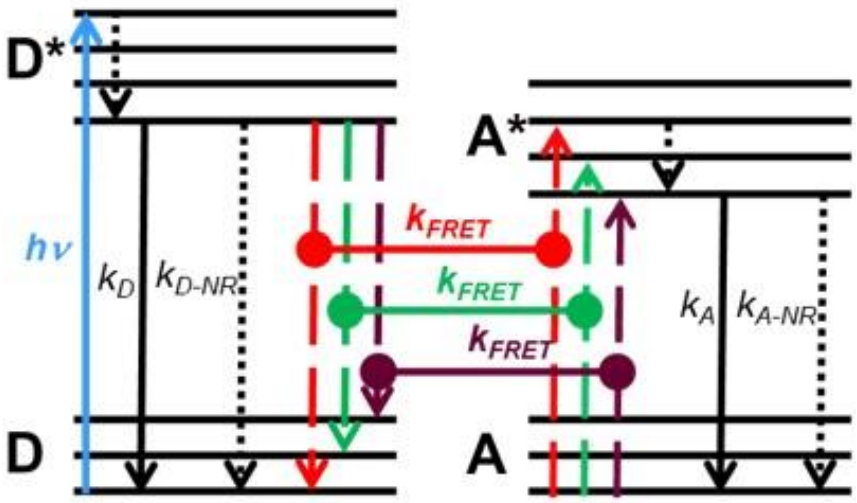

Figure 2.5 Basic FRET principle described in simplified energy level scheme (Jablonski diagram). The donor is excited (*hv*) from an electronic ground state (D) to an excited state (D*), then goes to an excited electronic ground state by inner relaxation (dotted arrow), then goes to ground state by radiative decay (k_D), non-radiative decay ($k_{D\text{-}NR}$) or FRET (k_{FRET}). The FRET process from D* to A* occurs when they share the same electronic transition (the difference between the respective energy levels need to be equal, vertical dashed lines in red, green and purple color). After FRET, the acceptor is in an excited state (A*), followed by radiative decay (k_A) or non-radiative decay ($k_{A\text{-}NR}$) to its ground state (A). (Adapted with permission from reference [140]. Copyright 2013 The Wiley-VCH Verlag GmbH & Co. KGaA.)

The FRET rate (k_{FRET}) can be described as following **Equation 2.1**:

$$k_{FRET} = \frac{9(\ln 10)\kappa^2 \Phi_D}{128\pi^5 N_A n^4 \tau_D r^6} J(\lambda) \qquad (2.1)$$

where κ^2 is the orientation factor of coupled donor and acceptor transition dipole moments, Φ_D is the luminescence quantum yield of donor in absence of energy transfer, N_A is Avogadro's number (6.023×10^{23} mol^{-1}), n is the refractive index of the medium, τ_D is the luminescence lifetime of donor (in the absence of acceptor), r is the distance between donor and acceptor, and $J(\lambda)$ is the spectral overlap integral between the donor emission and acceptor absorption defined in wavelength scale.

When the k_{FRET} and other decay rates are in equilibrium ($k_{FRET} = k_D + k_{D-NR} = \tau_D^{-1}$), and the FRET efficiency (η_{FRET}) is 50% at a distance r, this distance is commonly referred as Förster distance R_0, which can be calculated by replacing k_{FRET} with τ_D^{-1} and r with R_0 in **Equation 2.2**:

$$R_0 = \left(\frac{9(\ln 10)\kappa^2\Phi_D}{128\pi^5 N_A n^4} J(\lambda)\right)^{1/6} = 0.02108\left(\kappa^2\Phi_D n^{-4} J(\lambda)\right)^{1/6} \text{ nm} \qquad (2.2)$$

The spectral overlap integral $J(\lambda)$ describes the degree of energetic resonance between donor and acceptor (**Figure 2.6**), which is accessible with precise spectroscopy measurements and is given by **Equation 2.3**:

$$J = \int \bar{I}_D(\lambda)\, \varepsilon_A(\lambda)\, \lambda^4 d\lambda \qquad (2.3)$$

where $\varepsilon_A(\lambda)$ is the acceptor extinction coefficient (or molar absorptivity) spectrum, $\bar{I}_D(\lambda)$ is the donor emission spectrum normalized to unity and is given by **Equation 2.4**:

$$\int \bar{I}_D(\lambda)\, d\lambda = 1 \qquad (2.4)$$

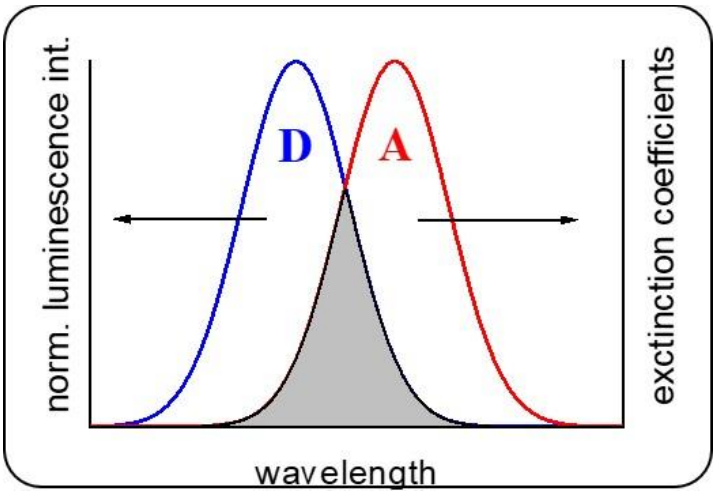

Figure 2.6 The overlap (gray area) of the area normalized emission spectrum of donor (D) (*cf.* **Equation 2.4**) and the extinction coefficient spectrum of acceptor (A) ε_A defines the overlap integral J (*cf.* **Equation 2.3**). (Adapted with permission from reference [140]. Copyright 2013 The Wiley-VCH Verlag GmbH & Co. KGaA.)

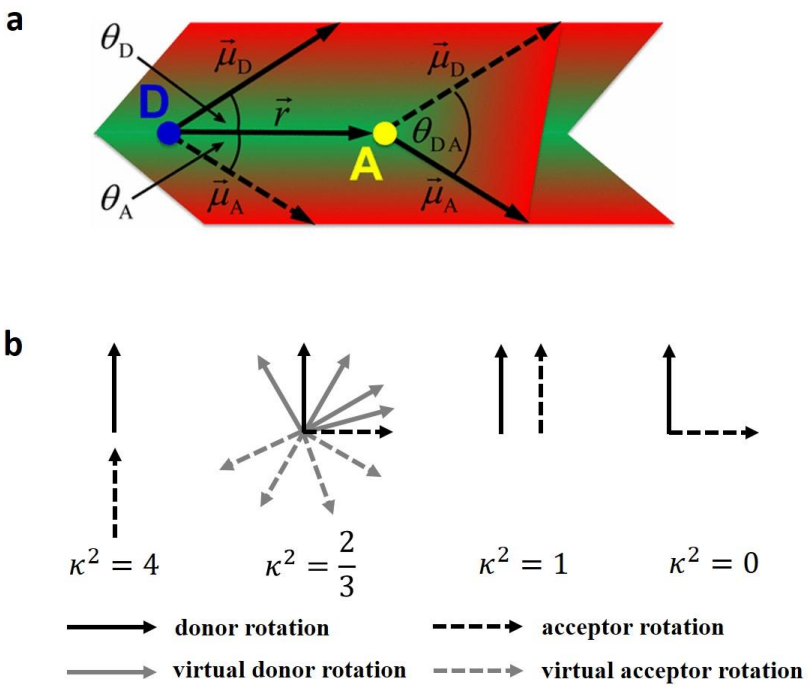

Figure 2.7 a. The orientation of donor emission transition dipole moment $\vec{\mu}_D$, the orientation of acceptor absorption transition dipole moment $\vec{\mu}_A$, and connection vector $\vec{r}$. (Adapted with permission from reference [141]. Copyright 2016 American Chemical Society.); **b.** The possible virtual orientations of donor and acceptor transition dipole moments and the corresponding κ^2. (Adapted with permission from reference [142]. Copyright 2015 MDPI.)

In addition, another important variable for FRET is the orientation factor κ^2 (in **Equation 2.1** and **Equation 2.2**). **Figure 2.7a** describes the orientation of the donor and acceptor dipole moments within the basic concept of FRET. With the different angles between the transition dipole moments of donor ($\vec{\mu}_D$) and acceptor ($\vec{\mu}_A$) and the connection vector between them ($\vec{r}$), κ^2 can be calculated as following **Equation 2.5**:

$$\kappa^2 = [\hat{\mu}_D \cdot \hat{\mu}_A - 3(\hat{\mu}_D \cdot \hat{r})(\hat{\mu}_A \cdot \hat{r})]^2 = (\cos\theta_{DA} - 3\cos\theta_D \cos\theta_A)^2 \qquad (2.5)$$

where $\hat{\mu}_D$, $\hat{\mu}_A$, and $\hat{r}$ represent the unit vectors of $\vec{\mu}_D$, $\vec{\mu}_A$, and $\vec{r}$, respectively, θ_{DA} is the angle between the donor and acceptor transition dipole moments ($\vec{\mu}_D$ and $\vec{\mu}_A$), θ_D and θ_A are the angles between the respective dipole moments and the donor-acceptor connection vector ($\vec{\mu}_D$ and $\vec{r}$, $\vec{\mu}_A$ and $\vec{r}$).

According to the **Equation 2.5**, κ^2 can range from 0 to 4 depending on the relative orientation of donor and acceptor transition dipole moments. As illustrated in **Figure 2.7b** [142], κ^2 can be 4 for head-to-tail parallel transition dipole moments, 1 for the parallel transition dipole moments, and $\kappa^2 = 0$ can occur for the perpendicular orientation. Often, $\kappa^2 = 2/3$ is assumed to be a good approximation and is used for many practical FRET application [140]. When both donor and acceptor can take any possible orientation during the FRET time ($1/k_{FRET}$), which means that the average rotation rate is much larger than the average FRET rate ($k_{rotation} \gg k_{FRET}$), the system is in a dynamic averaging regime and κ^2 becomes $2/3$. Even if one of the FRET pair shows average orientation and the other has a fixed orientation, then κ^2 can take values between $1/3$ and $4/3$, for which $2/3$ is still a decent approximation.

Taking **Equation 2.1** and **Equation 2.2** allows to the relation between the FRET rate (k_{FRET}), the luminescence decay time of donor (τ_D), and the donor-acceptor distance (r). As described in **Equation 2.6**, k_{FRET} is inverse sixth power distance dependent (r^{-6}):

$$k_{FRET} = \tau_D^{-1} \left(\frac{R_0}{r}\right)^6 \tag{2.6}$$

Then the FRET efficiency (η_{FRET}) can be given by **Equation 2.7**:

$$\eta_{FRET} = \frac{k_{FRET}}{k_{FRET}+k_D+k_{D-NR}} = \frac{k_{FRET}}{k_{FRET}+\tau_D^{-1}} = \frac{1}{1+(r/R_0)^6} = \frac{R_0^6}{R_0^6+r^6} \tag{2.7}$$

As shown in **Figure 2.8**, due to the r^{-6} distance dependency, FRET efficiency is mostly sensitive in the region of 0.5 R_0 to 2.0 R_0 (gray area). Beyond this range, FRET is either too efficient for shorter distances or negligible for longer distances.

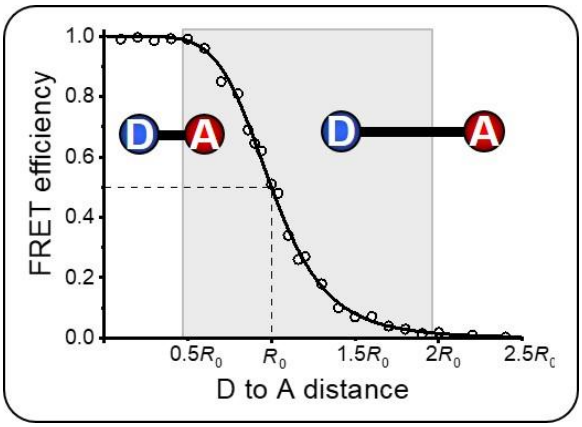

Figure 2.8 FRET efficiency as a function of donor (D) to acceptor (A) distance (*cf.* **Equation 2.7**). (Adapted with permission from reference [140]. Copyright 2013 The Wiley-VCH Verlag GmbH & Co. KGaA.)

As FRET is a deactivation process of the excited donor, the photophysical properties of the donor change in the FRET process. Thus, in terms of different spectroscopy, FRET efficiency (η_{FRET}) can be determined by measuring the luminescence intensity (I), or luminescence decay time (τ), or quantum yield (Φ) of the donor in the presence (I_{DA}, τ_{DA}, Φ_{DA}) and in the absence of the acceptor (I_D, τ_D, Φ_D), respectively (**Equation 2.8**).

$$\eta_{FRET} = 1 - \frac{I_{DA}}{I_D} = 1 - \frac{\tau_{DA}}{\tau_D} = 1 - \frac{\Phi_{DA}}{\Phi_D} \tag{2.8}$$

In summary, an effective FRET depends on several factors that must be carefully taken into account before thinking about an application of FRET:

(i) Spectral overlap integral $J(\lambda)$: the donor emission spectrum must overlap with the acceptor.absorption spectrum.

(ii) Distance between FRET pair r: due to the strong distance dependence (r^{-6}) of FRET efficiency, a slight modification of r can induce a significant change on FRET signals in the range of 0.5 R_0 to 2.0 R_0. The distance r should be neither too far nor too close (*ca.* 1-20 nm).

(iii) The orientation factor κ^2: the donor emission dipole moment, the acceptor absorption dipole moment, and their separation vectors must be in favorable mutual orientation. κ^2 is usually assumed to be $2/3$, which is the average value integrated over all possible angles for freely rotating attached-lumiphores.

2.3.2 FRET measurements

Although FRET itself is non-radiative, luminescence is always involved in FRET. In order to determine the FRET efficiency and FRET distance, emission changes of donor and acceptor (in case it is luminescent) must be measured. Luminescence can be measured by steady-state and time-resolved techniques, and time-resolved techniques can be divided into time-domain and frequency-domain methods. This section gives a short overview of these FRET measurement techniques in terms of luminescence spectroscopy.

Steady-state FRET measurements. Steady-state luminescence spectroscopy measures emission spectra (emission intensity of the luminophores as a function of wavelength over their entire time period of emission). It is achieved by exciting the luminophores at a fixed wavelength, and then scanning over the wavelength of their emission, which is then detected in selected wavelength intervals. In FRET experiments, steady-state measurement offers the advantage that both donor and acceptor can be measured at the same time within the same sample. Luminescence intensities (I_D, I_{DA}, I_A, I_{AD},) can be extracted from the measured overall spectrum and used for the calculation of FRET efficiency and distance. However, as the measured overall spectrum contains both donor and acceptor emissions, the spectral crosstalk between them should be taken into account. Moreover, autofluorescence from the sample medium, sample scattering and reabsorption (inner filter effects), and low signal-to-noise ratios are common sources of error that require an adequate correction.

Time-resolved FRET measurements. Time-resolved luminescence spectroscopy measures time-dependent luminescence intensity, which can be divided into time-domain method and frequency-domain method. Time-domain method uses a short excitation pulse of light, usually in the nanosecond range for lasers up to microsecond range for flash lamps. The excitation pulse is ideally much shorter than the decay time of the sample. Frequency-domain method uses intensity-modulated excitation light, the emitted light will follow this modulation frequency with a time delay called phase shift or phase angle (ϕ). The modulation frequency is typically in the same range as the reciprocal of the luminescence decay time of the sample. Both methods can be used to determine luminescence decay times,

Figure 2.9 shows the typical examples of measurements, respectively. Compared to frequency-domain method, time-domain method permits visualization of the luminescence decay and provides straightforward dynamic information.

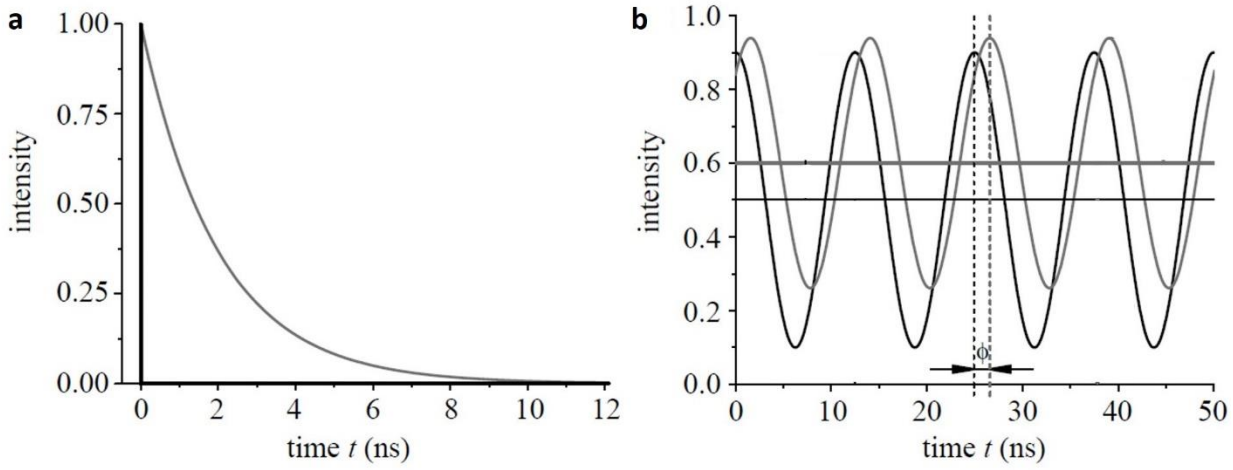

Figure 2.9 Typical examples of two time-resolved measurements for the determination of luminescence decay times. **a.** Time-domain measurement; **b.** Frequency-domain measurement. Excitation is displayed in black, emission with a decay time is displayed in grey. (Adapted with permission from reference [140]. Copyright 2013 The Wiley-VCH Verlag GmbH & Co. KGaA.)

In time-domain methods, the mathematical description of luminescence decay (with i decay times) is the luminescence intensity as a function of time (**Equation 2.9**):

$$I = \sum_i A_i \ exp\ (-t/\ \tau_i) \tag{2.9}$$

where I is the time-resolved luminescence intensity, A_i is the amplitude of a certain lifetime τ_i. The lifetime can be determined by fitting the data into the assumed decay models. With the calculated lifetimes, FRET efficiencies and distances can be determined. Steady-state measurement provides an average representation of the luminescence emission while time-resolved measurement shows dynamic information, which is particularly useful for biological molecule studies and cellular imaging (*e.g.*, Fluorescence Lifetime Imaging Microscopy-FLIM) [143]. In contrast with intensity based methods, fluorescence lifetime is independent of concentration, sample absorption and excitation intensity. Moreover, the

utilization of donors with long decay times (*e.g.*, lanthanide complexes) and acceptors (*e.g.*, organic dyes) with short decay times ($\tau_A \ll \tau_D$) allows the replacement of τ_{DA} by τ_{AD} in **Equation 2.8**, and both quenched donor emission and sensitized acceptor emission can be used for FRET analysis. Especially, the analysis with FRET-sensitized acceptor emission can get rid of the pure donor emission, and therefore decrease the background signal (non-FRET signal).

In this work, time-domain based time-resolved FRET measurements using lanthanide complexes (**Section 2.4**) as donors and fluorescent dyes (**Section 2.5**) and QDs (**Section 2.6**) as acceptors were mainly employed.

2.3.3 FRET application in miRNA detection

Due to the strong distance dependence in the biological interaction range (1-20 nm), FRET has been widely utilized as a "Spectroscopic Nano-Ruler" to monitor changes and interactions in biological systems, such as molecular interactions among proteins and nucleic acids, as well as their folding dynamics and conformational changes [144]. According to the aforementioned detection strategies in **Section 2.2**, FRET has been applied in miRNA detection as it is a common approach to facilitate "on/off" detection schemes, in which the FRET signal is "off" when the target is absence and "on" when the target is present (or vice versa). Strategies are usually based on the specific hybridization of complementary nucleic acids probes [145]. Molecular beacons (MBs) and binary probes (BPs) are two very common hybridization probes that are designed based on well-established photophysical principles to generate sequence-specific FRET signal in nucleic acids detection [146].

Standard MBs contain a single-stranded oligonucleotide with an acceptor and a donor attached at their opposite ends (**Figure 2.10a**). The central sequence of this oligonucleotide (loop) is complementary to a specific target. Five or six bases are attached at each end of the oligonucleotide (stem) in order to form Watson-Crick base pairs that force the acceptor and donor to be in close proximity, resulting in the FRET-sensitized acceptor emission. Only the presence of the target prompts the hybridization of the MB to the target, leading

to the open conformation of the MB. Consequently, the acceptor and the donor are spatially separated, which produces a fluorescence signal from the donor.

In standard BPs, a donor and an acceptor are attached to the ends of two single-stranded oligonucleotides, which are complementary to adjacent regions of a target (**Figure 2.10b**). In the absence of target, the two oligonucleotide probes are distributed randomly and separated in solution, leading to the fluorescence emission from the donor. Adding the target brings the two oligonucleotide strands together and forces donor and acceptor into close proximity. Upon exciting the donor, energy is transferred from the donor to the acceptor, which results in significant emission from the acceptor.

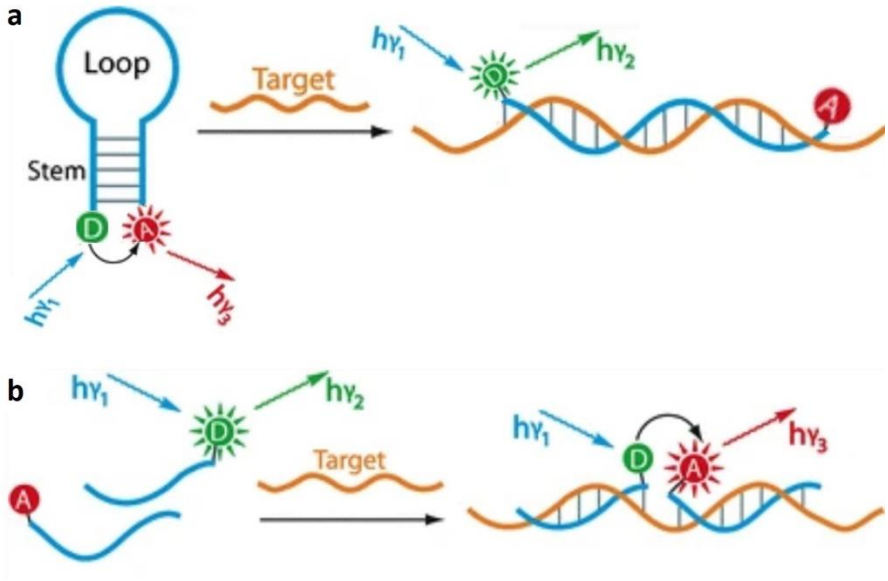

Figure 2.10 Common designs for FRET hybridization probes. **a.** Standard MB; **b.** Standard BP. (Adapted with permission from reference [146]. Copyright 2011 Springer Nature.)

2.4 Lanthanides

Lanthanides comprise 15 metallic chemical elements with atomic numbers from 57 to 71 (La, Ce, Pr, Nd, Pm, Sm, Eu, Gd, Tb, Dy, Ho, Er, Tm, Yb, and Lu), that are known as the rare earth elements. It is difficult in obtaining a pure form of lanthanides due to the similarity in chemical properties, which can be explained by the electronic configuration of the atoms and their derived ions. The general electronic structure of the lanthanide elements is $[Xe]4f^{0-14}5d^{0-1}6s^2$, where the 4f orbitals are gradually filled from La (0) to Lu (14) making them differ in the ability to absorb and emit light [147]. Usually, lanthanides are dominated by the trivalent oxidation state (Ln^{3+}) and Ln^{3+} ions in aqueous solutions are the most stable state with electronic configuration as $[Xe]4f^n$ [148]. Particularly, Ce^{3+} can lose its single f electron to form Ce^{4+} with the stable electronic configuration with an empty f orbital, and Eu^{3+} can gain an electron to form Eu^{2+} with the $4f^7$ configuration that has the extra stability of a half-filled orbital. The 4f orbital is the factor that distinguishes lanthanides from other transition elements and has profound effect on lanthanides.

Most Ln^{3+} ions are luminescent, which arises from the transitions involved in redistribution of electrons within 4f orbitals (f-f electronic transitions) and related to a rich variety of energy levels (**Figure 2.11a**) [149]. The energies of these levels are well defined due to the sterically shielding of 4f orbitals from surrounding environment by the filled $5s^2$ and $5p^6$ sub-shells, resulting in almost no perturbations in these electronic transitions, and consequently appearing as several sharp and narrow emission bands specific for lanthanides [149, 150]. Among them, Tb^{3+} and Eu^{3+} have relative sizeable energy gap ($^5D_4$ - ^7F_J for Tb^{3+}, $^5D_0$ - ^7F_J for Eu^{3+}), and various emission wavelengths to emit green and red lights across a broad spectral range (> 100 nm) (**Figure 2.11b)**, thus have been most widely used, especially for the development of valuable luminescent probes [151, 152]. To summarize, lanthanides possess easily recognizable and fascinating optical properties, allowing their application in various areas, such as construction of efficient light conversion devices [153, 154], biomedical analysis and imaging [155], production of hybrid and multifunctional materials [147, 156], and many others.

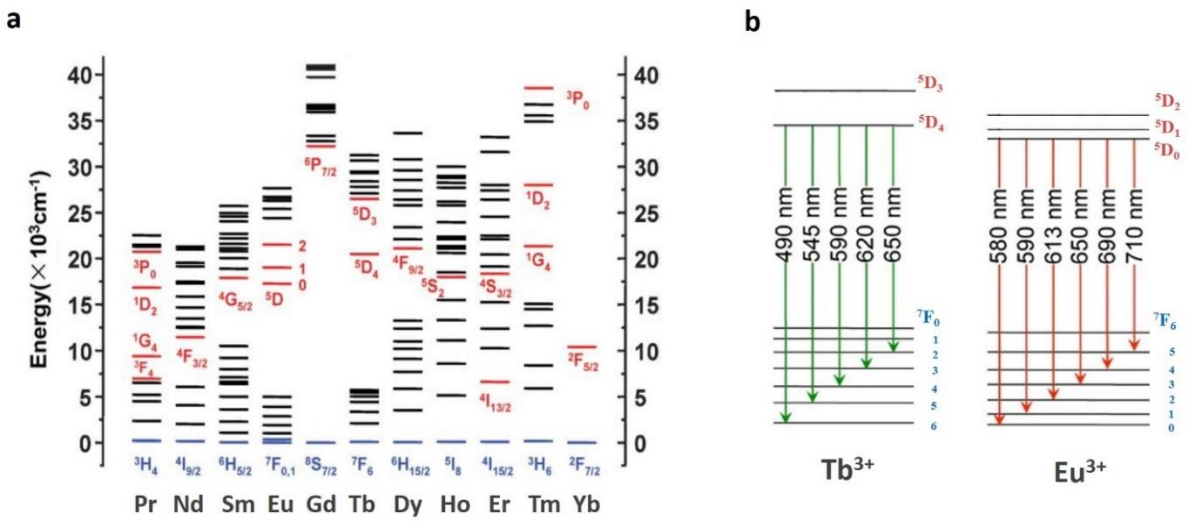

Figure 2.11 a. Partial energy level diagram for some Ln^{3+} ions. The main luminescent levels are drawn in red, while the fundamental level is indicated in blue. (Adapted with permission from reference [149]. Copyright 2005 American Chemical Society.); **b.** Commonly observed emission wavelengths as a result of electronic transitions for Tb^{3+} ($^5D_4$ - ^7F_J transitions) and Eu^{3+} ($^5D_0$ - ^7F_J transitions). (Adapted with permission from reference [151]. Copyright 2014 American Chemical Society.)

2.4.1 Luminescent lanthanide complexes

As mentioned, the unusual luminescence properties of lanthanides originate from f-f transitions. While according to the Laporte selection rule and sometimes due to the change in spin multiplicity, such transitions have quite low probabilities [148]. Consequently, Ln^{3+} ions themselves display quite long lifetimes (*ca.* 400 μs for Tb^{3+} and *ca.* 120 μs for Eu^{3+} in aqueous) and very low molar absorption coefficients ($\varepsilon < 1\ M^{-1}cm^{-1}$), which can be more than 10^4 - 10^5 times lower than that of traditionally used organic fluorophores [157]. Unless utilizing a high-power laser, the direct excitation of Ln^{3+} ions are very inefficient. However, the problem of weak light absorption is overcome after the development of a so-called "antenna effect" [158]. As shown in **Figure 2.12a**, some organic chromophores with strong absorption can be coordinated with Ln^{3+} ions to form luminescent lanthanide complexes (LLCs) as chelates or cryptates, that can be a light absorbing "antenna" to transfer absorbed energy to lanthanide ion, and also serve as a "cage" to protect central lanthanide ion from environmental luminescence quenching. As another consequence of the aforementioned

shielding, the 4f orbitals are minimally involved in chemical bonding. Thus, the antenna ligands in the first and second coordination sphere perturb the electronic configurations of the trivalent lanthanide ions only to a very limited extent [147], and the bonding is mainly electrostatic and nondirectional, which imparts great flexibility on LLCs in terms of coordination number and geometry [148]. In general, the LLCs in aqueous solutions exhibit coordination numbers from 8 to 10, that are able to saturate the central Ln^{3+} coordination sphere to prevent luminescent quenching by surrounding water molecules.

The commonly accepted antenna effect mechanism is proposed by Crosby and Whan [160] and can be modelled using Jablonsky's diagram (**Figure 2.12b**). Briefly, upon excitation, ligand absorbs energy to its singlet excited state (S_0 to S_1), and then undergoes intersystem crossing to its triplet excited state (S_1 to T_1), which has long lifetime due to the spin restriction of the back transition into the ground states. Then intramolecular energy transfer occurs from the ligand to the Ln^{3+} ion and populates the Ln^{3+} ion excited state (T_1 to $(Ln^{3+})^*$), finally generating characteristic Ln^{3+} luminescence from the lowest excited state to its ground state (^5D_J to ^7F_J). Given the short lifetimes of the S_1 states for organic chromophores, energy transfer is usually assumed as proceeding from the long-lived T_1 states, although singlet states and charge transfer can also play a role [161, 162].

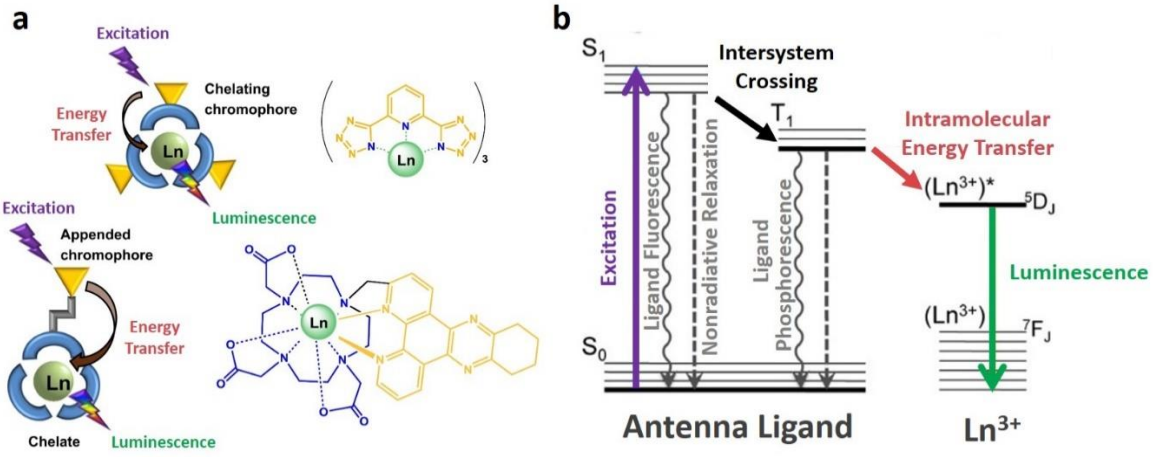

Figure 2.12 a. The scheme of LLCs using the chelating chromophoric (top) and appended chromophoric (bottom) ligand designs and corresponding examples (right). (Adapted with permission from reference [159]. 2015 Elsevier B.V.); **b.** Simplified Jablonski diagram for the antenna effect of LLCs. (Adapted with permission from reference [151]. Copyright 2014 American Chemical Society.)

Benefiting from specific "antenna effect", LLCs provide a considerable variety of advantages compared to other fluorophores [163]:

(i) The overall quantum yield of a LLC (Φ_{LLC}^{ligand}), given by **Equation 2.10**, can be increased by improving η_{ET} and Φ_{LLC}^{Ln}:

$$\Phi_{LLC}^{ligand} = \frac{photons\ emitted\ by\ Ln}{photons\ absorbed\ by\ ligand} = \eta_{ET} \times \Phi_{LLC}^{Ln} \quad (2.10)$$

where Φ_{LLC}^{ligand} is the overall quantum yield of LLC from indirect excitation of the Ln^{3+} ion through the antenna ligand, Φ_{LLC}^{Ln} is the intrinsic quantum yield from direct excitation of the Ln^{3+} ion, η_{ET} is the intramolecular energy transfer efficiency from ligand to Ln^{3+} ion. Improved η_{ET} can be achieved by selecting the antenna ligand with a high intramolecular energy transfer rate. Improved Φ_{LLC}^{Ln} can be achieved by the Ln^{3+} ion carrier chelate, which protects the centered Ln^{3+} ion from the aqueous matrix quenching, and thus minimizes the nonradiative process.

(ii) Possibility to increase the molar absorption coefficients and vary absorption spectra by choosing appropriate antenna ligands. In addition, the ligand absorption occurs at a shorter wavelength compared to the intrinsic lanthanide absorption. Thus, the indirect excitation of Ln^{3+} ions through their antenna ligands results in red shift of the lanthanide emission spectra by more than hundred nanometers from the ligand absorption spectra, namely the large effective "Stokes shift" (**Figure 2.13a**). The well-separated excitation and emission wavelengths of the LLCs allow facile blocking of stray excitation light by cut-off filters and/or dichroic mirrors.

(iii) LLCs possess long excited-state lifetimes, which are increased up to ms by coordinating Ln^{3+} ions with chelate/cryptate ligands. It allows the possibility to use delayed or time-gated acquisition of the emitted light measured by time-resolved spectroscopy (mentioned in **Section 2.3.2**). Upon pulsed excitation of a sample, by measuring the long-lived luminescence intensity decay in a time-window that opens after luminescence of other components have already decayed, the relatively short-lived background can be efficiently

suppressed including the auto-fluorescence of sample or other fluorophores, as well as the light scattering from excitation source. The scheme of time-resolved spectroscopy with combination of temporal (time-window) and spectral (filter) resolution is illustrated in **Figure 2.13c** using Eu complex as example.

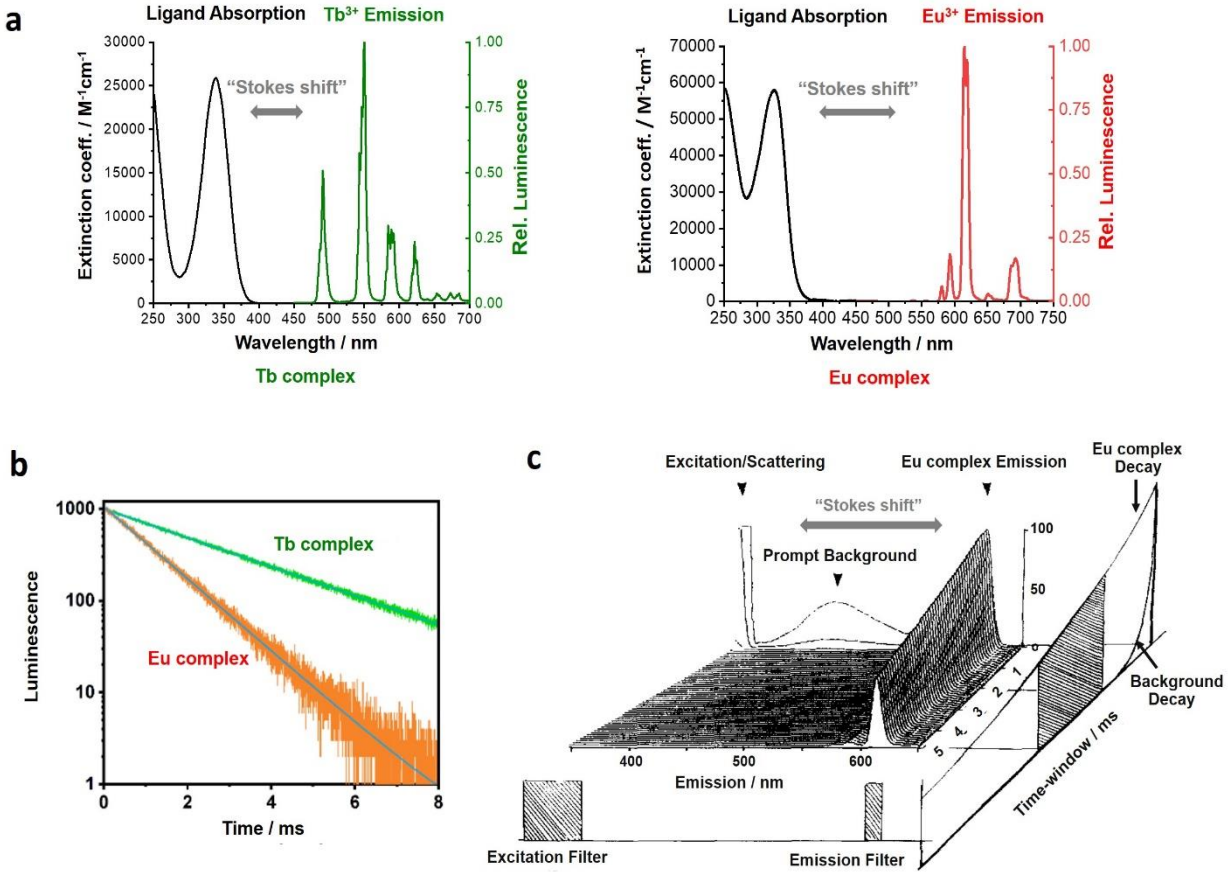

Figure 2.13 a. Absorption and emission spectra, and **b.** Luminescence decay of Tb complex and Eu complex. (Adapted with permission from reference [164]. Copyright 2018 Wiley-VCH Verlag GmbH & Co. KGaA.); **c.** The scheme of time-resolved spectroscopy with combination of temporal (time-window) and spectral (filter) resolution using Eu complex as example. (Adapted with permission from reference [165]. Copyright 1995 Elsevier B.V.)

In summary, LLCs exhibit bright luminescence, large "Stokes shift" (not an actual Stokes shift because ligand get excited and lanthanide ion emits), and long-lived luminescence lifetimes, which makes them versatile luminescent probes for a wide variety of

bioanalytical assays [150, 152], especially ideal energy donors in time-resolved FRET-based applications [166].

2.4.2 Luminescent Tb complexes as FRET donors

LLCs are frequently utilized as FRET donors paired with different fluorophores as acceptors, which provides the capability for obtaining nanometric distance information and offers "on/off" signaling for quantitative analysis in biological processes [167, 168]. In preference to other lanthanide ions, luminescent Tb complexes (LTCs) have been the major players in this field, particularly possessing an outstanding advantage of multiplexing capability, which will be discussed hereinafter. The macrocylic ligand-based Lumi4-Tb complex (**Figure 2.14**) is used in this thesis, which contains 2-hydroxyisophthalamide ligands with a molar absorption coefficient of *ca.* 26,000 $M^{-1}cm^{-1}$ at 340 nm in aqueous solution. It can be conjugated to the biomolecules through –NHS (N-hydroxysuccinimide) functional groups.

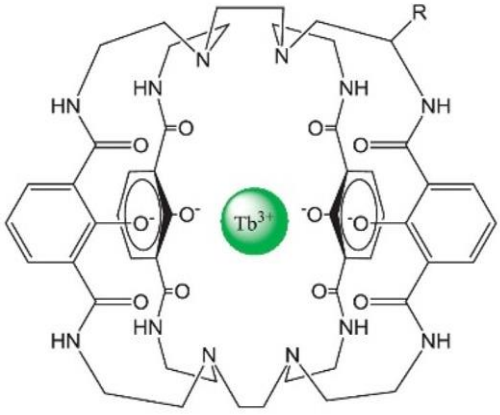

Figure 2.14 Chemical structure of Lumi4-Tb complex, R represents the place for the functional group. (Adapted with permission from reference [169]. Copyright 2014 Elsevier B.V.)

There are remarkable advantages distinguishing LTCs from other FRET donors [169]:

(i) Long decay time. Long-lived excited state is one of highlighted properties of LTCs discussed in the last section. While, as mentioned in **Section 2.3.2**, the significant difference in the excited-state lifetimes of donor and acceptor results in approximately equal luminescence decay times for FRET-quenched donor and FRET-sensitized acceptor.

Therefore, the decay time of donor in the presence of acceptor (τ_{DA}) can be replaced by the decay time of acceptor in the presence of donor (τ_{AD}) in **Equation 2.8**, and both quenched donor emission and sensitized acceptor emission can be used for time-resolved FRET analysis. Moreover, detection of FRET-sensitized acceptor luminescence combined with time-windows can get rid of background signal including auto-fluorescence, direct acceptor luminescence, or pure donor luminescence (assuming no spectral crosstalk). As a consequence, concentration effects and incomplete bioconjugation arising from excessive concentrations of donor or acceptor, unlabeled biomolecules, and free donor or acceptor can be largely avoided.

(ii) Unpolarized emission. Due to the multiple transition dipole moments (unpolarized emission), LTCs are able to act as randomized donors. Thus, the orientation factor κ^2 value can be limited between $1/3$ and $4/3$ as discussed in **Section 2.3.1**. In most cases, FRET acceptor is generally labeled to a biomolecule that has fast isotropic rotation. Therefore, the system is in a dynamic averaging regime and κ^2 becomes $2/3$. Even with an acceptor having a fixed transition dipole moment, $2/3$ is still an appropriate approximation.

(iii) Multiplexing capability. The increasing demand for multiplexing, which enables the simultaneous measurement of multiple distinctive species in a single sample, has promoted the interests in lanthanide-based FRET biosensing approaches.

LTCs possess well-separated and narrow emission bands and are therefore superior for spectral multiplexing. These emission bands are in a spectral range where many fluorophores are excellent absorbers and therefore relatively large spectral overlap integrals can be achieved. As shown in **Figure 2.15a**, both organic dyes and QDs have large spectral overlap with LTCs and can act as FRET acceptors. By emitting light between or beyond LTCs emission bands, simultaneous luminescence detection can be realized with the same LTC donors paired with multiple acceptors. The utilization of optical transmission filters enables the efficient spectral separation, especially for the QDs as they have narrower symmetric emission profiles in contrast to dyes. Due to the broad emission profiles of most organic dyes, several different dyes may emit in the same wavelength region of the optical transmission filter, which is the so-called spectral crosstalk. Additional correction needs to

be performed to achieve efficient multiplexing and an example of such crosstalk correction can be found in previous work of our group [170].

In addition to spectral multiplexing, temporal multiplexing can also be achievable if different luminescence decay times are distinguishable. In terms of LTCs donor, different decay times $\tau_{AD} = \tau_{DA}$ due to the different efficiencies results from different donor-to-acceptor distances for the same FRET pair. Taking the extremely long luminescence lifetime of LTCs and the tunable distances between the same LTCs and different acceptors, it is allowed for flexible designing of different FRET-quenched and FRET-sensitized decay times. Besides, by introducing distinguishable spectra and intensities as another multiplexing dimensions, combined temporal and spectral multiplexing (spectrotemporal multiplexing) can be feasible and recently has been applied for simultaneous detection of four different DNAs in single homogenous sample by our group (in **Figure 2.15b**) [171].

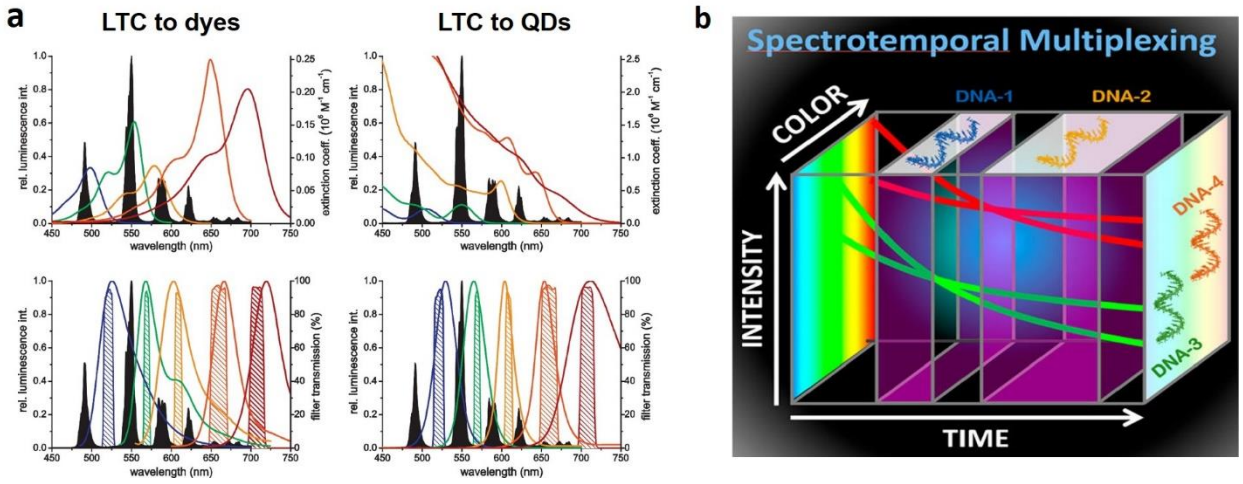

Figure 2.15 a. LTC-donor-based spectral multiplexed FRET using different organic dyes (left) and QDs (right). Top: Broad spectral overlap between LTCs emission and the absorption of several different acceptors. Bottom: Separation of the single LTCs emission bands allows the measurement of different acceptors in wavelength ranges with very low LTCs intensity (represented by the shaded bandpass filter transmission spectra). LTCs-emission-spectra in black. Left: OregonGreen (blue), AlexaFluor555 (green), AlexaFluor568 (orange), Cy5 (red) and AlexaFluor700 (brown); right: QD525 (blue), QD565 (green), QD605 (orange), QD655 (red), and QD705 (brown). (Adapted with permission from reference [169]. Copyright 2014 Elsevier B.V.); **b.** Scheme of the spectrotemporal multiplexing using time-resolved FRET with one LTCs as donor, two different Cyanine dyes as acceptors, and two different time-windows for the simultaneous detection of four different DNAs in single homogenous sample. (Adapted with permission from reference [171]. Copyright 2018 American Chemical Society.)

2.5 Fluorescent dyes

2.5.1 Introduction

Organic dyes are still playing the dominant role in the fluorescent labeling field, and also act as the first type of dyes tested with novel or "nontraditional" materials. The common fluorescent dyes are shown in **Figure 2.16a**. Their emissions can span ultraviolet to near-infrared spectrum that are usually related to their structures. The ultraviolet dyes are typically pyrene-, naphthalene-, and coumarin-based structures, while the visible or near-infrared dyes include various fluorescein-, rhodamine-, and cyanine-based derivatives (**Figure 2.16b**). Some redder dyes have low solubility in aqueous solvents limiting their application, while fluorescein-based dyes have high solubility, but suffer from high rate of photobleaching and self-quenching [168]. Cyanine dyes may alleviate some of these issues [168]. As well-known biomolecular labels, they have been widely used for microarrays, FRET experiments, imaging, and many other analyses in the recent decades [172-175]. Typically, cyanine dye family denotes a dye system with a polymethine chain between two nitrogens (**Figure 2.16b**). These compounds are given common names according to the number of carbon atoms between the dihydroindole units (*e.g.* Cy3 and Cy5) [176]. A further elaboration of the structure enables to provide control over wavelength, and such structural modification is designated with a ".5" suffix (*e.g.* Cy3.5 and Cy5.5) [176]. In this thesis (in **Section 3** and **Section 4**), Cy5.5 is used with a molar absorption coefficient of *ca.* 209,000 $M^{-1}cm^{-1}$ at 684 nm in aqueous solution. It can be conjugated to the biomolecules through –NHS functional group.

In general, fluorescent dyes have several advantages including commercial availability, cost-effectiveness, high quantum yields, and easy bioconjugation (*via* –NHS ester, maleimide, hydrazide, or amine functional groups), and have been extensively used in FRET applications [177]. Most importantly, there are widespread description of their FRET properties in the literatures, demonstrating their accessibility to suitable design and flexible utilization as FRET pair (donor and/or acceptor).

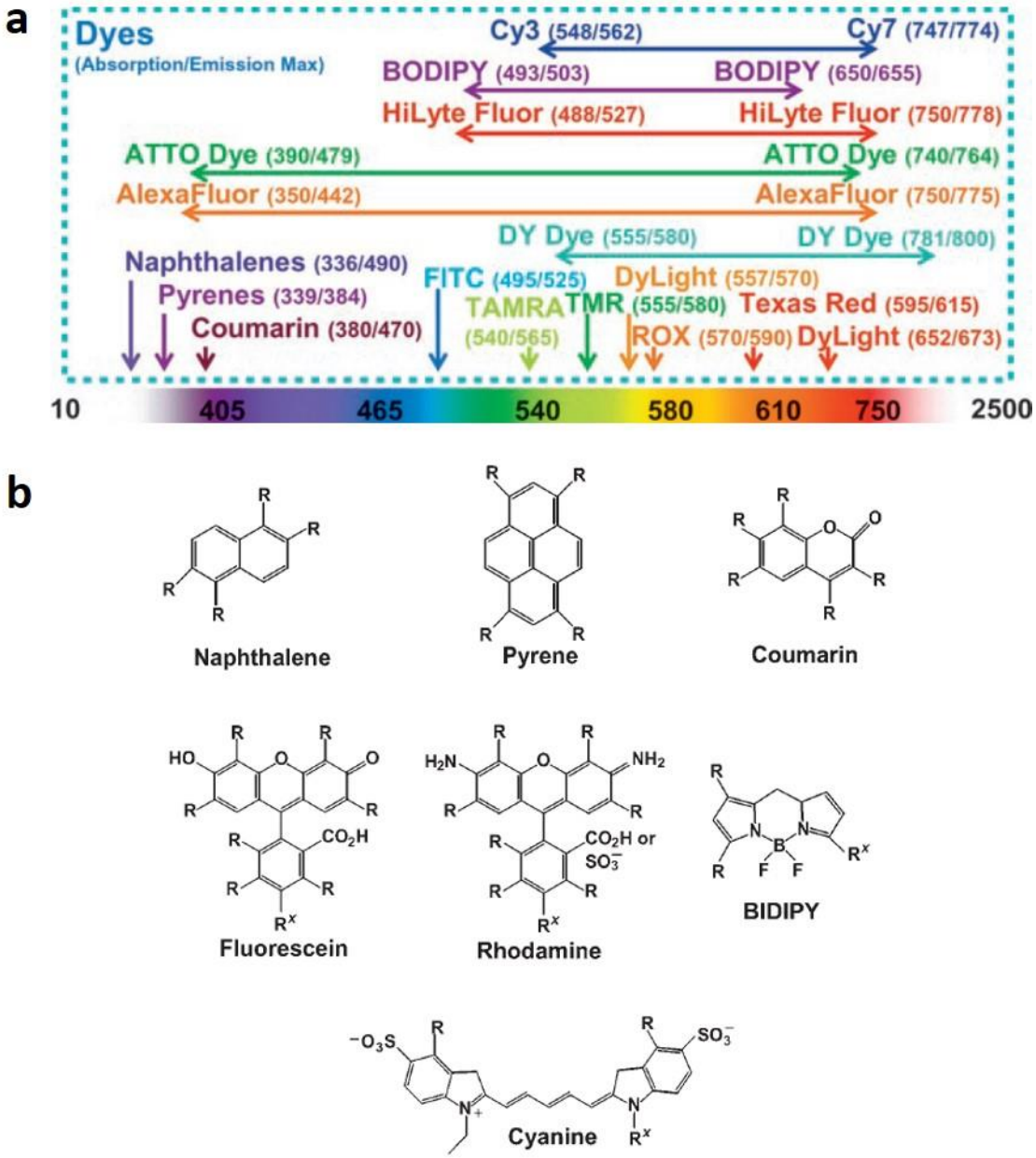

Figure 2.16 a. Common fluorescent dyes. Absorbance and emission maxima along with spectral regions covered by a particular dye family are highlighted. FITC is fluorescein-based dyes; TAMRA, TMR, and ROX are rhodamine-based dyes; Cy3 to Cy7 are cyanine-based dyes; **b.** Chemical structures of common ultraviolet/visible/near-infrared fluorescent dyes. R marks the typical position of substituents position; R^x marks the typical position of the bioconjugation linker. (Adapted with permission from reference [168]. Copyright 2006 WILEY-VCH Verlag GmbH & Co. KGaA, Weinheim.)

2.5.2 Fluorescent dyes in FRET applications

Fluorescent dyes are considered as "traditional" FRET dyes that represent the majority donors or/and acceptors used in FRET applications. There are various resources available to aid in choosing suitable dyes in FRET pairs, such as "The Molecular Probes Handbook" written by Johnson and Spence [178], some web-based Fluorescent Spectraviewer programs (Thermo Fisher, Bio-Rad, ZEISS, and *etc.*), and many other reviews [179-181]. Traditional dye-to-dye FRET system still occupy many current applications. It has tremendous impact on biomedical research, specifically in the areas of nucleic acid analysis. In nucleic acid biosensing, the probes are labeled with appropriate dyes to generate the target-specific FRET signal through undergoing a target-induced conformation change (*e.g.* MB) or a target-involved hybrid formation (*e.g.* BPs) (**Section 2.3.3 Figure 2.10**). Particularly, in amplification-based detection technologies, for instance in PCR, the FRET probes are cleaved during the reaction (*e.g.* TaqMan probes), or incorporated into amplified DNA (*e.g.* Scorpion primers), not only realizing FRET but also monitoring the amplification [182]. Nowadays, the TaqMan probes have been commercially used as RT-qPCR reaction kit for miRNA detection. Apart from dye-to-dye combinations, fluorescent dyes coupling with various other materials (e.g. quantum dots, upconversion nanoparticles, graphene oxide) as FRET pairs have also been widely used in FRET-based nucleic acid analysis [183-185].

Despite the wide utilization, there are inherent drawbacks of fluorescent dyes-based FRET applications. Their broad absorption/emission profiles and small Stokes shifts often lead to direct excitation of the acceptor, which complicates subsequent analysis. Especially for the spectral multiplexing, when using different dyes, the spectral crosstalk due to their broad emission spectra increases the complexity and requires an additional optical correction. Lifetime multiplexing can sufficiently overcome these limitations as described in the previous section. In this thesis, the lifetime multiplexing for simultaneous detection of miRNAs is realized based on LTCs-to-Cy5.5 FRET and details are shown in **Section 4**.

2.6 Quantum dots

Quantum dots (QDs) are semiconductor nanocrystals that are typically composed of group II-VI (*e.g.* CdS, CdSe, CdTe, ZnS, and *etc.*) or III-V (*e.g.* GaAs, GaN, InAs, and *etc.*) elements, or their alloys (*e.g.* CdSeS, InGaN, InGaAs, and *etc.*) with small sizes range from 1 to 10 nm [186]. They provide unique and excellent photophysical properties that are superior to traditional organic fluorophores. Besides, good biocompatible QDs can be functionalized and bioconjugated with small biomolecules including nucleic acids, peptides, and proteins, which enables recognition of biomarkers, targeting cells/tissues, and delivery of drugs. As a consequence of these properties, QDs are frequently used in a large variety of bioanalytical investigations.

2.6.1 Photophysical properties

QDs are crystalline materials with facets and a lattice structure analogous to the bulk semiconductor materials, and possess electronic properties that are in intermediate regime between bulk semiconductors and molecules [187, 188]. The electronic structure of bulk semiconductor is characterized by a lower energy valence band (VB) that is occupied by electrons, and a higher energy conduction band (CB) that is empty. Upon excitation, an electron is promoted from the VB to CB leaving a positive hole in VB. The interaction between the electron and the hole creates an exciton, and the distance between electron-hole pair is referred to as the exciton Bohr radius. Typically, the VB and CB are separated by a band gap depending on the semiconductor materials, and can be regarded as continuous energy levels due to the large density of electronic states. While when the size of semiconductor material becomes smaller and close to the exciton Bohr radius, the density of electronics states is not sufficient to form complete band structures, and thus discrete energy levels exist at the band edges. The energy levels become more separated as the size become smaller, and consequently the energy band gap becomes larger (**Figure 2.17a**). This phenomenon is known as quantum confinement, and most unique properties of QDs originated from the quantum confinement effect. The difference in energy between the VB

and CB is conserved in the form of emitted photons, and therefore this band gap dictates the energy (wavelength) of the light emitted from the QDs. As the QD energy band gap is directly related to its diameter, QDs comprising the same semiconductor material can be tuned to emit different wavelengths by simply changing their size (**Figure 2.17b**).

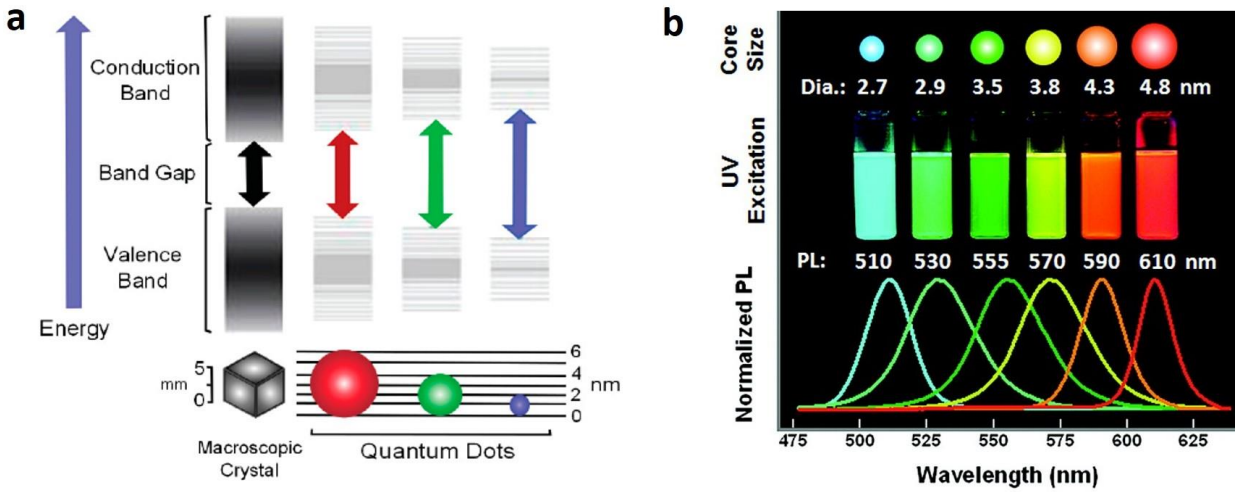

Figure 2.17 a. Discrete energy levels and band gap in semiconductor crystals with increasing nanocrystal size. (Adapted with permission from reference [189]. Copyright 2015 MDPI.); **b.** Progressive color and PL wavelength changes of CdSe/ZnS QDs with increasing nanocrystal size. (Adapted with permission from reference [190]. Copyright 2011 American Chemical Society.)

In summary, QDs have extraordinary photophysical properties that make them excellent fluorophores in biosensing applications [191, 192]:

(i) Narrow, symmetric, and size-dependent photoluminescence (PL) spectra continuously across a broad range from the ultraviolet to near-infrared, making them ideal for spectral multiplexing strategies.

(ii) Broad and continuous absorption profiles allow free selection of excitation wavelength.

(iii) High brightness due to high quantum yields and large absorption cross-sections.

(iv) High photostability making them resistant to photobleaching and chemical degradation.

(v) Large Stokes shifts compared to organic dyes that efficiently separates excitation and emission lights.

(vi) Relatively large nanoparticle surface for a variety of functionalization schemes.

2.6.2 QDs in FRET applications

QDs display unique optical features and their nanoparticle properties make them superior FRET partners that can serve as both donor and acceptor. As the FRET efficiency is highly dependent on the donor and acceptor distance, QDs are frequently functionalized and bioconjugated with small ligands or small-sized biomolecules to create stable QDs, as well as the formation of the resulting QD bioconjugates. The FRET-sensitized QD emission signal upon target recognition through biological binding event and/or conformational change can be easily measured, and thus enables sensitive and specific detection of various biomolecules of interest, such as nucleic acids, proteins, enzymes, or other biomolecules.

QDs are most frequently used as FRET donors that benefits from several advantages. The extremely high extinction coefficients as well as broad absorption wavelength range enable the efficient and selective excitation of QD donors. The size-tunable PL spectra enable to adjust appropriate spectral overlap with various acceptors. The narrow and symmetric emission spectra reduce the opportunity of donor emission leakage into the acceptor detection channel, which favors multiplexing applications. Besides, the large surface area of QDs provide more possibility to attach many acceptors onto the surface.

For nucleic acids detection, in addition to FRET donors, QDs also act as interfaces for the immobilization of oligonucleotide probes. A hybridization event is usually used to bring the acceptor in close proximity to the donor QD *via* several strategies, such as MBs, BPs, intercalating dye, and displacement hybridization format (**Figure 2.18**). The basic principle of MBs and BPs was described before. Ma *et al.* developed a novel two-dimensional dual-modal MB for mRNA-activated cancer theranostics by constructing MB with a QD as donor, a photosensitizer (chlorin e6) and a dark quencher (BHQ3) as acceptors (**Figure 2.18a**) [193]. This method overcomes the disadvantages of traditional MB, and provides high imaging sensitivity and therapeutic efficacy. Based on BPs strategy, Zhang *et al*. integrated an isothermal amplification method (HRCA) into QD-based FRET sensors and realized simultaneous detection for two miRNAs with high sensitivity (**Figure 2.18b**) [194]. In the strategy based on intercalating dye, target oligonucleotide is directly hybridized with

QD-oligonucleotide conjugates, generating FRET signal between QD and intercalating dye. Krull *et al.* constructed a paper-based platform using QD-DNA probes and intercalating dye for the detection of gene sequence that are associated with spinal muscular atrophy (**Figure 2.18c**) [195]. In strand displacement strategy, an initial FRET-on format generated by hybridizing QD-oligonucleotide conjugates with dye-labeled oligonucleotides is ultimately switched to FRET-off format in the presence of the target nucleic acid which displaced the dye labeled DNA probe (**Figure 2.18d**) [196]. A target recycling miRNA detection assay combined with isothermal amplification method (DSNSA) is performed based on this strategy with the help of a duplex-specific nuclease [197]. The proposed method is highly sensitive with the limit of detection as 42 fM (1.2 amol) for miR-148, and shows excellent selectivity versus mismatched sequences and other miRNAs.

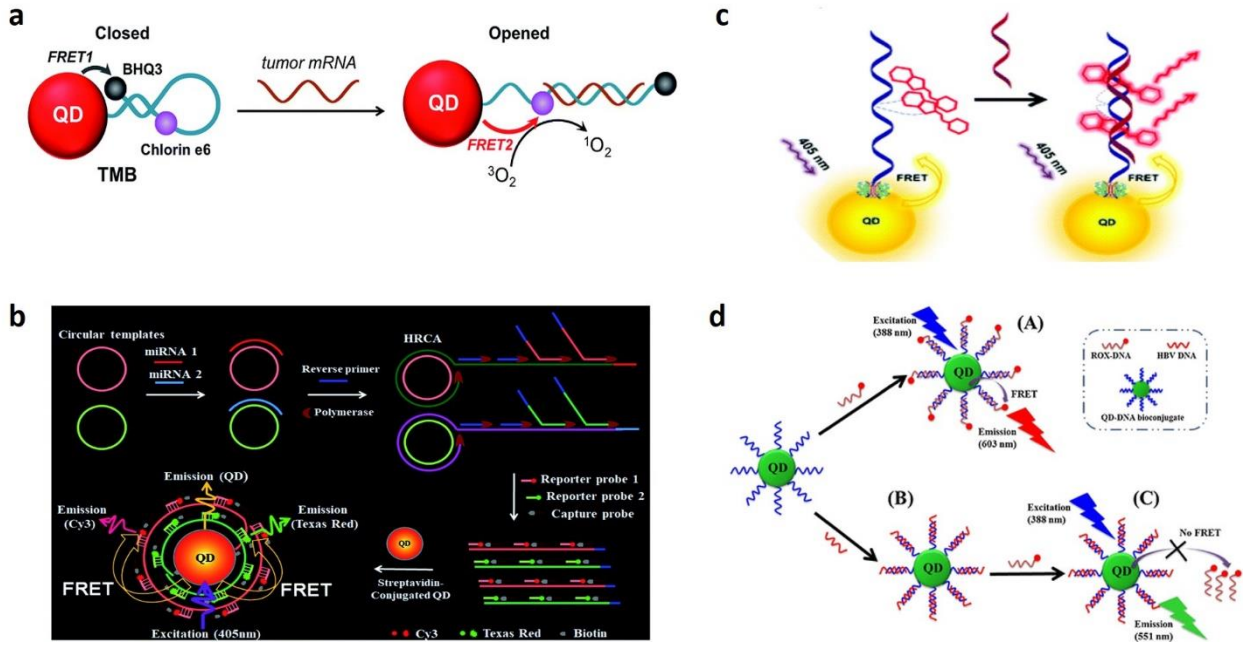

Figure 2.18 FRET-based biosensors using QDs as donors for nucleic acids detection. **a.** Schematic illustration of a tumor mRNA detection based on MB strategy. (Adapted with permission from reference [193]. Copyright 2015 The Royal Society of Chemistry.); **b.** Schematic illustration of simultaneous detection for two miRNAs based on BPs strategy. (Adapted with permission from reference [194]. Copyright 2018 The Royal Society of Chemistry.); **c.** Schematic illustration of a gene sequence (associated with spinal muscular atrophy) detection based on intercalating dye strategy. (Adapted with permission from reference [195]. Copyright 2019 The Royal Society of Chemistry.); **d.** Schematic illustration of HBV DNA detection based on strand displacement strategy. (Adapted with permission from reference [196]. Copyright 2013 The Springer Nature.)

Although QDs are most commonly used as FRET donors, QD acceptor-based FRET has also been well established. The large absorption cross-sections of QDs result in very large spectral overlap integrals and hence large Förster distances. The relatively large surfaces of QDs provide multiple attaching sites of donors on the surfaces, leading to an increased probability of FRET sensitization with the number of donors, while the FRET efficiency is not affected. What's more, their narrow and symmetric emission spectra favor multiplexed detection without spectral crosstalk. However, two general drawbacks need to be taken into account. First, the broad absorption spectra and high extinction coefficients of QDs hamper the selective excitation of the respective FRET donors, because the QD acceptors are efficiently excited at almost any wavelength independently of the donor. The second problem arises from the difference in the excited-state lifetimes between donors and QD acceptors. For instance, the lifetimes of dyes are usually a few ns with a monoexponential decay process, whereas the lifetimes of QDs are usually tens to hundreds of ns with a multiexponential decay. If both dye and QD are excited at the same time, there is a very high probability that the dye will decay back to its ground state before the QD, and therefore the possibility of FRET will be extremely low.

As sufficiently described before, the introduction of time-resolved spectroscopy using LLCs as FRET donors, whose PL lifetimes are up to several ms, is one of the keys to solve the problem of simultaneous donor and acceptor excitation. Time-resolved spectroscopy is used to record the luminescence intensities of FRET pairs in individual detection channels in a time-gated window (several μs after pulsed excitation). By collecting PL intensities in time windows much longer than the natural decay of the QD, but still within the lifetime of the LLCs decay, the direct excitation of the QD and any background autofluorescence will not be recorded, thus greatly simplifying analysis of the system. Since 2005, our group has shown that QDs can be used as efficient FRET acceptors when paired with Eu or Tb complexes (LTCs) as donors in time-resolved FRET systems, and several biological assays have been demonstrated using ratiometric output (the ratio of the time-gated PL intensities of the FRET-sensitized acceptor and FRET-quenched donor) to quantify the analytes of interest [198]. In our recent studies, multiplexed detection of several clinically relevant

biomarkers has been achieved specifically and sensitively using time-gated LTCs-to-QD FRET strategy (**Figure 2.19**).

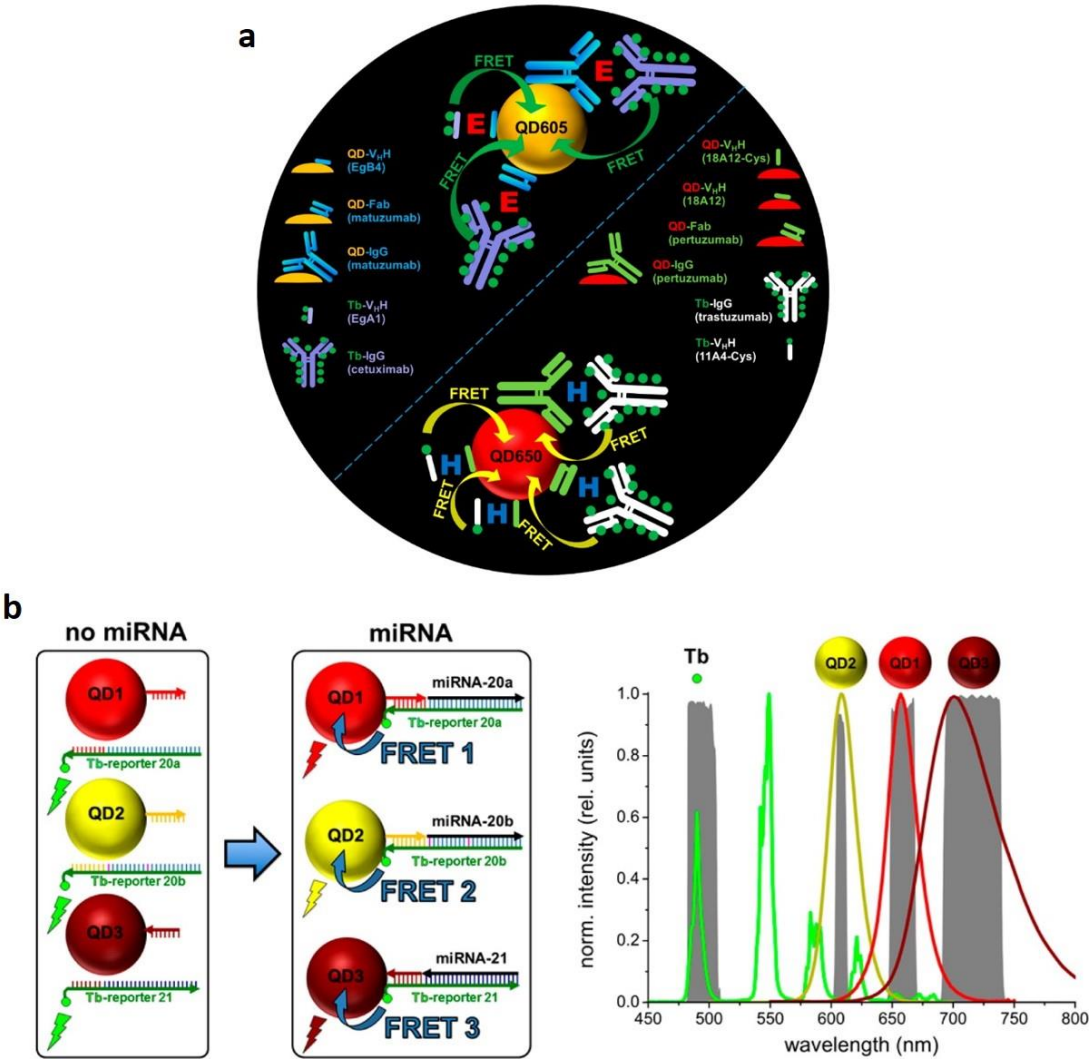

Figure 2.19 FRET-based biosensor using QDs as acceptors and LTCs as donors for clinically relevant biomarkers detection. **a.** Schematic illustration of the duplexed detection for epidermal growth factor receptors EGFR and HER2 with the combination of different types of antibodies against EGFR and HER2. (Adapted with permission from reference [199]. Copyright 2016 American Chemical Society.); **b.** Left: Schematic illustration of the three FRET systems for multiplexed miRNAs detection; Right: The three FRET systems can be distinguished by the PL emission spectra of the QD acceptors, which are detected (together with the Tb PL spectrum) at different detection channels (gray spectra in the background). (Adapted with permission from reference [200]. Copyright 2015 American Chemical Society.)

QDs could engage in FRET with each other as a QD-to-QD FRET system [189]. A primary advantage of QDs in QD-to-QD FRET sensing is their high photostability compared to organic dyes or fluorescent proteins, making QDs uniquely suitable for longitudinal studies, where measurements or images are taken repeatedly over extended periods of time. They are good candidates for device-on-a-chip applications and for sensors designed to be utilized outside of the laboratory setting. In addition, the extraordinary brightness of QDs yields considerable fluorescence output with relatively fewer emitters and potentially decreases the limit of detection in sensing applications. However, QD-to-QD FRET is challenging due to the broad, overlapping excitation spectra from the two nanocrystals, precluding the selective excitation of the donor. This induces crosstalk and creates a large background signal, which is a major challenge in QD-to-QD FRET sensor design.

3. Advanced miRNA diagnostics using RCA-amplified Tb-to-dye FRET

3.1 Introduction

MiRNA-based diagnostics has the potential to play a pivotal role for the prognosis, diagnosis, management, and monitoring of diseases because varying expression levels can be detected in most solid (cells, tissues) and liquid (blood, urine, saliva) clinical samples [201-203]. Among the standard miRNA detection methods, such as RT-qPCR, NGS, or microarrays, RT-qPCR is arguably the most suited technology for routine and simple use. However, the necessity of reverse transcription and multiple primers, the sensitivity to contamination generated by RNA extraction, and the rather extensive guidelines for obtaining reliable results with qPCR present serious drawbacks for simple and reliable analysis [204]. In addition, the large majority of clinical studies that have related different miRNAs in solid (tissues) and liquid (blood) biopsies to various cancers, diabetes, sepsis, infectious and cardiac diseases, have used relative concentrations because the absolute quantitation is impossible with NGS and too imprecise with RT-qPCR [205, 206]. Selective, sensitive, and precise absolute quantitation is one of the most important aspects for translating the use of miRNA biomarkers to the clinic.

Many emerging technologies have been developed over the recent years that can overcome the technical limitations of the standard technologies, and the most frequently applied strategies are fluorescent-based detection and isothermal amplification with optical readout [200, 207-210]. Isothermal amplification method provides detection of a nucleic acid target sequence in a streamlined or exponential manner, and is not limited by the constraint of thermal cycling, which has been a robust, reproducible, and simple amplification strategy. As one common used isothermal amplification, target-primed RCA generates long ssDNA with a tandem sequence, where target can be amplified 10,000-fold in a few hours. An increasing number of RCA combined with different luminescence readout strategies has

been developed for specific and sensitive detection of miRNAs [99, 105, 120, 211-213]. However, few proposed technologies have been translated into routine clinical practice due to the missing proofs for relevant clinical application. Highly important requirements for a new technology to become a useful miRNA detection method, and to advance miRNA-based diagnostics and translational research are not only sensitivity and specificity but also the capability to be applicable to different types of clinical samples and to obtain useful clinical information from those samples.

To advance this translational research endeavor, this work integrated the ratiometric and single-step detection format of time-gated FRET (TG-FRET) from a Tb donor to a Cy5.5 acceptor in target-primed RCA (**Figure 3.1**). In contrast to many other emerging technologies, the proposed method can not only detect very low amounts of miRNAs, but also provides extremely high specificity against precursor miRNA (pre-miRNA) and miRNAs with single nucleotide variations. We also demonstrated the immediate practical applicability by precise quantification of endogenous miRNAs from various types of clinical samples and for different pathologies, namely miR-21 from human plasma and tissue related to ovarian and breast cancer [214, 215], miR-132 and miR-146a from *in vitro* cultured acute monocytic leukemia cells (THP-1) related to innate immune responses [216]. At the low miRNA concentrations required for clinical diagnostics, amplified TG-FRET provided both better specificity (distinction of single-nucleotide variations at varying positions within the target) and higher precision (smaller distribution of concentrations and better distinction between healthy and pathological samples) than the gold standard method RT-qPCR.

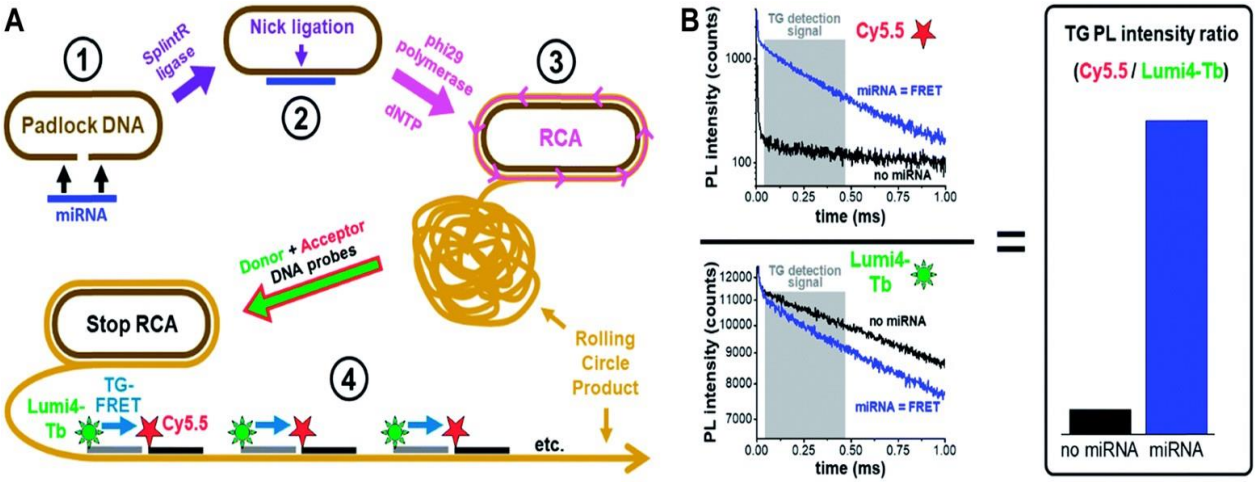

Figure 3.1 Principle of miRNA detection by amplified TG-FRET. (A) After specific recognition of miRNA by a linear padlock DNA (1), the DNA padlock nick is ligated over the miRNA target splint using SplintR ligase (2) and the miRNA becomes a primer for a phi29 polymerase to synthesize and displace (by RCA) complimentary DNA around the circularized padlock DNA (3). After stopping RCA, the rolling circle product (RCP) is incubated with Tb (Lumi4-Tb) donor and Cy5.5 acceptor labeled ssDNA, which hybridize to specific sequences that exist more than 1000-fold on the amplified RCP concatemer. The close distance of Lumi4-Tb and Cy5.5 in the RCP allows for Tb-to-Cy5.5 FRET, which is not possible if both are free in solution (not hybridized to the RCP). Thus, the TG-FRET signal can be used for quantifying miRNA without any washing or separation steps. (B) Ratiometric TG-FRET, which measures the ratio of FRET-sensitized Cy5.5 PL and FRET-quenched Tb PL within a specific time-window after pulsed excitation (to suppress autofluorescence), is used to quantify the miRNA target in a 140 µl microwell within 5 seconds.

3.2 Materials and methods

3.2.1 Nucleic acid probes and exogenous targets

All sequences and modifications of nucleic acids are summarized in **Table 3.1**. All oligonucleotides were purchased from Eurogentec. Phosphate DNAs were purified with polyacrylamide gel electrophoresis. All other modified DNAs and RNAs were purified with HPLC. Lumi4-Tb-NHS (Tb-NHS) was provided by Lumiphore, Inc. Tb-DNA conjugates were obtained by mixing Tb-NHS in concentration excess to amino-functionalized oligonucleotides in 100 mM carbonate buffer at pH 9.0. The mixtures were incubated

overnight at 4 °C. The Tb-DNA conjugates were purified 3 times with HEPES buffer (100 mM, pH 7.4) by Zeba Spin Desalting Columns (7 kDa MWCO). Tb concentrations were determined by absorbance measurements at *ca.* 340 nm using a molar absorptivity of *ca.* 26,000 $M^{-1}cm^{-1}$ as provided by the manufacturer. DNA was quantified by absorbance measurements at *ca.* 260 nm. Conjugation ratios were determined by linear combination of the respective absorbance values of Tb and oligo within the Tb-oligo conjugates and were in all cases higher than 0.9 Tb/DNA.

Table 3.1 Sequences and modifications of all DNA and RNA probes and targets. Sequence differences shown in red, sequence similarities shown in magenta, target-specific termini of padlock DNA shown in blue, Tb-probe-complementary sequences shown in green, and Cy5.5-probe-complementary sequences shown in orange.

Probe	Sequence 5'-3'	Modification
miR-21	UAG CUU AUC AGA C UGA UGU UGA	
miR-146a	UGA GAA CUG AAU UCC AUG GGU U	
miR-132	UAA CAG UCU ACA GCC AUG GUC G	
pre-miR-21	UGU CGG G UAG CUU AUC AGA CUG AUG UUG A CUG UUG AAU CUC AUG GCA ACA CCA GUC GAU GGG CUG UCU GAC A	
miR-21_{10} (A→G)	UAG CUU AUC GGA CUG AUG UUG A	
miR-21_{4} (C→U)	UAG UUU AUC AGA CUG AUG UUG A	
miR-21_{17} (U→A)	UAG CUU AUC AGA CUG AAG UUG A	
RNA_{int} (terminal)	UAA AGU GCU UAU AG UGA UGU UGA	
RNA_{int} (internal)	UAA AGU GCU UAU AG UGA UGU UGA GCA GGU AG	
padlock-21	TGA TAA GCT A ATA TAT GAT GG AAT CAA GAC AAT ATT GTT GAT GCC GAA TTT TTC AAG AG GAA ATG T TCA ACA TCA GTC	5'-Phosphate
padlock-146a	TTC AGT TCT CA ATA TAT GAT GG AAT CAA GAC AAT ATT GTT GAT GCC GAA TTT TTC AAG AG GAA ATG T AAC CCA TGG AA	5'-Phosphate
padlock-132	GTA GAC TGT TA ATA TAT GAT GG AAT CAA GAC AAT ATT GTT GAT GCC GAA TTT TTC AAG AG GAA ATG T CGA CCA TGG CT	5'-Phosphate
Tb-probe	AAT CAA GAC AAT ATT GTT	5'-C6 amino
Cy5.5-probe	GAT GCC GAA TTT TTC AAG AG	5'-Cy5.5

3.2.2 Photophysical analysis

Absorption spectra (Lambda 35 UV/Vis System, PerkinElmer) and emission spectra (FluoTime 300, PicoQuant) were recorded in HEPES buffer (100 mM, pH 7.4) and deionized water (purifiedby Purelab Option-Q equipped with bio-filter, ELGA LabWater) for Tb and Cy5.5 samples, respectively. All spectra are shown in **Figure 3.2**.

Förster distance (the donor-acceptor distance for which FRET is 50 % efficient) was $R_0 = 5.8 \pm 0.2$ nm and calculated using the **Equation 3.1**:

$$R_0 = 0.02108\left(\kappa^2 \Phi_D n^{-4} J(\lambda)\right)^{1/6} \text{ nm} \tag{3.1}$$

The orientation factor $\kappa^2 = 2/3$ because of random orientation of donor and acceptor during the FRET time (dynamic averaging), which is well justified by the long PL lifetime of the Tb donors and the unpolarized emission (fast isotropic rotation). The refractive index was $n = 1.35$ (aqueous buffer solution). The Tb-centered quantum yield was $\Phi_D = 0.80 \pm 0.05$. The overlap integral J was calculated by **Equation 3.2**:

$$J = \int_{475\,nm}^{700\,nm} \bar{I}_D(\lambda)\, \varepsilon_A(\lambda)\, \lambda^4 d\lambda \tag{3.2}$$

where $\bar{I}_D(\lambda)$ is the emission intensity from the area-normalized (to unity) emission spectrum of Tb donor and $\varepsilon_A(\lambda)$ is the molar absorptivity of the acceptor.

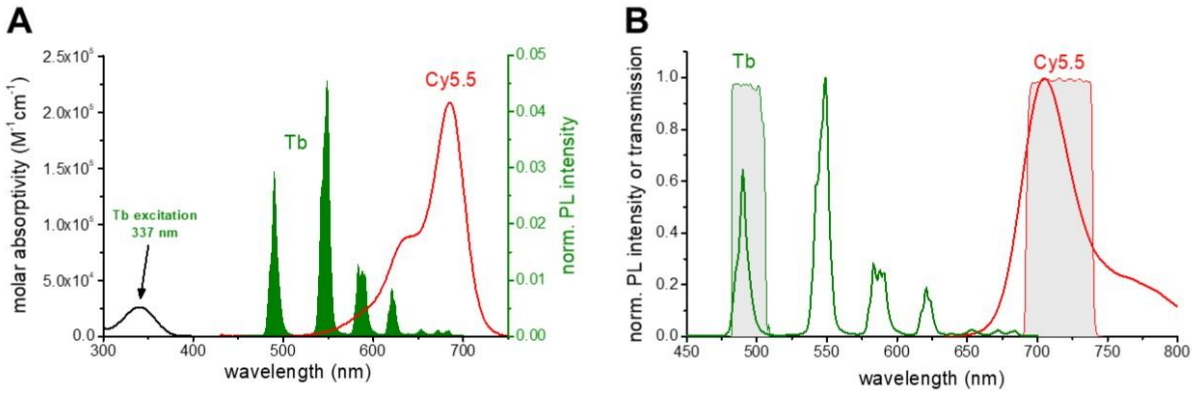

Figure 3.2 Absorption and emission spectra of the TG-FRET pair. (A) Spectra of Tb absorption (black) and emission (green) that partly overlaps with the absorption of Cy5.5 (red). (B) Emission spectra of Tb (green) and Cy5.5 (red). Optical bandpass filter transmission spectra, which represent the detection channels for Tb and Cy5.5, are shown in gray.

3.2.3 Statistical analysis

For statistical analysis and the estimation of LODs, all samples were prepared 3 times and measured in triplicates ($n = 9$) apart from the zero-concentration samples (without miRNA targets), which were prepared 10 times and measured in triplicates ($n = 30$). For specificity tests, all samples were prepared and measured once. For real sample detections, all samples were prepared in duplicate and measured once ($n = 2$). All RT-qPCR measurements were performed in duplicate and measured once ($n = 2$).

3.2.4 Amplified TG-FRET miRNA assays

In a typical assay, 1.5 nM padlock probe and an appropriate amount of the target miRNA were prepared in 10 µl optimized SplintR DNA ligase reaction buffer (BUFFER-1, 50 mM Tris–HCl, 10 mM $MgCl_2$, 100 mM NaCl, 10 µM ATP, 10 mM DTT, pH 7.6), and the mixture was incubated in a thermal cycler with a temperature control program (80 ℃ for 2 min, decreased from 80 ℃ to 22 ℃ with a 2 ℃ min^{-1} speed). Then, 21.5 U of SplintR DNA ligase (New England Biolabs) prepared in 5 µl BUFFER-1 was added to the mixture and incubated at 37 ℃ for 1 h. Afterwards, 15 µl phi29 DNA polymerase reaction buffer (BUFFER-2, 1× buffer components: 50 mM Tris-Cl, 10 mM $MgCl_2$, 10 mM $(NH_4)_2SO_4$, 4 mM DTT, pH 7.4), which contained 5 U of phi29 DNA polymerase (New England Biolabs) and 0.5 mM dNTP (New England Biolabs), was added and incubated at 37 ℃ for 3 h. Before termination of the polymerization process, 2.5 nM Tb probe and 2.5 nM Cy5.5 probe prepared in 120 µl hybridization buffer (BUFFER-3, 20 mM Tris-Cl, 500 mM NaCl, 0.1% BSA, pH 8.0) were added and then incubated in a thermal cycler with a temperature control program (65 ℃ for 10 min, decreased from 65 ℃ to 22 ℃ with a 2 ℃ min^{-1} speed, 22 ℃ for 10 min). From the total reaction volume of 150 µl, 140 µl were measured in 96-well microtiter plates on the clinical immunofluorescence plate reader KRYPTOR (Thermo Fisher Scientific) with time-gated (0.1-0.9 ms) PL intensity detection using optical bandpass filters (Semrock) with 494 ± 12 nm for the Tb detection channel and 716 ± 24 nm for the Cy5.5 detection channel.

3.2.5 RNA extraction

Tissue material was obtained with informed consent at the Medical University of Graz and the St. John of God Hospital Graz under approval from the ethics committee of the Medical University of Graz and the ethics committee of the St. John of God Hospital Graz (23-015 ex 10/11). All breast tissue samples were gathered in course of routine interventions and autopsies, respectively, and used in an anonymized/pseudonymized way. The use was approved by the responsible ethics committee. All plasma samples were collected from anonymized patients with written informed consent under the agreement of the responsible ethical committees (official permission n° 2746 by the "comité de protection des personnes Ile de France III" – January 5, 2010). For all plasma samples, miRCURY™ RNA Isolation Kit-Biofluids (Exiqon) was used for the extraction of small RNA. The extraction was performed according to the manufacturer's instructions. In a typical experiment, 250 µl of each plasma sample was centrifuged at 3000g for 5 min to pellet any debris and insoluble components after thawing. 200 µl of supernatant was transferred to a new tube and 60 µl Lysis solution and 1.2 µl MS2 RNA (Sigma-Aldrich) were added into the solution for 3 min at room temperature to lyse plasma components. After that, 20 µl protein precipitation solution was added for 1 min at room temperature. The precipitated mixture was centrifuged for 3 min at 11,000g and the clear supernatant was transferred into a new collection tube. Then, 270 µl isopropanol was added to the collected supernatant, and the solution was loaded to a microRNA Mini Spin Column for 2 min at room temperature. After centrifuging for 30 s at 11,000g, the solution was washed once with 100 µl washing solution 1 and twice with washing solution 2 (700 µl and 250 µl). Finally, the RNA was eluted with 50 µl RNase free water, and all RNA extractions were stored at −80 °C. Total RNA was isolated from snap-frozen human breast tissue samples using Trizol reagent (Life Technologies), followed by extraction with phenol-chloroform. THP-1 cells were grown in RPMI 1640 supplemented with 10% fetal calf serum, 1% penicillin/streptomycin, and L-glutamine. THP-1 cells were not treated (0 h) or treated for 24 h (24 h) with LPS (1 µg ml^{-1}). Total RNAs were extracted using a miRNeasy Mini Kit with a Qiacube (QIAGEN), according to

the manufacturer's instructions. RNA concentrations were assessed using a NanoDrop spectrophotometer (Thermo Fisher Scientific, Waltham, USA). Total RNA concentrations and available volumes of all samples are given in **Table 3.2**. Relevant information on human research participant are given in **Table 3.3**.

Table 3.2 Total RNA concentrations and sample volumes of clinical samples. Corresponding Figures are shown on the left hand column.

Figure	Extraction from	Sample name	Total RNA concentration (ng μl^{-1})	Available volume (µl)
3.6a	Plasma	Control 1	14	50
	Plasma	Control 2	13	50
	Plasma	Control 3	10	50
	Plasma	Control 4	11	50
	Plasma	Control 5a (experiment 1)	12	50
	Plasma	Control 5b (experiment 2)	17	50
	Plasma	Control 6	13	50
	Plasma	Control 7	9	50
	Plasma	Control 8	11	50
	Plasma	Control 9	10	50
	Plasma	Control 10	11	50
	Plasma	Control 11	15	50
	Plasma	Control 12	19	50
	Plasma	Ovarian cancer 1	8	50
	Plasma	Ovarian cancer 2	15	50
	Plasma	Ovarian cancer 3	11	50
	Plasma	Ovarian cancer 4	13	50
	Plasma	Ovarian cancer 5	15	50
	Plasma	Ovarian cancer 6a (experiment 1)	10	50
	Plasma	Ovarian cancer 6b (experiment 2)	15	50
	Plasma	Ovarian cancer 7	11	50
	Plasma	Ovarian cancer 8	14	50
	Plasma	Ovarian cancer 9a (experiment 1)	12	50
	Plasma	Ovarian cancer 9b (experiment 2)	14	50
	Plasma	Ovarian cancer 10	12	50
	Plasma	Ovarian cancer 11	15	50
3.6b	Tissue	Control 1	133	26
	Tissue	Control 2	204	28
	Tissue	Control 3	160	28
	Tissue	Control 4	456	28
	Tissue	Breast tumor 1	1149	56
	Tissue	Breast tumor 2	44	28
	Tissue	Breast tumor 3	163	28
	Tissue	Breast tumor 4	1113	28
	Tissue	Breast tumor 5	916	28
	Tissue	Breast tumor 6	77	28
3.6c	Cells	0 h - 0.25 mio cells	203	30
	Cells	24 h - 0.25 mio cells	172	30
	Cells	0 h - 3 mio cells	180	180
	Cells	24 h - 3 mio cells	136	180

Table 3.3 Relevant information on human research participants.

Plasma samples						
Sample	**Gender**	**Age**	**Pathology**	**Tumor stage**	**BRCA status**	**Treatment modalities**
13858	Female	52	None	None	Wild type	None
13993	Female	49	None	None	Wild type	None
14214	Female	42	None	None	Wild type	None
14168	Female	32	None	None	Wild type	None
14237	Female	52	None	None	Wild type	None
14267	Female	51	None	None	Wild type	None
14270	Female	25	None	None	Wild type	None
14394	Female	35	None	None	Wild type	None
14483	Female	56	None	None	Wild type	None
16400	Female	49	None	None	Wild type	None
17919	Female	43	None	None	Wild type	None
18189	Female	49	None	None	Wild type	None
EXO015	Female	66	HGSOC	IIIc	Wild type	Neo-adjuvant chemotherapy, followed by debulking surgery and adjuvant chemotherapy
EXO018	Female	55	HGSOC	IIIb	Wild type	Direct debulking surgery and adjuvant chemotherapy
EXO025	Female	71	HGSOC	IIIc	Wild type	Neo-adjuvant chemotherapy, followed by debulking surgery and adjuvant chemotherapy
EXO045	Female	66	HGSOC	Ia	Wild type	Direct debulking surgery and adjuvant chemotherapy
EXO050	Female	63	HGSOC	IIIc	Unknown	Direct debulking surgery and adjuvant chemotherapy
EXO069	Female	55	HGSOC	IIIc	Unknown	Neo-adjuvant chemotherapy, followed by debulking surgery and adjuvant chemotherapy
EXO075	Female	58	HGSOC	IIIc	BRCA1	Direct debulking surgery and adjuvant chemotherapy
EXO079	Female	59	HGSOC	IIIc	Unknown	Neo-adjuvant chemotherapy, followed by debulking surgery and adjuvant chemotherapy
EXO0122	Female	61	HGSOC	IIIc	Unknown	Neo-adjuvant chemotherapy, followed by debulking surgery and adjuvant chemotherapy
EXO0129	Female	73	HGSOC	IIIc	Wild type	Neo-adjuvant chemotherapy, followed by debulking surgery and adjuvant chemotherapy
EXO0141	Female	39	HGSOC	IIIc	Wild type	Chemotherapy alone

Tissue samples						
Sample	**Gender**	**Age**	**Pathology**	**Tumor stage**	**Receptor status**	**Treatment modalities**
nnB1	Female	55	material far away from nB1 tumor	-	-	see nB1
nnB2	Female	78	no history of breast cancer	-	-	no breast cancer-specific treatment
nnB3	Female	80	no history of breast cancer	-	-	no breast cancer-specific treatment
nnB4	Female	70	history of breast cancer for the not sampled breast (more than 10 years ago)	-	-	no breast cancer-specific treatment for more than ten years
nB1	Female	55	poorly differentiated invasive breast cancer without special subtype, metastasising	apT-4b, G-3, V-1, L-1, pM-1	estrogen receptor: moderately positive, progesterone receptor: moderately positive, no Her2 overexpression	no surgery, no breast cancer-specific treatment
nB2	Female	49	highly differentiated invasive ductal breast cancer	G1 pT1c(m) N1mi (1/3;sn)	estrogen receptor: positive, progesterone receptor: positive, no Her2 overexpression	direct surgery (sampling), post operative radiation therapy, adjuvant anti-hormone therapy
nB3	Female	50	moderately differentiated invasive ductal breast cancer	pT1c, G2, pN0(sn, 0/1) pTis(DCIS), G2	estrogen receptor: positive, progesterone receptor: positive, no Her2 overexpression	direct surgery (sampling), post operative radiation therapy, adjuvant anti-hormone therapy
nB4	Female	65	poorly differentiated invasive ductal breast cancer, metastasising	G3 pT4b L1	estrogen receptor: positive, progesterone receptor: negative, no Her2 overexpression	direct surgery (sampling), post operative radiation therapy, palliative adjuvant anti-hormone therapy
nB5	Female	47	moderately differentiated invasive ductal breast cancer	G-2, pT-X	estrogen receptor: positive, progesterone receptor: positive, no Her2 overexpression	direct surgery (sampling), post operative radiation therapy, adjuvant chemotherapy, adjuvant anti-hormone therapy
nB6	Female	77	moderately differentiated invasive ductal breast cancer	G2 pT2	estrogen receptor: positive, progesterone receptor: moderately positive, no Her2 overexpression	direct surgery (sampling), post operative radiation therapy, adjuvant anti-hormone therapy

3.2.6 Absolute quantification of miRNA by amplified TG-FRET

Absolute concentrations of unknown miRNAs were determined by using a calibration curve (FRET-ratio over concentration) constructed with the use of synthetic miRNAs with known concentrations (between 0.05 and 1.0 pM within 140 µl solutions). Unknown miRNAs were diluted at different dilution factors to be sure that their concentration range fitted the one of the calibration curves.

3.2.7 RT-qPCR miRNA assays

TaqMan MicroRNA Assay Kits (Thermo Fisher) were used for all RT-qPCR experiments. All plasma RNA extracts were diluted five times. Breast cancer tissue RNA extracts were diluted to 0.5 ng μl^{-1} of total RNA, except for breast tumor samples 3, 4, and 6 (**Table 3.2**), which were diluted to 0.25 ng μl^{-1} of total RNAs. All other RNA extracts were diluted to 2 ng μl^{-1} of total RNA. RT reactions were carried out with a *TaqMan* MicroRNA Reverse Transcription Kit (Thermo Fisher) in 15 µl containing 5 µl of RNA extract, 0.15 µl of 100 mM dNTPs, 1 µl of Multiscribe reverse Transcriptase (50 U μl^{-1}), 1.5 µl of 10× reverse transcription buffer, 0.19 µl of RNase inhibitor (20 U μl^{-1}), 3 µl of gene-specific primer, and 4.16 µl of nuclease-free water. For synthesis of cDNA, the reaction mixtures were incubated at 16 ℃ for 30 min, at 42 ℃ for 30 min, at 85 ℃ for 5 min, and then held at 4 ℃. Then, 1.33 µl of cDNA solution was amplified using 10 µl of *TaqMan* Universal PCR Master Mix II with UNG (Thermo Fisher), 1 µl of gene-specific primer and probe, and 7.67 µl of nuclease-free water in a final volume of 20 µl. Quantitative PCR was run on a PikoReal Real-Time PCR System (Thermo Fisher Scientific), and the reaction mixtures were incubated at 95 ℃ for 10 min, followed by 40 cycles of 95 ℃ for 15 s and 60 ℃ for 1 min. The quantitation cycles (C_q) were calculated with PikoReal software (Thermo Scientific). Absolute concentrations of unknown miRNAs were determined by using a calibration curve (C_q over concentration) constructed with the use of synthetic miRNAs with known concentrations.

3.3 Results and discussion

3.3.1 Sensitivity and dynamic range

To quantify miRNA, amplified TG-FRET technology applies time-gated (0.1-0.9 ms after pulsed excitation) ratiometric PL intensity (FRET-ratio) detection (**Figure 3.1B**) of Cy5.5 acceptors and Lumi4-Tb (Tb) donors (*cf.* **Figure 3.2** for absorption/emission spectra and FRET parameters), which only takes a few seconds on a KRYPTOR immunofluorescence plate reader. We first evaluated the performance for miRNA quantification on exogenous miR-21, miR-132, and miR-146a. SplintR ligase was used for efficient ligation of the DNA padlock probes over the miRNA targets. Although shorter padlock probes were shown to exhibit higher fluorescence intensities in RCA-FRET [212], we chose padlock probes of 77 and 78 nucleotides (see **Table 3.1** for sequences of all RNAs and DNAs used in the study). These relatively long DNAs allowed us to avoid overlap between the sequences that recognized the miRNA targets and those that hybridized the Tb-donor and dye-acceptor DNA probes and to optimize the FRET distance between Tb and dye inside the RCA product. The actual Tb-dye distance in the rolling circle product (RCP, **Figure 3.1A**) was 18 base pairs (see **Table 3.1** for complementary sequences between the padlock and the Tb and dye probes). This distance would correspond to *ca.* 7 nm when using 0.34 nm per base pair and 0.4 ± 0.1 nm for both Tb and Cy5.5 and was shown to be in excellent agreement with time-resolved FRET measurements on dsDNA [217]. When comparing the PL decays of the Tb-Cy5.5 FRET pair inside the RCP and inside dsDNA (**Figure 3.3**), the average FRET-sensitized PL lifetime is significantly shorter for the RCP FRET-pair (0.4 ms *vs.* 2 ms), which means that the average FRET efficiency is higher (0.86 *vs.* 0.28). This difference can be explained by the folded (coiled) structure of the RCP and a concomitant closer donor-acceptor distance and/or the interaction of one donor with several acceptors, both of which lead to higher FRET efficiencies. Despite the different behavior of the Tb-dye FRET pair in a folded RCP concatemer, donor-acceptor distance adjustment (different number of base pairs between Tb and dye) can still be used to produce distinct PL decays that are applicable for multiplexed nucleic acid detection [171]. Another practical reason

of the non-overlapping sequences for miRNA targets and fluorescent probes was the usability of the same Tb-donor and dye-acceptor probes for different miRNA targets (see color code in **Table 3.1**). Taking into account the many different miRNAs that have been related to various cancers, this versatile padlock design is an important advantage for diagnostic applications.

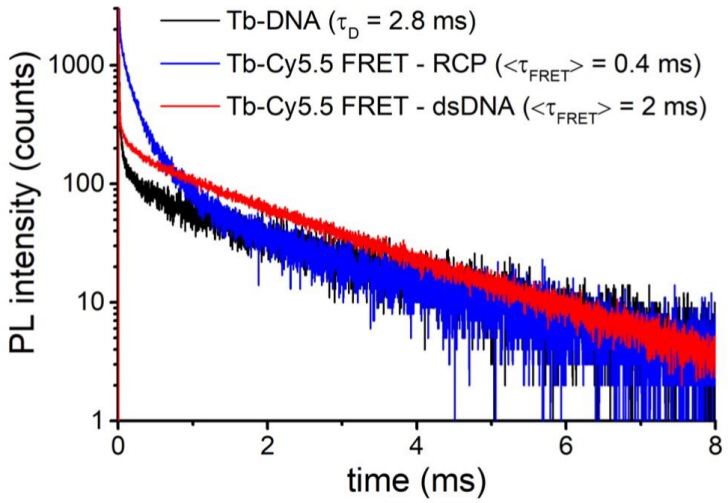

Figure 3.3 PL decays of Cy5.5 for a Tb-Cy5.5 donor acceptor pair at 18 base pairs distances in a dsDNA (red curve) and in a RCP concatemer (blue curve). A PL decay curve of Tb alone (black curve, no Cy5.5 present) is shown for comparison and for intensity normalization of the two PL decays (intensity normalized in the temporal region between 7 and 8 ms). The PL decay time of the donor in the absence of the acceptor (τ_{DA}) and of the acceptor in the presence of the donor (average FRET decay time <τ_{FRET}>) are given inside the graph.

For all three miRNA targets the calibration curves (**Figure 3.4A**) showed increasing FRET-ratio values with increasing miRNA concentrations. Limits of detection (LODs) were determined (three standard deviations over the blank sample) as 4.2 ± 0.5 attomole (30 ± 3 fM) for miR-21, 6.8 ± 0.8 attomole (48 ± 5 fM) for miR-132, and 14 ± 2 attomole (99 ± 10 fM) for miR-146a (**Figure 3.4B**) and the dynamic concentration range spanned more than 3 orders of magnitude (~50 fM to ~50 pM, **Figure 3.4C**).

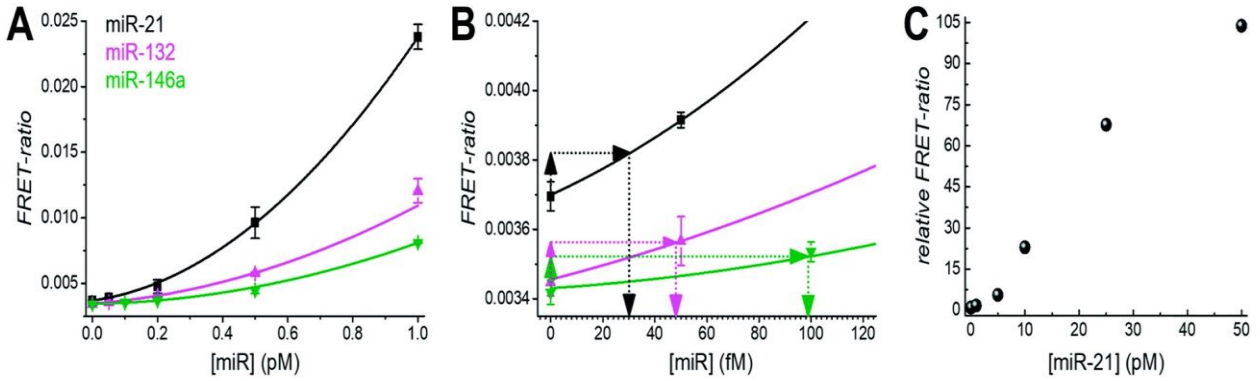

Figure 3.4 (A) Calibration curves for miR-21, miR-132, and miR-146a for concentrations between 0.05 and 1.0 pM within 140 µl solutions per microwell. (B) Enlarged view of the same calibration curves in the 0 to 120 fM concentration range. LODs were determined as shown (using 3 standard deviations of the blank) to 30 ± 3 fM for miR-21, 48 ± 5 fM for miR-132, and 99 ± 10 fM for miR-146a. (C) Assay calibration curve of miR-21 over a larger concentration range (up to 50 pM) to assess the dynamic range of amplified TG-FRET assays.

3.3.2 Specificity and comparison to RT-qPCR

Another important requirement for diagnostics is specificity at very low concentrations, which we verified by challenging the miR-21 assay with various amounts of pre-miR-21 as well as three modified miR-21 targets with single nucleotide variations at different positions (**Figure 3.5A**). Compared to samples without target, pre-miR-21 did not lead to any signal increase for TG-FRET (red curve in **Figure 3.5B**) but significantly reduced quantification cycles (C_q) for RT-qPCR (red curve in **Figure 3.5C**), which will lead to an overestimation (positive offset) of the real miR-21 target concentration (the lower the C_q the higher the measured concentration). Although the C_q values for the miR-21 target were much lower (black curve in **Figure 3.5C**), the nonspecific pre-miR-21 signal suggests that the internal miR-21 sequence of pre-miR-21 (with additional 7 bases on the 50 end and 43 bases on the 30 end) can still be reverse transcribed and amplified by RT-qPCR albeit with much lower efficiency compared to miR-21. For TG-FRET, it is very likely that the miR-21 sequence inside pre-miR-21 will be specifically hybridized by the padlock DNA. However, the two 3' and 5' overhangs prevent amplification by the phi29 polymerase.

Although it was shown that phi29 polymerase can provide 3' to 5' RNA exonucleolytic activity, the efficiency was ~10-fold lower than for DNA [218]. We therefore assume that, under our experimental conditions, the additional 43 bases on the 3' end cannot be hydrolyzed efficiently enough to initiate RCA. Concerning the single-nucleotide variations of miR-21, only miR-21_{17} (U→A) at concentrations higher than 6 pM led to a significant miR-21 signal for TG-FRET (green curve in **Figure 3.5B**). This nonspecific signal resulted from a single-nucleotide variation at a distant position from the padlock nick on the longer (12 nt) target-recognizing terminus of the padlock DNA (**Figure 3.5A**). The versatility of the padlock design can overcome even such particular mismatches. Moving the nick closer to the mismatch and/or shortening the length of the mismatch-recognizing terminus (10 nt) completely removed the non-specific signal as shown by two other mismatched miR-21 variants (miR-21_{10} (A→G) and miR-21_4 (C→U) - blue and magenta curves in **Figure 3.5B**). In contrast, the gold standard RT-qPCR was strongly influenced by all three mismatched miR-21 (**Figure 3.5C**). Although the quantification cycles (C_q) were distinguishable from the original miR-21 target, they significantly decreased to values far below that seen without any target. While such mismatches will result in a positive offset of the real miR-21 target concentration, the RT step of RT-qPCR can lead to negative concentration offsets. The presence of internal or terminal RNA sequences that are complementary to the very short hybridization sequence (~6 to 8 nt) of the RT stem-loop primer may be recognized by the RT primer and therefore reduce RT efficiency and produce less cDNA (**Figure 3.5D**). Indeed, both internal and terminal complementary sequences of otherwise unrelated RNAs led to a significant decrease in the measured miR-21 concentrations (**Figure 3.5E**). Such short sequences that are complementary to the RT stem-loop primer may exist in many different RNAs present in real clinical samples and present a serious drawback for RT-qPCR-based diagnostics. These results clearly show another important advantage of amplified TG-FRET when it comes to clinical applications.

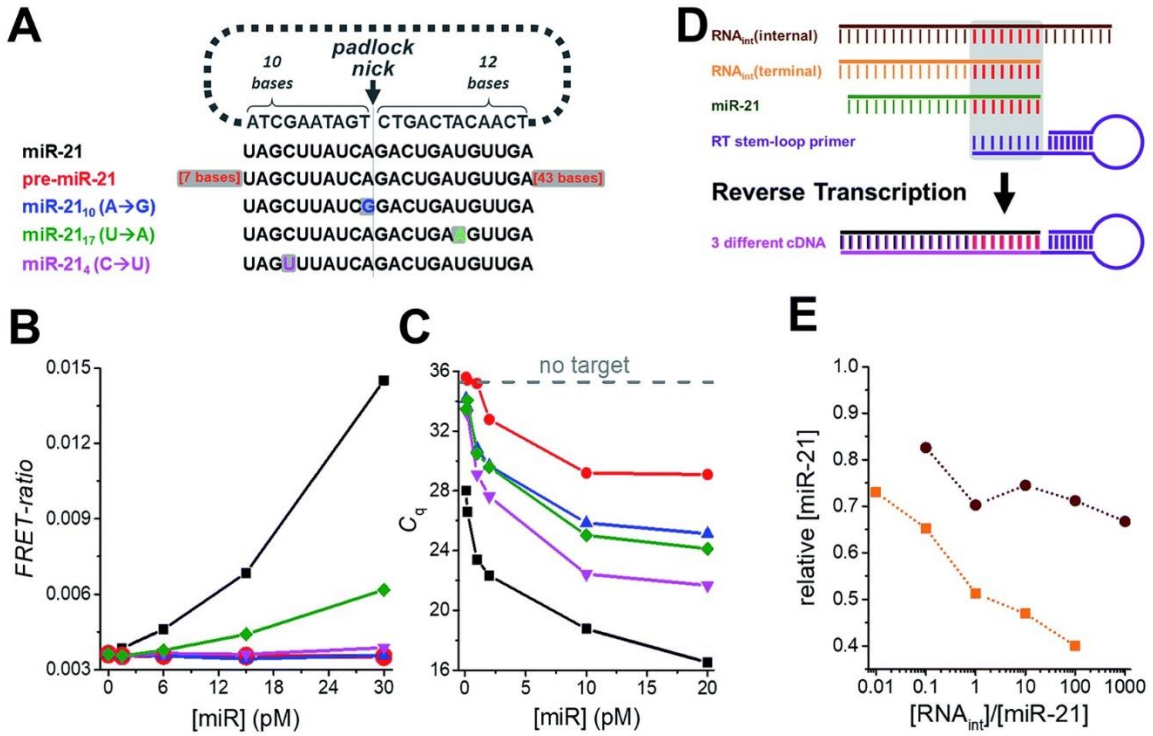

Figure 3.5 (A) The specificity of amplified TG-FRET and TaqMan RT-qPCR for miR-21 (black) was challenged against pre-miR-21 (red) and three different targets with single nucleotide variations compared to miR-21 (blue, green, and magenta). (B) For amplified TG-FRET, only the mismatch at a remote position from the padlock nick on the longer (12 nt) target-recognizing terminus led to a nonspecific signal at elevated concentrations of miRNA (miR-21_{17} (U→A), green curve). The versatile probe design can overcome this problem by using a padlock probe with a nick closer to the mismatch (miR-21_{10} (A→G), blue curve) or with the shorter target-recognizing terminus (10 nt) over the mismatch (miR-21_4 (C→ U), magenta curve). Pre-miR-21 (red curve) did not lead to any nonspecific signal either. The black curve shows the signal for the miR-21 target (without any mismatches). (C) TaqMan RT-qPCR is strongly influenced by pre-miR-21 (red curve) and all three single nucleotide variations (blue, green, and magenta curve), as shown by decreasing quantification cycles (C_q) with increasing mismatch concentrations (within the same low picomolar miRNA concentration range as for TG-FRET - *cf.* graph in B). Gray dashed line indicates C_q value for samples without target. (D) The short target-hybridization sequence of the TaqMan RT-stem loop primer can lead to reverse transcription of RNA that have the same internal or terminal sequence than the target terminus. (E) Both internal and terminal interfering sequences led to negative offsets (down to 40% for RNA_{int} (terminal)) of the target concentration (10 pM).

3.3.3 MiRNA detection in human plasma, tissue, and cells

To demonstrate immediate applicability of amplified TG-FRET to biologically relevant samples and research (**Figure 3.6**), we quantified hsa-miR-21 in 26 plasma samples related to ovarian cancer (13 samples from ovarian cancer patients and 13 samples from healthy individuals), hsa-miR-21 in 10 tissue samples related to breast cancer (4 healthy tissues and 6 primary tumor tissues), and hsa-miR-132 and hsa-miR-146a in lysate samples from 0.25 × 10^6 and 3 × 10^6 THP-1 cells stimulated with lipopolysaccharide (LPS) for 0 h or 24 h. For comparison, all samples were also quantified with TaqMan RT-qPCR.

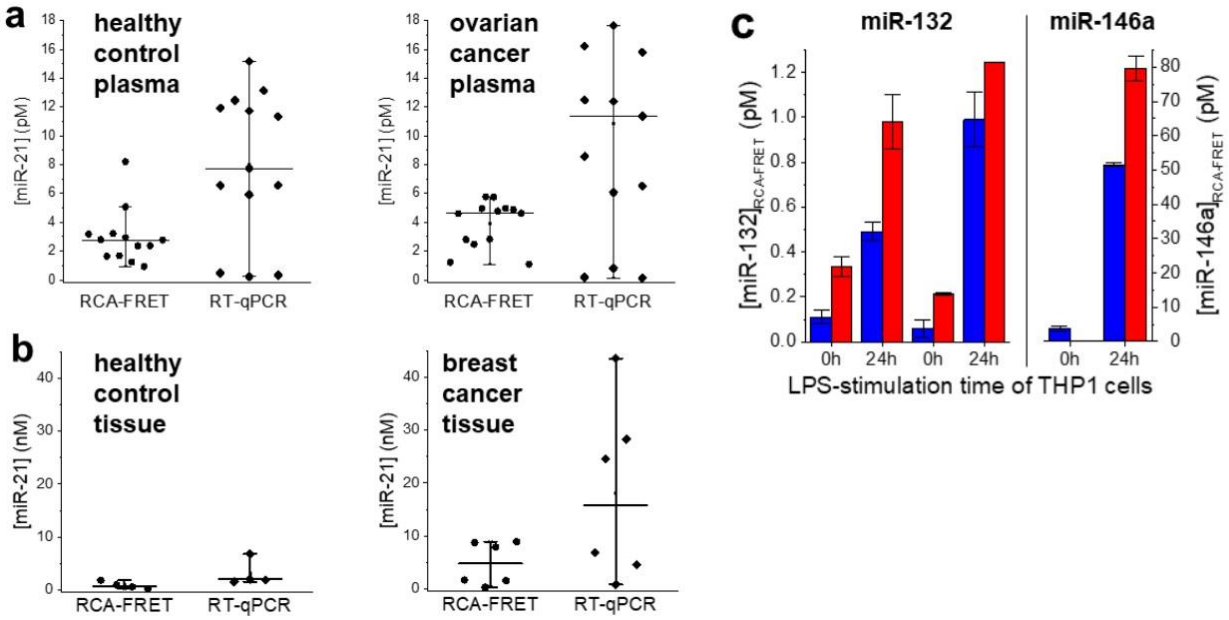

Figure 3.6 Absolute concentrations (pM) of miR-21 in 26 plasma samples related to ovarian cancer (a), and that (nM) in 10 tissue samples related to breast cancer (b). (c) Absolute concentrations (pM) of miR-132 (left) and miR-146a (right) in LPS-stimulated THP-1 cells. All samples were also quantified with TaqMan RT-qPCR (red columns in graph c).

Plasma samples are arguably the most challenging for miRNA-based diagnostics because of the low miRNA concentrations and the large variations in miRNA expression. As shown in **Figure 3.7A**, amplified TG-FRET values provided a much narrower distribution of concentrations compared to RT-qPCR. When applying a threshold value (maximum concentration in healthy samples without outliers), TG-FRET could reveal a significant difference between healthy and ovarian cancer samples (62% above and 38% below threshold line), whereas RT-qPCR showed only minor differences (17% above and 83% below threshold line). Comparing all samples in a scatter plot (TG-FRET *vs.* RT-qPCR concentrations, **Figure 3.7B**) showed the difference between both techniques. Although samples were distributed below and above the ideal 1:1 line, a trend toward higher RT-qPCR concentrations (~3:1) became evident. The scatter plot also showed a large concentration distribution of both healthy and cancer samples and the better distinction of cancer and healthy samples for TG-FRET. Although the results showed a better analytical performance of TG-FRET, they also confirmed the challenges of miRNA quantification in plasma and that larger sample cohorts are necessary to provide a clear clinical conclusion [5]. Nevertheless, the outcome of this study on 26 different plasma samples clearly showed that amplified TG-FRET has a large potential to add significant advantages to clinical studies with large patient cohorts.

A narrower distribution of TG-FRET-determined concentrations was also found for breast cancer tissues (**Figure 3.8A**). Although we disposed fewer samples compared to plasma, a distinction of healthy from cancer samples was evident. One of the reasons may be the higher absolute concentrations (pM in plasma and nM in tissue) because RT-qPCR is known to be less precise at low target input [219]. Both amplified TG-FRET and RT-qPCR could very well distinguish healthy and cancer tissue (100% of healthy samples below threshold and 100% of cancer samples above threshold). Similar to the plasma results, miR-21 concentration values for RT-qPCR were significantly higher (also approximately 3-fold) compared to TG-FRET but there was much less distribution in the scatterplot when comparing both techniques (**Figure 3.8B**). Although the patient cohort was relatively small, the results clearly show that amplified TG-FRET can provide very useful clinical

information (healthy or cancer) at a relatively simple workflow without reverse transcription and without interferences from reagents used in RNA extraction. TG-FRET may therefore be used as a stand-alone or complementary analytical method to accomplish higher precision in miRNA-based tissue diagnostics.

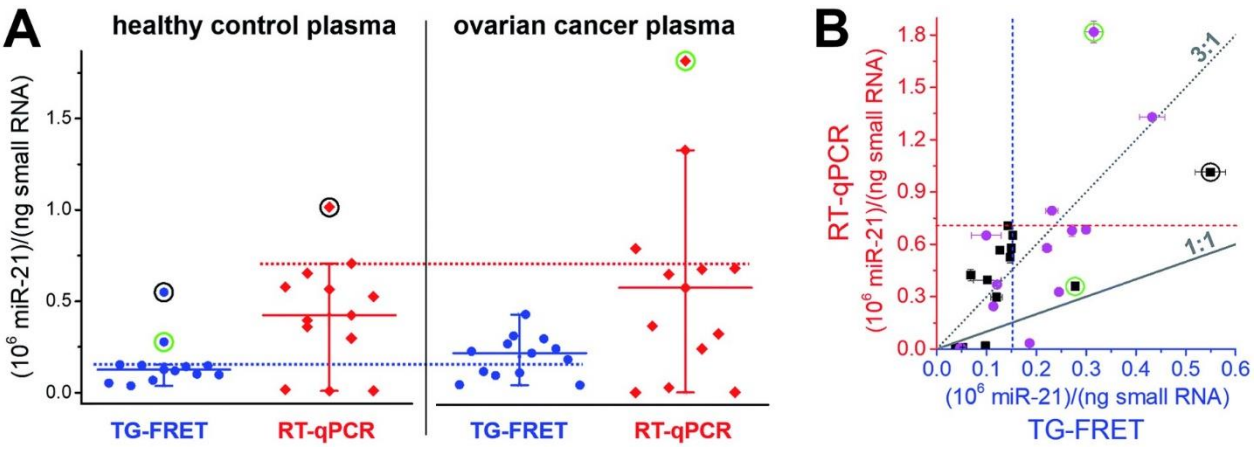

Figure 3.7 (A) Absolute quantification of hsa-miR-21 in human plasma (ovarian cancer) using amplified TG-FRET (blue) and RT-qPCR (red). MiR-21 concentrations (in small-RNA extracts) of 13 healthy control and 13 ovarian cancer samples were quantified. Circles around data points indicate statistical outliers (in green for only one of the techniques, in black for both techniques). Whiskers represent maximum and minimum values (without outliers) and horizontal lines represents the median. Dotted lines represent a threshold value (maximum of healthy control samples). More information about samples and human research participants can be found **Table 3.2** and **Table 3.3**. All concentrations are given in copy number per ng of small RNA. Absolute concentrations (pM) are shown in **Figure 3.6a**. (B) Scatterplot comparing RT-qPCR with TG-FRET concentrations for the same samples. Healthy samples are shown in black and cancer samples in magenta. For orientation, lines of perfect agreement (1:1) between the two techniques and 3-fold higher RT-qPCR values (3:1) are shown. Circles around data points indicate the statistical outliers from (A). Blue and red dashed lines present the threshold values from (A).

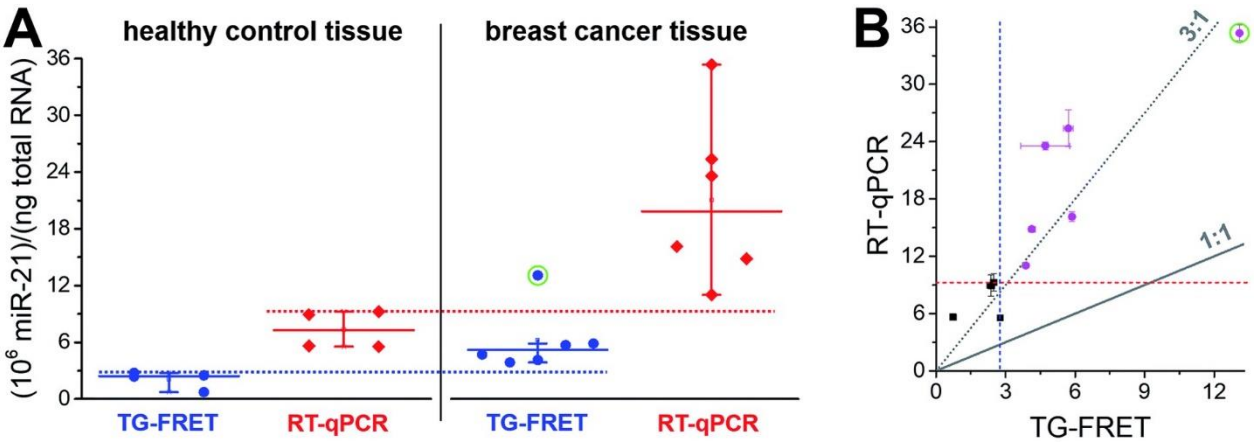

Figure 3.8 (A) Absolute quantification of hsa-miR-21 in human tissue (breast cancer) using amplified TG-FRET (blue) and RT-qPCR (red). miR-21 concentrations (in total-RNA extracts) of four healthy tissues (non-neoplastic breast) and six breast tumor tissues were quantified. Circle around data point indicates statistical outlier. Whiskers represent maximum and minimum values (without outlier) and horizontal lines represents the median. Dotted lines represent a threshold value (maximum of healthy control samples). More information about samples and human research participants can be found in **Table 3.2** and **Table 3.3**. All concentrations are given in copy number per ng of total RNA. Absolute concentrations (nM) are shown in **Figure 3.6b**. (B) Scatterplot comparing RT-qPCR with TG-FRET concentrations for the same samples. Healthy samples are shown in black and cancer samples in magenta. For orientation, lines of perfect agreement (1:1) between the two techniques and 3-fold higher RT-qPCR values (3:1) are shown. Circle around data point indicates the statistical outlier from (A). Blue and red dashed lines present threshold values from (A).

To demonstrate successful application of amplified TG-FRET beyond cancer diagnostics and for a third sample type, quantification of two other endogenous miRNAs (hsa-miR-132 and hsa-miR-146a) was performed in total-RNA extracts from LPS-stimulated THP-1 cells (**Figure 3.9**). LPS stimulation resulted in a significant increase in miR-132 concentrations for both smaller (250,000 cells) and larger (3×10^6 cells) amounts of cells. The higher amount of cells allowed us to produce more total-RNA but at approximately equal

concentrations (*cf.* **Table 3.2**). Similar to plasma and tissue measurements, concentration values were (2.4 ± 1.1)-fold higher for RT-qPCR compared to TG-FRET. These higher concentration values in all three types of clinical samples suggest that the positive concentration offset of RT-qPCR (*cf.* **Figure 3.5A-C**) caused by miRs with very similar sequences is significantly stronger than the negative concentration offset (*cf.* **Figure 3.5E**) caused by the RT step of RT-qPCR. Absolute concentrations (*cf.* **Figure 3.6**) were similar to plasma samples (pM concentration range). Average relative increases due to LPS stimulation were 5.3/22-fold and 3.5/7.8-fold (smaller/larger amounts of cells) for TG-FRET and RT-qPCR, respectively. The larger amount of cells was used for the quantification of miR-146a. Concentration values were 14-fold lower (no stimulation) and 1.5-fold higher (24 h stimulation) for RT-qPCR, and this time the relative increases due to LPS stimulation were 18-fold and 395-fold for TG-FRET and RT-qPCR, respectively. TG-FRET showed better agreement with a previous study, which reported that both miR-132 and miR-146a showed equivalent elevation and that the one of miR-146a was circa 8-fold (normalized to 5S RNA) [216]. Again, we used only few samples to demonstrate quantification of miRNAs in cells and though the results were more consistent for TG-FRET, a larger study would be necessary to confirm its better performance. However, similar to the tissue samples, we could clearly show (and verify by RT-qPCR) that TG-FRET can efficiently distinguish LPS-stimulated from non-stimulated cells and that this new technology has the potential to become a useful tool for cell-based miRNA diagnostics.

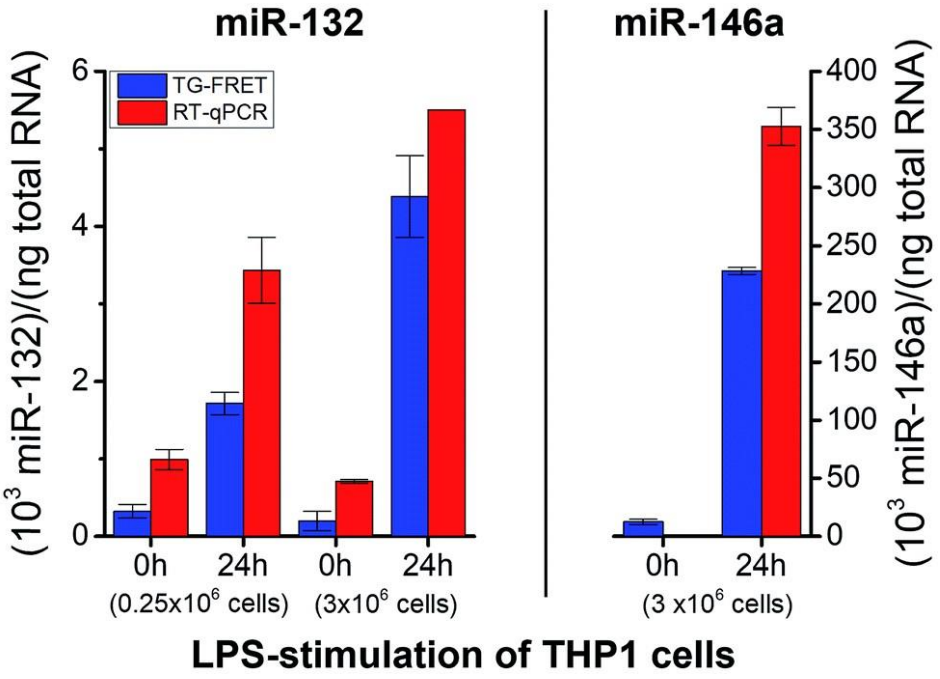

Figure 3.9 Absolute quantification of hsa-miR-132 and hsa-miR-146a in in vitro cultured cells (LPS stimulation) using amplified TG-FRET (blue) and RT-qPCR (red). miR-132 (left) and miR-146a (right) concentrations (in total-RNA extracts) of THP-1 cells after 0 h and 24 h of stimulation with LPS (1 μg ml^{-1}). Note: value of miR-146a for 0 h stimulation measured with RT-qPCR is 0.9 and therefore not visible within the concentration scale. More information about the samples can be found in **Table 3.2**. All concentrations are given in copy number per ng of total RNA. Absolute concentrations (pM) are shown in **Figure 3.6c**.

3.4 Conclusion

In this study, we have presented the development, characterization, and application of a new amplified TG-FRET technology for absolute quantification of miRNA. Amplified TG-FRET uses simple isothermal RCA and ratiometric TG-FRET detection for precise quantification on a commercial clinical plate reader (KRYPTOR). The rapid miRNA assay does not require any separation or washing steps and can directly quantify miRNA without reverse transcription to cDNA. To fulfill the technological and clinical requirements we designed TG-FRET for high sensitivity, specificity, and the use for quantifying miRNA from human plasma, tissues, and cells. Careful characterization of sensitivity and

specificity for miR-21, miR-132, and miR-146a revealed LODs down to 4.2 attomoles (30 fM), efficient distinction against single-nucleotide variations and pre-miRNA, and significant advantages in specificity compared to RT-qPCR.

To evaluate the immediate applicability to a broad range of biological or clinical studies, we tested the assay performance on small groups of different types of samples (plasma, tissue, and cells) with different pathological backgrounds (ovarian cancer, breast cancer, and innate immune response) in a one-to-one comparison with TaqMan RT-qPCR. While hsa-miR-21 quantification from tissue allowed for a clear distinction between healthy and tumor tissue and hsa-miR-132 and has-miR-146a quantification from THP-1 cells provided clear evidence for LPS-stimulated or non-stimulated cells, pathological evaluation of plasma samples appeared more challenging. From the diagnostic point of view, TG-FRET clearly outperformed RT-qPCR with 62% of cancer plasma samples detected above the maximum concentration value of healthy control samples, whereas RT-qPCR only detected 17% above threshold. For most of the samples (independent of the sample type), RT-qPCR detected higher concentrations (approximately 3-fold) than TG-FRET and RT-qPCR determined concentrations with a significantly larger distribution. We attribute these higher and broader values of RT-qPCR to specificity issues (*cf.* **Figure 3.5**), the susceptibility to interferences with sample extraction reagents, and the lower precision of this exponential amplification technique at low target input.

The ability to quantify different miRNAs from various types of clinically relevant samples, to obtain significant pathological information from these measurements, the advantages in simplicity and precision compared to RT-qPCR, and the adaptability of the isothermal and washing-free procedure to life-cell imaging, will make TG-FRET a very useful tool (in combination with other technologies or as stand-alone method) for advancing miRNA-based diagnostics and research. Moreover, amplified TG-FRET has the potential to create significant impact for the translation of miRNA biomarkers into the clinic.

4. Multiplexed miRNA diagnostics using CHA-amplified Tb-to-dye FRET

4.1 Introduction

In the previous chapter, we have shown a precise, sensitive, and specific miRNAs assay based on RCA-amplified Tb-to-dye TG-FRET. The absolute quantification of miRNAs from human clinical samples not only revealed the relevance for breast and ovarian cancer diagnostics, but also demonstrated the broad applicability to different miRNAs and other types of clinical samples. The importance of specific disease signatures that are composed of several different miRNA biomarkers have dramatically increased the demand for the simultaneous measurement of multiple targets in a single sample, so-called multiplexed biosensing [220, 221]. Additionally, more efficient clinical diagnostics and personalized therapies require multiplexing technologies ranging from point-of-care testing to high-throughput screening [222-224]. The large choice of commercially available fluorophores with different photochemical and photophysical properties has become an important source for the development of multiplexed PL detection [225]. The implementation of FRET between two fluorophores into PL detection can combine the benefits of biological recognition and multiplexing for molecular diagnostics [226]. While most PL multiplexing approaches are based on spectral (or color) encoding with different fluorophores, which require distinct detection channels and excitation wavelengths. Taking the extremely long PL lifetime and multiplexing capabilities of LTCs, temporal encoding with one single FRET pair can be efficiently exploited.

In contrast to RCA, another commonly used isothermal amplification strategy, CHA, is enzyme-free and therefore avoids the drawbacks of enzymatic reactions, including particular reaction times and conditions to maintain the enzyme's activity. Our group demonstrated an enzyme-free HCR for temporally multiplexed miRNA quantification in a previous study, but the proposed HCR-TG-FRET approach has not been capable of detecting miRNAs in clinical samples [227]. Thus, the implementation of single FRET-pair

temporal multiplexing into other enzyme-free amplification techniques and the analytical validation of its sensing performance on clinical samples are two challenges, which have the potential to further advance rapid and multiplexed miRNA diagnostics.

This work is to achieve multiplexed miRNA diagnostics based on Tb-to-dye TG-FRET and enzyme-free CHA amplification strategy with simplicity, rapidity, sensitivity, and multiplexing at the same time. By using specifically designed hairpin probes that located a single Tb-to-dye FRET pair at different donor-acceptor distances, the sensitive quantification of miR-21 and miR-20a at picomolar concentrations is realized. The CHA-TG-FRET approach displayed excellent performance in the simultaneous detection of miRNAs from human tissue samples, which was verified by parallel measurement with the standard method RT-qPCR. Being capable of multiplexed quantification of miRNAs from clinical samples, CHA-TG-FRET presents an interesting and complementary sensing approach for rapid miRNA-based clinical diagnostics and biomolecular research.

4.2 Materials and methods

4.2.1 Nucleic acid probes and exogenous targets

All sequences and modifications of nucleic acids are summarized in **Table 4.1**. All oligonucleotides were purchased from Eurogentec and purified with HPLC. Lumi4-Tb-NHS (Tb-NHS) was provided by Lumiphore. Cy5.5-NHS was purchased from Lumiprobe. Tb-DNA and Cy5.5-DNA conjugates were obtained by mixing Tb-NHS or Cy5.5-NHS in concentration excess to amino-functionalized oligonucleotides in 100 mM carbonate buffer at pH 9.0. The mixtures were incubated overnight at 4 °C. The Tb-DNA and Cy5.5-DNA conjugates were purified three times with HEPES buffer (100 mM, pH 7.4) by Zeba Spin Desalting Columns (7 kDa molecular weight cutoff, MWCO). Tb concentrations were determined by absorbance measurements at 340 nm using a molar absorptivity of 26,000 $M^{-1}cm^{-1}$ as provided by the manufacturer. Cy5.5 concentrations were determined by absorbance measurements at 684 nm using a molar absorptivity of 209,000 $M^{-1}cm^{-1}$ as

provided by the manufacturer. DNA was quantified by absorbance measurements at 260 nm using molar absorptivities as provided by the manufacturer (H1 for miR-21: 464,100 $M^{-1}cm^{-1}$; H2 for miR-21: 424,600 $M^{-1}cm^{-1}$; H1 for miR-20a: 478,100 M-1cm-1; H2 for miR-20a: 424,200 $M^{-1}cm^{-1}$). Complete fluorophore-DNA conjugation (~100 %) was verified by linear combination of the respective absorbance values of Tb or Cy5.5 and DNA within the Tb-DNA and Cy5.5-DNA conjugates.

Table 4.1 Sequences and modifications of all RNA targets and hairpin DNA probes. Nucleotides with amino-modification for Cy5.5 conjugation are displayed in bold/underlined. Probe-specific domains (*cf.* **Figure 4.1**) are presented in color as follows: 1/1*: red; 2/2*: blue; 3/3*: green; 4/4*: magenta.

Probe	Sequence 5'-3'	Modification
miR-21	UAG CUU AUC AGA CUG AUG UUG A	
miR-20a	UAA AGU GCU UAU AGU GCA GGU AG	
miR-20b	CAA AGU GCU CAU AGU GCA GGU AG	
H1 for miR-21 (Cy5.5 acceptor probe)	TCA ACA TCA GTC TGA TAA GCT ACC ATG TG**T** AGA TAG CTT ATC AGA C	d**T**-C6 amino
H2 for miR-21 (Tb donor probe)	AAG CTA TCT ACA CAT GGT AGC TTA TCA GAC CCA TGT GTA GA	5'-C3 amino
H1 for miR-20a (Cy5.5 acceptor probe)	CTA CCT GCA CTA TAA GCA CTT TAC CA**T** GTG TAG ATA AAG TGC TTA TAG	d**T**-C6 amino
H2 for miR-20a (Tb donor probe)	CAC TTT ATC TAC ACA TGG TAA AGT GCT TAT AGC CAT GTG TAG A	5'-C3 amino

4.2.2 Optical spectroscopy

Absorption spectra (Lambda 35 UV/Vis System, PerkinElmer) and emission spectra (Xenius, SAFAS) were recorded in HEPES buffer (100 mM, pH 7.4) and deionized water (purified by Purelab Option-Q equipped with bio-filter, ELGA LabWater) for Tb and Cy5.5 samples, respectively.

4.2.3 TG-FRET miRNA assays

Before use, both H1 and H2 for each target were denatured at 90 °C for 5 min and then cooled down (2 °C/min) to room temperature (25 °C) to form complete hairpin structures. All FRET assays were prepared in TNaK Buffer (40 mM Tris-HCl, 280 mM NaCl, 10 mM KCl, 0.02% BSA, pH 7.5). These buffer conditions were optimized for obtaining high FRET-ratios. Different buffer conditions will result in different assay performance and therefore, assay calibration curves should be performed under the same conditions as the final miRNA quantification assay. The single sensor assays contained 5 nM of H1, 5 nM of H2 and increasing concentrations of target miRNAs (from 10 pM to 400 pM). Again, the H1 and H2 probe concentrations were optimized and different probe concentrations require the acquisition of separate assay calibration curves. All samples were prepared at once and incubated at room temperature for 3 h. From the total reaction volume of 150 µl, 140 µl were measured in black 96-well microtiter plates on the clinical immunofluorescence plate reader KRYPTOR compact plus (Thermo Fisher Scientific) with TG (0.1-0.9 ms after excitation pulse) PL intensity detection using optical bandpass filters (Semrock) with 494 ± 12 nm for the Tb detection channel and 716 ± 24 nm for the Cy5.5 detection channel. The duplexed sensor assays contained two different H1 (5 nM H1 for miR-21 and 5 nM H1 for miR-20a) and two different H2 (5 nM H2 for miR-21 and 5 nM H2 for miR-20a). 140 µl were measured in black 96-well microtiter plates on a time-resolved fluorescence plate reader (Edinburgh Instruments) using 4000 detection bins of 2 µs integration time, nitrogen laser (MNL 100, LTB) excitation (337.1 nm, 20 Hz), and optical bandpass filters (Semrock) with 494 ± 12 nm for the Tb detection channel and 716 ± 24 nm for the Cy5.5 detection channel. For ratiometric analysis, FRET-ratios were calculated by the ratio of Cy5.5 and Tb TG PL intensities.

4.2.4 Mathematical treatment of multiplexed signal deconvolution

TG PL intensities (I^{TG}) of the Cy5.5 acceptors and Tb donors were determined in their specific time windows (from the corresponding PL decay curves). These TG PL intensities

were then used to calculate a background-subtracted FRET-ratios for each target concentration $c = x$ (**Equation 4.1**):

$$\Delta FRET\text{-}ratio = \frac{I_{Cy5.5}^{TG}(c=x)}{I_{Tb}^{TG}(c=x)} - \frac{I_{Cy5.5}^{TG}(c=0)}{I_{Tb}^{TG}(c=0)} \tag{4.1}$$

The concentration-dependent $\Delta FRET\text{-}ratio$ values were used to determine the calibration curves for each miRNA target in each detection window (*cf.* **Figure 4.4**).

The slopes of the four linearly fitted calibration curves ($z_{miR\text{-}21}^{TG_1}, z_{miR\text{-}20a}^{TG_1}, z_{miR\text{-}21}^{TG_2}, z_{miR\text{-}20a}^{TG_2}$) from **Figure 4.4b** were used to determine the concentrations in the multiplexed assay that led to the concentration recovery in **Figure 4.5** by solving **Equation 4.2** for the concentrations $c(\text{miR-21})$ and $c(\text{miR-21})$. $\Delta FRET\text{-}ratio_1$ and $\Delta FRET\text{-}ratio_2$ were the $\Delta FRET\text{-}ratio$ values from two TG detection windows (TG_1 and TG_2) in the multiplexed assay.

$$\begin{bmatrix} \Delta FRET\text{-}ratio_1 \\ \Delta FRET\text{-}ratio_2 \end{bmatrix} = \begin{bmatrix} c(\text{miR-21}) \\ c(\text{miR-20a}) \end{bmatrix} \times \begin{bmatrix} z_{miR\text{-}21}^{TG_1} & z_{miR\text{-}20a}^{TG_1} \\ z_{miR\text{-}21}^{TG_2} & z_{miR\text{-}20a}^{TG_2} \end{bmatrix} \tag{4.2}$$

4.2.5 RNA extraction

Tissue material was obtained with informed consent at the Medical University of Graz and the St. John of God Hospital Graz under approval from the ethics committee of the Medical University of Graz and the ethics committee of the ST. John of God Hospital Graz. Total RNA was isolated from snap-frozen human colon or rectum tissue samples using Trizol Reagent (Life Technologies), followed by extraction with phenaol-chloroform. Total RNA concentrations and available volumes of all samples are given in **Table 4.2**.

Table 4.2 Total RNA concentrations and sample volumes of clinical tissue samples.

Sample name	**Patient number** (internal database)	**Extracted from**	**Concentration of Total RNA in ng/µl**
A	3	Colon, tumor	1076
B	11	Colon, healthy	576
C	9	Rectum, tumor	575
D	10	Rectum, tumor	386
E	17	Rectum, healthy	103

4.2.6 Absolute quantification of miRNA by TG-FRET

Absolute concentrations of unknown miRNAs were determined by using calibration curves ($\Delta FRET\text{-}ratio$ over concentration) constructed with the use of synthetic (exogenous) miRNAs with known concentrations (between 10 pM and 400 pM within 140 µl solutions). Due to the unknown concentrations of miRNAs in the total RNA tissue extracts, samples were diluted at different dilution factors to make sure that their concentration range fitted the one of the calibration curves. Final dilution factors of the samples were 4-fold (sample A for single target detection), 2-fold (samples B, C, D, and E for single target and samples A and C for duplexed target detection), and 1-fold (samples B, D, and E for duplexed target detection), where x-fold corresponded to a volume fraction of $1/x$ inside the final sample volume of 10 µl. These 10 µl were added to 140 µl of TG-FRET miRNA assays reagents such that the concentrations of the reagents inside the final 150 µl mixtures were the same as for the TG-FRET miRNA assays for exogenous targets (*vide supra*) and the total sample dilution corresponded to $15x$. Thus, the miR-21 and miR-20a concentrations determined by TG-FRET were multiplied by $15x$ to obtain the miRNA concentrations in the total RNA extracts. These miRNA concentrations (in mol/µl) were divided by the total RNA concentrations (in ng/µl – *cf.* **Table 4.2**) and multiplied by the Avogardo constant ($6.022 \times 10^{23} mol^{-1}$) to obtain the miRNA concentration in units "copies of miRNA per ng of total RNA" as presented in **Figure 4.6**.

4.2.7 RT-qPCR miRNA assays

TaqMan MicroRNA Reverse Transcription Kit (Thermo Fisher) in 15 µl containing 5 µl of RNA extract, 0.15 µl of 100 mM dNTPs, 1 µl of Multiscribe reverse Transcriptase (50 U/µl), 1.5 µl of 10× reverse transcription buffer, 0.19 µl of RNase inhibitor (20 U/µl), 3 µl of gene-specific primer, and 4.16 µl of nuclease-free water. For synthesis of cDNA, the reaction mixtures were incubated at 16 °C for 30 min, at 42 °C for 30 min, at 85 °C for 5 min, and then held at 4 °C. Then, 1.33 µl of cDNA solution was amplified using 10 µl of *TaqMan* Universal PCR Master Mix II without UNG (Thermo Fisher), 1 µl of gene-specific primer and probe, and 7.67 µl of nuclease-free water in a final volume of 20 µl. Quantitative

PCR was run on a StepOnePlus (96-well) Real-Time PCR System (Thermo Fisher Scientific), and the reaction mixtures were incubated at 95 °C for 10 min, followed by 40 cycles of 95 °C for 15 s and 60 °C for 1 min. The quantitation cycles (C_q) were calculated with StepOnePlus Systems software (Thermo Fisher Scientific). Absolute concentrations of unknown miRNAs were determined by using a calibration curve (C_q over concentration) constructed with the use of synthetic (exogenous) miRNAs with known concentrations using the same procedure as mentioned above.

4.2.8 Statistical analysis

For statistical analysis and the estimation of LODs, all samples were prepared 3 times and measured in triplicates ($n = 9$). The zero concentration samples (without target miRNAs) were prepared 10 times and measured in triplicates ($n = 30$). Samples of multiplexed assays with varying target concentrations were prepared in duplicate and measured once ($n = 2$). For real sample detections, all samples were prepared in duplicate and measured once ($n = 2$). All RT-qPCR measurements were performed in duplicate and measured once ($n = 2$).

4.2.9 Calculation of FRET parameters

Förster distance (the donor-acceptor distance for which FRET is 50 % efficient) for the Tb-to-Cy5.5 FRET pair ($R_0 = 5.8 \pm 0.2$ nm) was calculated using **Equation 3.1** (*vide supra*). The orientation factor κ^2 was taken as $2/3$ because of random orientation of donor and acceptor during the FRET time (dynamic averaging), which is well justified by the long PL lifetime of the Tb donors and the unpolarized emission (fast isotropic rotation). The refractive index was $n = 1.35$ (aqueous buffer solution). The Tb-centered quantum yield was $\Phi_D = 0.80 \pm 0.05$. The overlap integral J was calculated by **Equation 3.2** (*vide supra*), where $\bar{I_D}(\lambda)$ is the emission intensity from the area-normalized (to unity) emission spectrum of Tb donor and $\varepsilon_A(\lambda)$ is the molar absorptivity of the acceptor.

4.3 Results and discussion

4.3.1 Principle of CHA-TG-FRET miRNA assays

As shown in **Figure 4.1**, two hairpin probes (H1 and H2) for each miRNA target (miR-21 and miR-20a) were carefully designed to efficiently follow the target-mediated CHA process. H1 and H2 can hybridize to form a H1:H2 duplex, since H1 contains a DNA segment that is complementary to a segment of hairpin H2. However, the spontaneous hybridization of the two hairpins is kinetically hindered by occluding complementary regions within the intramolecular hairpin secondary structures. A segment (1*) of the target miRNA serves as a toehold to initiate hybridization with the complementary segment (1) of H1 followed by branch migration, which opens hairpin H1 and forms a miRNA:H1 intermediate. In this intermediate, a segment (3*) of H1 is no longer occluded and can bind to the complementary segment (3) of H2, again initiating a branch migration reaction to form a miRNA:H1:H2 complex. This complex is inherently unstable and target miRNA dissociates from the H1:H2 complex, which completes the reaction and results in a partly double-stranded H1:H2 complex and a recycled target miRNA. Thus, a single miRNA target can act as a catalyst to trigger many cycles of CHA and produce many copies of dsDNA H1:H2 complexes. To quantify miRNA-dependent CHA, the 3' ends of H2 probes (for both target miRNAs) were labeled with a Tb FRET-donor, whereas a Cy5.5 FRET-acceptor was labeled to a specific thymine within H1. Thereby, we obtained distinct donor-acceptor distances (r) for the different target miRNAs. Due to the strong distance dependence of the FRET efficiency ($\sim r^{-6}$), different values of R led to different PL decays of the FRET-quenched donors and FRET-sensitized acceptors (the closer the distance, the faster the decay). The different PL decays were then used for a straightforward temporal multiplexing by TG PL intensity detection. FRET-ratios, which were used for quantifying the miRNA target concentrations (**Figure 4.3** and **Figure 4.4**, **Equation 4.1** and **Equation 4.2**), were measured on two commercially available time-resolved fluorescence plate readers. The ratiometric detection of TG PL intensities of Cy5.5 acceptor and Tb donor allowed for precise and reproducible (low coefficients of variation) CHA-TG-FRET assays.

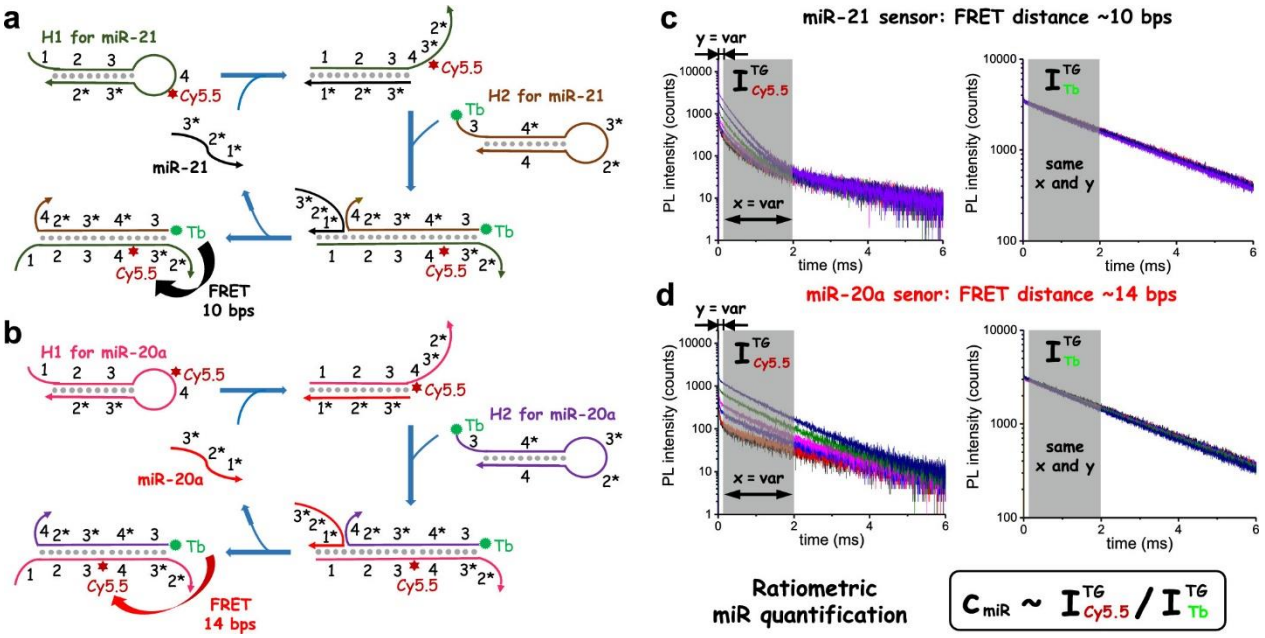

Figure 4.1 Principle of CHA-TG-FRET probes for multiplexed quantification of two miRNAs. Target miR-21 (**a**) and miR-20a (**b**) were mixed with both Cy5.5-acceptor labeled H1 probes and Tb-donor labeled H2 probes. Specific sequences in H1, H2, and target miRNAs, each of which represents a short fragment (usually <12 nt) of DNA or RNA, are presented with numbered domains (1 to 4). Complementarity between these domains is denoted by an asterisk (*e.g.*, 1 and 1*). The miRNA targets serve as a toehold to initiate the opening of hairpin H1, which then opens hairpin H2 to form a dsDNA H1:H2 complex and displace the miRNA target. The released miRNA can then be recycled for another "H1 + H2 → H1:H2" reaction. Signal amplification by CHA was performed at room temperature for 3 h and resulted in the formation of many H1:H2 complexes, in which the Tb-to-Cy5.5 distance was 10 bps for the miR-21-specific complex (**a**) and 14 bps for the miR-20a-specific complex (**b**). Cy5.5 and Tb PL decay curves of increasing concentrations (0 pM to 400 pM from bottom to top) of miR-21 (**c**) and miR-20a (**d**) at constant concentrations (5 nM Cy5.5-acceptor labeled H1 and 5 nM Tb-donor labeled H2) of the miR-21 or miR-20a hairpin probes. The distinct PL decays were used to specifically quantify the different miRNAs. Ratiometric measurements ($\Delta FRET\text{-}ratio$, **Equation 4.1**) of Cy5.5 and Tb TG PL intensities ($I^{TG}(x)$) in variable time windows (width x and delay y) after the excitation pulse were used for quantifying miRNA target concentrations. In the case of duplexed miRNA quantification from a single sample within a single measurement, two different time windows were used (*cf.* **Figure 4.4**) and the two $\Delta FRET\text{-}ratios$ mathematically correlated (**Equation 4.2**).

4.3.2 Single miRNA assay performance

To evaluate the versatility and sensitivity of CHA-TG-FRET, we first tested the single sensor performance for the two prototypical miRNAs miR-21 and miR-20a, which were found to be upregulated in different cancers (miRCancer database reports 248 and 50 cancer-related upregulations for hsa-miR-21 and hsa-miR-20a, respectively) [228, 229]. For both targets, we used a TG detection window with width of $x = 0.8$ ms and a delay of $y = 0.1$ ms after the excitation pulse. Each ratiometric measurement (Cy5.5 and Tb TG PL intensities) on the KRYPTOR immunofluorescence plate reader took only a few seconds. Target selectivity was firstly tested by measuring the FRET-ratios of the miR-20a sensor in the presence of 0 to 400 pM miR-20b, which has only two mismatched nucleotides compared to miR-20a (*cf.* **Table 4.1**). No significant increase of the FRET-ratio was found over the entire concentration range of miR-20b (**Figure 4.2**), which showed the excellent specificity of the CHA-TG-FRET probe for its related target.

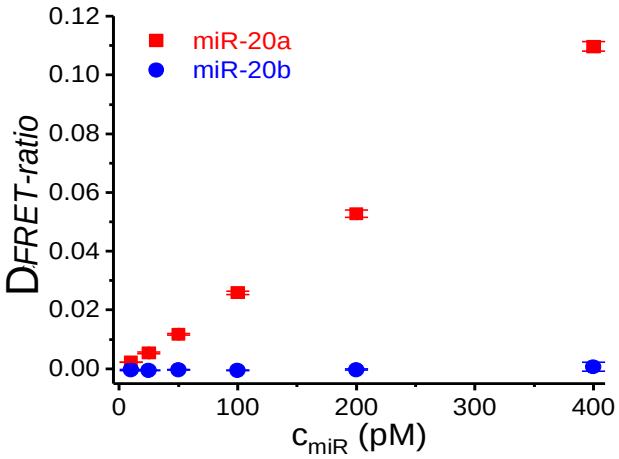

Figure 4.2 Specificity of the CHA-TG-FRET assay for miR-20a was tested against the same concentrations of the 2-nt mismatched miR-20b (compared to miR-20a). Only miR-20a resulted in a sensor response, whereas miR-20b did not lead to an increase of the FRET-ratio over the entire concentration range.

Then the sensitivity of the sensor was evaluated. For both miRNA targets, the calibration curves (**Figure 4.3A**) showed increasing FRET-ratios with increasing miRNA concentrations in a linear dynamic concentration range between 0 and 400 pM. LODs were determined (three standard deviations over the blank sample) as 380 ± 40 attomoles (2.7 ± 0.3 pM in the 140 µl detection volume) of miR-21 and 250 ± 60 attomoles (1.8 ± 0.4 pM in the 140 µl detection volume) of miR-20a (**Figure 4.3B**).

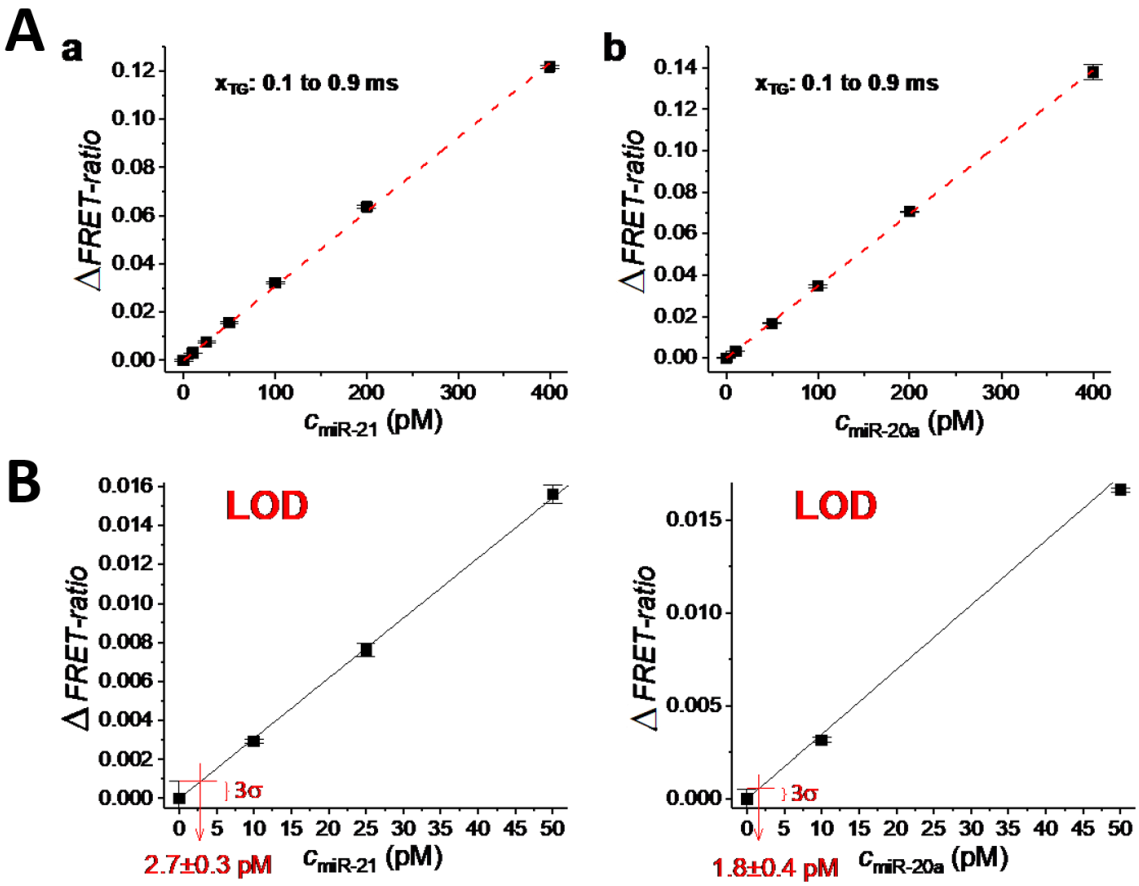

Figure 4.3 (A) CHA-TG-FRET miRNA assay calibration curves for miR-21 (**a**) and miR-20a (**b**). $\Delta FRET\text{-}ratios$ were calculated in TG PL detection windows from 0.1 to 0.9 ms. Error bars depict standard deviations from 9 measurement for $c > 0$ and from 30 measurement for $c = 0$. (B) Determination of LODs by plotting the calibration curves and linear fits (graph A) in the low concentration range. $\Delta FRET\text{-}ratio$ values three standard deviations (3σ, as calculated from 30 measurement of $\Delta FRET\text{-}ratio$ at $c = 0$, *i.e.* the blank sample) above the $\Delta FRET\text{-}ratio$ of the blank were correlated with the linear calibration curve to determine the LOD concentrations (red).

4.3.3 Single FRET-pair multiplexing

The different labeling positions of Cy5.5 in H1 for miR-21 and H1 for miR-20a resulted in different FRET distances (and concomitant FRET efficiencies) between Tb and Cy5.5 in the double-stranded H1:H2 complexes after CHA amplification (**Figure 4.1a** and **Figure 4.1b**). Therefore, the two miRNA sensors provided two distinct FRET-sensitized Cy5.5 PL decay curves (left graphs in **Figure 4.1c** and **Figure 4.1d**). The FRET-quenched Tb PL decay curves (right graphs in **Figure 4.1c** and **Figure 4.1d**) were also different, which is less visible due to the relatively strong background of unquenched Tb-probes (those that did not participate in FRET). When assuming a distance of ~0.33 nm between two base pairs of dsDNA in solution [230], the Tb-Cy5.5 distances would correspond to ~3.3 nm (10 bps) for the miR-21 FRET-probe and ~4.6 nm (14 bps) for the miR-20a FRET-probe. Fitting the PL decay curves from **Figure 4.1** for the actual FRET contributions resulted in slightly longer distances of 4.2 ± 0.2 nm (**Table 4.3**) and 5.1 ± 0.2 nm (**Table 4.4**). These longer distances are reasonable when taking into account the linkers (C6 for Cy5.5 and C3 for Tb – *cf.* **Table 4.1**) between the fluorophores and the DNA labeling position as well as the additional linker in Tb [167]. It also shows that an actual measurement (using the FRET pair as molecular ruler) is better than a simple estimation based on the number of base pairs. While the actual distances were of minor importance for the miRNA sensors, the differences in amplitude averaged PL decay times (~400 µs for the miR-21 FRET-probe and ~900 µs for the miR-20a FRET-probe, *cf.* **Table 4.3** and **Table 4.4**) and concomitant distinct PL decays were significantly more important to realize a multiplexed miRNA detection with a single FRET pair (*vide infra*). Adjusting the donor-acceptor distance by the different number of base pairs between Tb and Cy5.5 and a direct distance-analysis by Tb-to-Cy5.5 FRET are straightforward design and characterization tools for the development of single FRET-pair multiplexed detection of miRNAs.

Table 4.3 Fit results of PL decay curves (**Figure 4.1c**) for the donor-acceptor distances in the miR-21 FRET-probe. Fitting method is described in reference [217].

Tb Donor Channel

#	miR-21 (nM)	τ_D (µs)	A_D	τ_{DA} (µs)	A_{DA}
1	0	2800	3019	-	-
2	2	2800	2936	430	122
3	4	2800	2851	310	215
4	8	2800	2653	370	316
5	10	2800	2547	410	367
		average 2-5		380	E_{FRET}
R_0 = 5.8 nm		distance r (nm)		4.3	0.86

Cy5.5 Acceptor Channel

#	miR-21 (nM)	τ_D (µs)	A_D	τ_{AD1} (µs)	A_{AD1}	τ_{AD2} (µs)	A_{AD2}	$\langle\tau_{AD2}\rangle$ (µs)	E_{FRET}
1	2	2800	60	170	707	400	1420	363	0.87
2	4	2800	60	190	1172	410	2277	371	0.87
3	8	2800	59	230	1591	410	3525	376	0.87
4	10	2800	57	190	1504	400	4494	373	0.87
						average 1-4		371	E_{FRET}
R_0 = 5.8 nm						distance r (nm)		4.2	0.87

Table 4.4 Fit results of PL decay curves (**Figure 4.1d**) for the donor-acceptor distances in the miR-20a FRET-probe. Fitting method is described in reference [217].

Tb Donor Channel

#	miR-20a (nM)	τ_D (µs)	A_D	τ_{DA} (µs)	A_{DA}
1	0	2800	3376	-	-
2	2	2800	3496	990	255
3	4	2800	3145	1000	543
4	8	2800	2605	970	930
5	10	2800	2350	970	1060
		average 2-5		980	E_{FRET}
R_0 = 5.8 nm		distance r (nm)		5.2	0.65

Cy5.5 Acceptor Channel

#	miR-20a (nM)	τ_D (µs)	A_D	τ_{AD1} (µs)	A_{AD1}	τ_{AD2} (µs)	A_{AD2}	$\langle\tau_{AD2}\rangle$ (µs)	E_{FRET}
1	2	2800	79	140	697	910	970	854	0.70
2	4	2800	84	150	751	910	1953	877	0.69
3	8	2800	92	190	587	900	3371	881	0.69
4	10	2800	90	160	618	910	3927	895	0.68
						average 1-4		877	E_{FRET}
R_0 = 5.8 nm						distance r (nm)		5.1	0.69

4.3.4 Duplexed detection of miR-21 and miR-20a

Following the single FRET-pair temporal multiplexing concept mentioned above, we optimized the assay for the simultaneous quantification of miR-21 and miR-20a from a single sample. **Figure 4.4a** shows the target-concentration-dependent PL decays of the duplexed assay in the presence of miR-21 (left), miR-20a (center), and both miR-21 and miR-20a (right)). As expected, the PL decays of the dual-target samples presented a convolution of the shorter and longer PL decays of the miR-21 and miR-20a sensors, respectively. To accomplish simple deconvolution of the two contributions, we applied two different TG detection windows (also shown in **Figure 4.4a**). For temporal multiplexing, the number of detection windows should match the number of targets and the temporal delays and widths of the windows should be adapted to the PL decays. In particular, the different targets need to provide distinct concentration-dependent PL intensity increase to the different windows and these intensities should be as high as possible. Therefore, the later windows are usually selected with a longer width. The detection width should not be too long either because the signal-to-background ratio is lower at later times of the PL decay curves. In our case, the first window (TG_1, with width of $x = 0.7$ ms and a delay of $y = 0.1$ ms after the excitation pulse) showed obvious concentration-dependent intensity increases for both miR-21 and miR-20a, whereas the second one (TG_2, with width of $x = 1.0$ ms and a delay of $y = 1.0$ ms) was significantly more specific for miR-20a (low concentration-dependent concentration increase for miR-21). For both TG detection windows, the FRET-ratios increased linearly with increasing target concentrations (**Figure 4.4b**) and the sum of the single FRET-ratios (for each target) corresponded very well to the FRET-ratio of the mixed samples. These two properties confirmed that the two detection windows were well suited for duplexed detection. Using the four slopes of the single target calibration curves (black and red curves in **Figure 4.4b**), the concentrations of each target in the mixed samples can be determined by the $\Delta FRET\text{-}ratio$ values in both TG detection windows (blue data points in **Figure 4.4b**) and **Equation 4.2**, which presents a simple linear equation with a 2×2 matrix of the calibrated slopes.

The advantage of using both sensors and temporal multiplexing is that the two different miRNA targets can be quantified simultaneously from the same sample with a single measurement. Taking into account that there is no single disease-specific miRNA, the quantification of several different miRNA targets (so-called disease-specific miRNA signatures) by a single measurement is faster and requires less reagents and less patient sample volume. Nevertheless, the advantages of single-sample multiplexing are always accompanied by the disadvantage of slightly reduced sensitivity and accuracy. Therefore, it is important to verify if the compromise between rapidity, reduced sample volume, and lower costs on the one and reduced sensitivity and accuracy on the other side is suitable for efficient target quantification. To test the performance of the single FRET-pair dual target CHA-TG-FRET miRNA assay under more challenging duplexing conditions, we prepared 13 samples with varying concentrations of the two miRNA targets. **Figure 4.5** shows the selective, sensitive, and precise recovery of both miR-21 and miR-20a at varying low picomolar concentrations from the 13 different samples with quite high accuracy. For the 14 miRNA concentrations (those data points that were not zero), the accuracies (deviations from the known concentrations) were within 5 % for seven values, 10 to 20 % for five values, and 20 to 30 % for two values. The deviations from the 12 “zero-concentrations” were below 1 pM for five values, between 2 pM and 5 pM for six values, and 7 pM for one value.

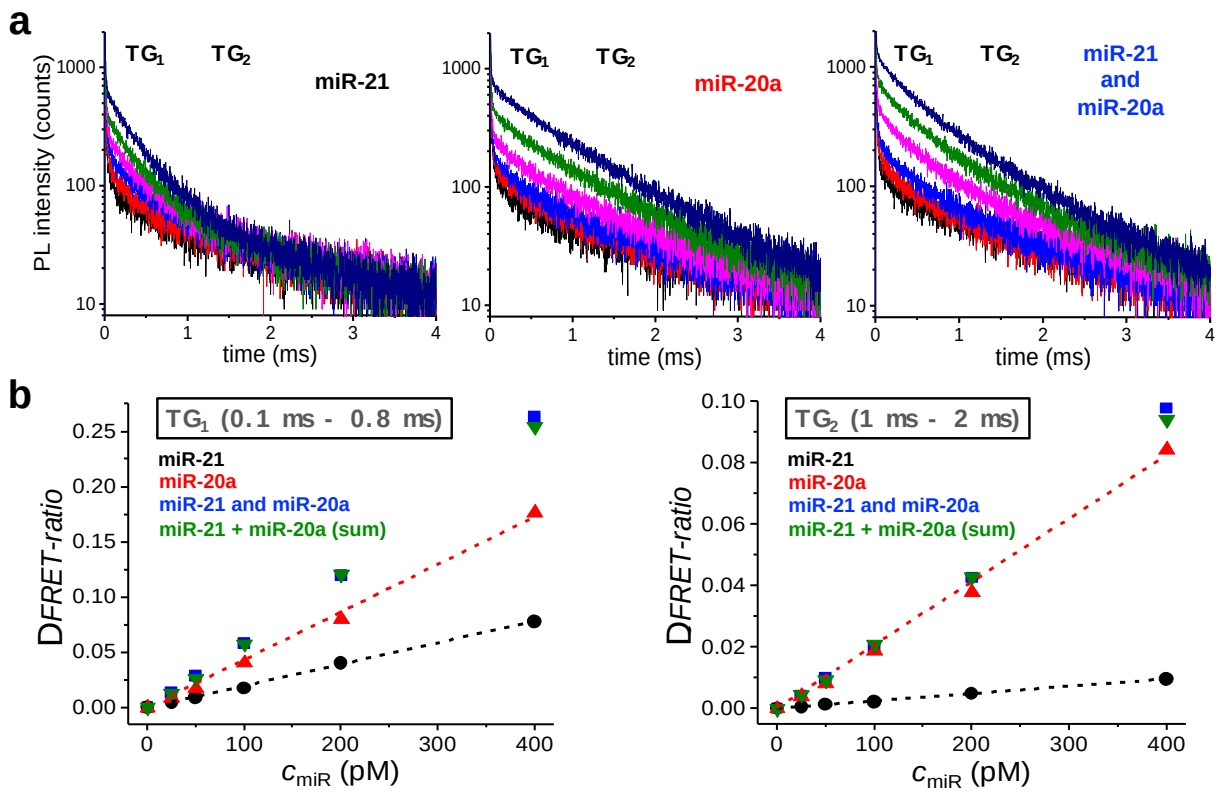

Figure 4.4 (**a**) PL decay curves of the duplexed CHA-TG-FRET miRNA assay measured in the Cy5.5-acceptor detection channels for increasing concentrations (0 pM to 400 pM from bottom to top) of miR-21, miR-20a, and both miR-21 and miR-20a in a single sample. (**b**) Concentration dependent FRET-ratios calculated from the TG PL intensities detected in TG_1 and TG_2 from the PL decay curves in graph **a**. Green data points present the sum of black and red data points for each concentration. The dotted lines present the single-target calibration curves, whose slopes ($z^{TG_1}_{miR\text{-}21} = 1.94\times10^{-4}$ pM^{-1} ; $z^{TG_1}_{miR\text{-}20a} = 4.31\times10^{-4}$ pM^{-1} ; $z^{TG_1}_{miR\text{-}20a} = 4.31\times10^{-4}$ pM^{-1} ; $z^{TG_2}_{miR\text{-}20a} = 2.06\times10^{-4}$ pM^{-1}) were used to calculate target concentrations for CHA-TG-FRET multiplexed assays using the $\Delta FRET\text{-}ratio$ values of the mixed samples (blue data points) and **Equation 4.2**. All assays contained all four hairpin probes (H1 and H2 for miR-21 probes, H1 and H2 for miR-20a – *cf.* **Figure 4.1a** and **Figure 4.1b**) in the same sample.

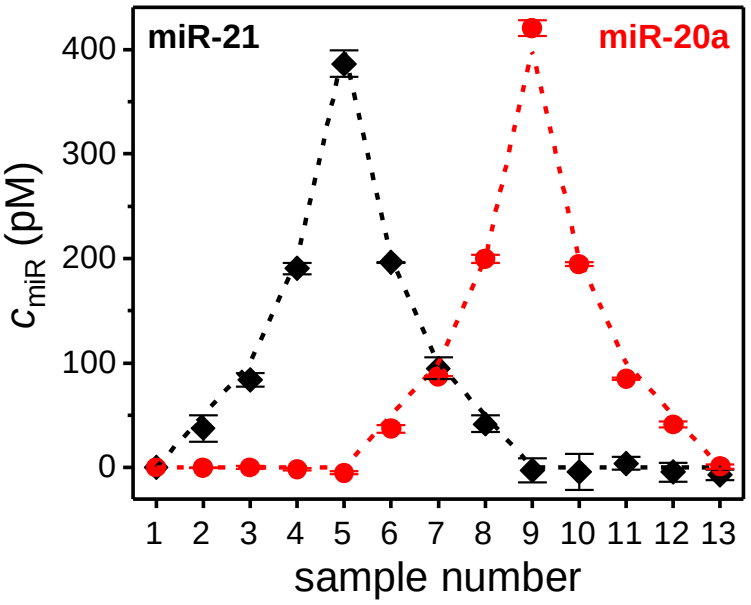

Figure 4.5 Concentration recovery of miR-21 and miR-20a from 13 samples with different concentrations of both targets using the duplexed CHA-TG-FRET miRNA assay. Dotted lines present known concentrations, data point present measured concentrations (error bars represent standard deviations from two measurements per sample).

4.3.5 MiRNA quantification from human tissue samples

To demonstrate the applicability of CHA-TG-FRET to clinically relevant samples, we quantified miR-21 and miR-20a in total RNA extracts from arbitrarily selected human tissue samples (*cf.* **Table 4.2**). Both single and duplexed target CHA-TG-FRET as well as RT-qPCR (for comparison with a standard method) were used to quantify the two miRNAs. **Figure 4.6** shows the concentrations of miR-21 and miR-20a for each sample measured with the three different methods. Single-target, duplexed, and RT-qPCR all detected very similar absolute concentrations of both miRNAs without systematic deviation from one to the other method, which shows that the multiplexed CHA-TG-FRET sensor provided excellent sensitivity and selectivity for miR-21 and miR-20a even in clinical samples. When comparing the single target to the duplexed results, one can find significant differences in samples A and C for miR-21 and in samples D and E for miR-20a. Considering that only one of the miRNA targets showed different concentrations (whereas the other target showed

very similar concentrations for that same sample), we do not believe that these differences were caused by the duplexing approach but rather by the complex total RNA sample with many different RNAs (including miRNAs). None of the methods could provide a clear distinction of the type of tissue (A and B were colon samples; C, D, and E were rectum samples) or if the tissue was from a tumor (A, C, D) or healthy (B, E). However, this proof-of-concept experiment with only few arbitrarily selected samples did not aim at a clinical analysis but rather a demonstration of the capability of CHA-TG-FRET to quantify absolute concentrations of different miRNAs in a multiplexed format in clinical samples. Taking into account that the concentrations of miR-21 were much higher than miR-20a (as expected from the usually well expressed miR-21 in many different types of cancer-related biological samples [228, 229]), most measured concentrations were significantly above the LODs of CHA-TG-FRET, and all concentrations corresponded well to the RT-qPCR values, it can be assumed that the determined concentrations are realistic and multiplexed CHA-TG-FRET may become a useful complementary tool for miRNA-based clinical diagnostics.

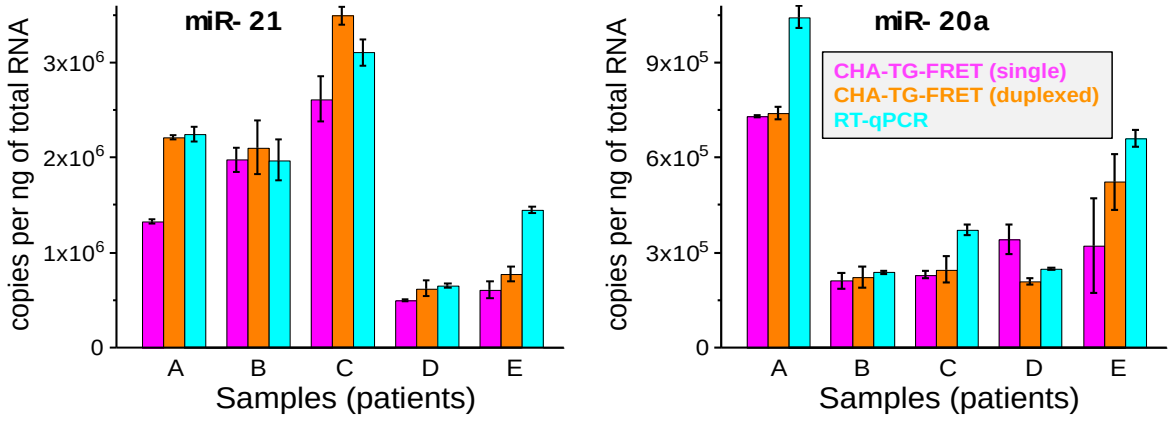

Figure 4.6 Absolute quantification of miR-21 (left) and miR-20a (right) in total RNA extracts from colon (A, B) and rectum (C, D, E) tissues with (A, C, D) and without (B, E) tumors. Single-target CHA-TG-FRET (magenta), duplexed CHA-TG-FRET (orange), and RT-qPCR (cyan) led to very similar concentrations. All concentrations were normalized to the concentrations of total RNA in the tissue extracts. Picomolar concentrations in the experimental volumes (used for measurements) and in the total RNA extracts as well as dilution factors (from samples to measurement volumes) can be found in **Table 4.5**.

Table 4.5 Concentrations of miR-21 and miR-20a in the experimental volumes and in the total RNA extracts and dilution factors used to dilute the total RNA extract samples to measurement volumes. Total RNA concentrations in copies per ng total RNA are the same as in **Figure 4.6**.

CHA-TG-FRET		c(miR-21)			c(miR-20a)		
Sample name	Dilution factor from total RNA extract	150 µL mix (in pM)	Total RNA (in pM)	Total RNA (in copies per ng total RNA)	150 µL mix (in pM)	Total RNA (in pM)	Total RNA (in copies per ng total RNA)
A	60	40	2400	1.3E+06	22	1320	7.4E+05
B	30	63	1890	2.0E+06	6.8	204	2.1E+05
C	30	83	2490	2.6E+06	7.3	219	2.3E+05
D	30	11	330	5.1E+05	7.3	219	3.4E+05
E	30	3.5	105	6.1E+05	1.8	54	3.2E+05

CHA-TG-FRET DUPLEXED		c(miR-21)			c(miR-20a)		
Sample name	Dilution factor from total RNA extract	150 µL mix (in pM)	Total RNA (in pM)	Total RNA (in copies per ng total RNA)	150 µL mix (in pM)	Total RNA (in pM)	Total RNA (in copies per ng total RNA)
A	30	132	3960	2.2E+06	44	1320	7.4E+05
B	15	134	2010	2.1E+06	14	210	2.2E+05
C	30	111	3330	3.5E+06	7.9	237	2.5E+05
D	15	27	405	6.3E+05	9	135	2.1E+05
E	15	8.8	132	7.7E+05	6	90	5.3E+05

RT-qPCR		c(miR-21)			c(miR-20a)		
Sample name	Dilution factor from total RNA extract	5 µL (10ng total RNA) sample (in pM)	Total RNA (in pM)	Total RNA (in copies per ng total RNA)	5 µL (10ng total RNA) sample (in pM)	Total RNA (in pM)	Total RNA (in copies per ng total RNA)
A	538	7.4	4007	2.2E+06	3.5	1865	1.0E+06
B	288	6.5	1885	2.0E+06	0.8	228	2.4E+05
C	287	10.3	2968	3.1E+06	0.9	255	2.7E+05
D	193	2.2	419	6.5E+05	0.8	159	2.5E+05
E	51	4.9	248	1.4E+06	2.2	113	6.6E+05

4.4 Conclusion

The enzyme-free amplification strategy of CHA provides significant advantages for a simple and cost-effective application in sensitive nucleic acid biosensing. Implementing Tb-to-dye TG-FRET probes with their benefits of a rapid, separation-free assay format, absence of sample autofluorescence, and capability of multiplexing, into CHA can further increase the versatility, rapidity, and simplicity of CHA-based miRNA sensing. To demonstrate this promising combination, we developed a single FRET-pair CHA-TG-FRET probe for multiplexed miRNA detection. Tb donors were labeled to the 3' ends of the CHA hairpin probes, whereas Cy5.5 acceptors were labeled to specific thymines inside the probes, which allowed us to tune the Tb-donor to Cy5.5-acceptor distance. Two FRET probes for miR-21 and miR-20a were designed with specific donor-acceptor distances that

resulted in target-specific PL decays of the Cy5.5 FRET acceptors. The different decays allowed us to use two different TG detection windows for a simple PL intensity measurement that could specifically quantify the two different miRNA targets from a single sample with a single measurement and a single FRET pair. The ratiometric CHA-TG-FRET assays provided high precision, accuracy, reproducibility, and specificity (tested against a miRNA target with two mismatched nucleotides), low limits of detection (380 ± 40 attomoles for miR-21 and 250 ± 60 attomoles for miR-20a), and the simultaneous quantification of both miRNAs at different picomolar concentrations from the same sample. The potential application for clinical studies was demonstrated by quantifying miR-21 and miR-20a from total RNA extracts of five different human tissue samples (colon and rectum samples with and without tumors) by single-, duplexed-CHA-TG-FRET and RT-qPCR for comparison. In comparison to the RT-qPCR, CHA-TG-FRET amplifies signal by recycling the target, making it much less susceptible to sample cross contamination. CHA-TG-FRET is also much simpler than RT-qPCR because it requires neither reverse transcription of the target nor enzymes for amplification. The amplification is isothermal (no thermal cycling required) and linear (exponential amplification leads to larger errors due to contamination and non-specific amplification) and multiplexing can be performed in a single sample, with a single measurement, and a single excitation wavelength. The simple sample preparation and rapid ratiometric measurement are also advantageous concerning reliability and accuracy of the results, which are more complicated for RT-qPCR., PCR can provide much lower detection limits (down to single copies of nucleic acids) than CHA-TG-FRET, which is certainly advantageous for samples with extremely low target concentrations.

While this proof-of-concept used two different miRNAs as targets for clinical diagnostics in tissues, it can be extended to other clinical samples, different miRNA targets, different nucleic acid biomarkers, and higher order multiplexing by using more colors and more FRET-distances. Together with complementary established and emerging technologies, CHA-TG-FRET can become a useful method for nucleic acid analysis and quantification in human samples for biomolecular research and clinical diagnostics.

5. MiRNA nano-diagnostics using HRCA-amplified Tb-to-QD FRET

5.1 Introduction

In the previous chapters, we have shown two sensitive and specific miRNA detection methods that combine isothermal amplification with Tb-to-Cy5.5 FRET. The utilization of Tb complexes and dyes as FRET pairs has the benefit of both small donors and acceptors, which allows for facile conjugation of nucleic acids (FRET probes) and more precise donor-acceptor distance tuning. Compared to dyes, QDs have superior photophysical properties that can be effective energy acceptors. Their large absorption cross-sections result in very large spectral overlap integrals and hence long Förster distances, allowing for significantly longer FRET distances. Moreover, in color-multiplexing approach, the disadvantage of organic dyes for FRET applications is their spectral crosstalk, which predominantly results from the dye emissions of shorter wavelengths into the bandpass filters of longer wavelength dyes due to the significant overlap between the different dye emission spectra and needs to render tedious correction of measured signals. On the contrary, narrow and symmetric emission spectra of QDs favor their multiplexed detection without spectral crosstalk, and their size tunability enables using several different-sized QD acceptors for the same donor. In the previous work in our group [200], spectral multiplexed miRNA diagnostic has been realized by using Tb-to-QD-based FRET. Only 30 min of sample incubation and 7.5 s of measurement were required to selectively quantify three different miRNAs. As no amplification technology was used, the main drawback of this sensor is the relatively low sensitivity. However, the implement of amplification technology with QD-based FRET sensor is not as straightforward as with dye-based FRET sensor, and only a few studies on amplified QD-based FRET sensor for miRNA detection assay have been reported.

To date, hyperbranched rolling circle amplification (HRCA) has been widely used for biosensing various targets, including miRNAs [194, 231], DNAs [232, 233], mutations [234, 235], proteins [236, 237] and small molecules [238, 239]. By introducing a second primer complementary to the RCA products, the linear RCA can be converted to HRCA, which significantly improves the amplification efficiency (~10^9-fold). Most importantly, it can generate numerous varying length DNA segments because the HRCA products are different from the RCA product (which are long and coiled DNA concatemers) [240]. Thus, QDs with relatively large size can be easier implemented into HRCA product for generating FRET signal. Few studies [194, 231] demonstrated the integration of HRCA with QD-to-dyes FRET for miRNAs detection and even realized the simultaneous detection of multiple miRNAs. However, steady-state measurements contain sample autofluorescence and the emission from multiple probes cannot be suppressed.

This work integrated TG measurement into HRCA for sensitive miRNA detection, which provides extremely low background noise, and a quick and simple one-step assay format. Hsa-miR-21 was selected as target. Target-primed and reverse primer-initiated HRCA reaction can generate a large amount of single strand DNAs with different lengths. They can be hybridized with Tb-labeled reporter DNA probes, and then hybridized with the adaptor DNA probes that are on the surface of the QD *via* biotin and streptavidin interaction. The formation of QD-DNA-Tb complexes shorten the distance between Tb and QD, allowing for Tb-to-QD FRET. The FRET-sensitized QD PL and FRET-quenched Tb PL within a specific time-window is measured and ratiometric TG-FRET signal is used to quantify target miRNA. The low LOD (down to attomole) and high selectivity demonstrated the unprecedented performance of this HRCA-amplified Tb-to-QD FRET assay.

5.2 Materials and methods

5.2.1 Materials

Lumi4-Tb-NHS (Tb-NHS) was provided by Lumiphore Inc. Qdot705 ITK Streptavidin Conjugate Kit was purchased at Invitrogen by Life Technologies. Sequences and modifications of all DNA and RNA oligonucleotides are summarized in **Table 5.1**. All oligonucleotides were purchased from Eurogentec and purified with HPLC. Zeba Spin Desalting Columns (7 kDa MWCO) were purchased from Thermo Fisher Scientific. SplintR ligase, phi29 DNA polymerase, dNTP and nuclease-free water were purchased from New England Biolabs. Deionized water was purified by Purelab Option-Q equipped with bio-filter, ELGA LabWater.

Table 5.1 Sequences and modifications of all DNA and RNA probes and targets. Target-specific termini of padlock DNA shown in blue, reverse primer-specific sequences shown in underline, Tb-probe-complementary sequences shown in green, and QD-probe-complementary sequences shown in red.

Probe	Sequence 5'-3'	Modification
miR-21	UAG CUU AUC AGA CUG AUG UUG A	
miR-20b	CAA AGU GCU CAU AGU GCA GGU AG	
padlock-21	TGA TAA GCT A GAA AG ACG GAC TCG CAT TCA CTG TCT AAC AAT ATT GTC TTG ATT GAA GAC AGA CGA CAG AAC AG TCT TCA ACA TCA GTC	5'-Phosphate
reverse primer	GAC AGA CGA CAG AAC AG	
reporter probe (Tb-probe)	AAT CAA GAC AAT ATT GTT	3' C6 amino
adapter probe (QD-probe)	CAG TGA ATG CGA GTC CGT CT	5' TEG biotin

5.2.2 Optical spectroscopy

Absorption spectra (Lambda 35 UV/Vis System, PerkinElmer) and emission spectra (SAFAS) for Tb and QD samples were recorded in HEPES buffer (100 mM, pH 7.4) and hybridization buffer, respectively. All spectra are shown in **Figure 5.1**.

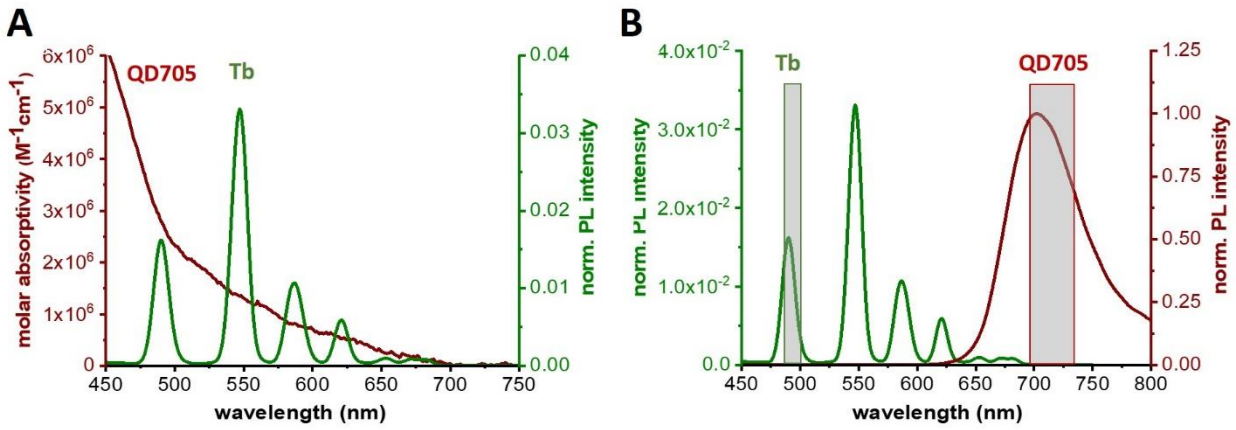

Figure 5.1 Absorption and emission spectra of the TG-FRET pair. (A) Spectra of Tb emission (green) that partly overlaps with the absorption of QD705 (red). (B) Emission spectra of Tb (green) and QD705 (red). Optical bandpass filter transmission spectra, which represent the detection channels for Tb and QD705, are shown in gray.

5.2.3 HRCA-amplified Tb-to-QD TG-FRET miRNA assays

In a typical assay, 5 nM padlock probe and an appropriate amount of the target miRNA were prepared in 10 µl optimized SplintR ligase reaction buffer (BUFFER-1, 50 mM Tris-HCl, 10 mM $MgCl_2$, 100 mM NaCl, 10 µM ATP, 1 mM DTT, pH 7.5), and the mixture was incubated in a thermal cycler with a temperature control program (80 ℃ for 2 min, then decreased from 80 ℃ to 22 ℃ with a 2 ℃ min^{-1} speed). Then, 21.5 U of SplintR ligase prepared in 5 µl BUFFER-1 was added and incubated at 37 ℃ for 1 h. Afterwards, 35 µl phi29 DNA polymerase reaction buffer (BUFFER-2, 1× buffer components: 50 mM Tris-Cl, 10 mM $MgCl_2$, 10 mM $(NH_4)_2SO_4$, 4 mM DTT, pH 7.5), which contained 5 µM reverse primer, 5 U of phi29 DNA polymerase and 0.2 mM dNTP, was added and incubated at 37 ℃ for 2 h. After polymerization and reverse transcription process, 20 nM reporter probe (Tb-DNA conjugate) prepared in 50 µl hybridization buffer (BUFFER-3, 20 mM

Tris-Cl, 500 mM NaCl, 0.1% BSA, pH 8.0) was added and then incubated in a thermal cycler with a temperature control program (80 ℃ for 2 min, then 65 ℃ for 10 min, then decreased from 65 ℃ to 22 ℃ with a 2 ℃ min^{-1} speed). Upon termination of hybridization between reporter probe and HRCA product, 50 µl 10 nM adapter probe (QD-sAv-Biot-DNA conjugate, which was prepared in advance by mixing 0.5 nM streptavidin-conjugated ITK Qdot705 with 10 nM biotinylated DNA in BUFFER-3 at room temperature for 30 min) was added and incubated at room temperature for 30 min. From 150 µl total reaction volume, 140 µl were measured in black 96-well microtiter plates on KRYPTOR compact plus (Thermo Fisher Scientific) with time-gated (0.1 to 0.9 ms) PL intensity detection using optical bandpass filters (Semrock) with 494 ± 12 nm for the Tb detection channel and 716 ± 20 nm for the QD705 detection channel. For ratiometric analysis, FRET-ratios were calculated by the ratio of QD705 and Tb time-gated PL intensities.

5.2.4 Statistical analysis

For statistical analysis and the estimation of LODs, all samples were prepared 3 times and measured in triplicates ($n = 9$). The zero concentration samples (without target miRNAs) were prepared 5 times and measured in triplicates ($n = 15$).

5.2.5 Gel Electrophoresis

8% polyacrylamide gel was prepared (7.9 ml deionized water, 4 ml 30% acrylamide, 3 ml pH 8.0 5× TBE buffer, 0.11 ml 10% ammonium peroxodisulfate and 20 µl TEMED). 10 µl portion of each sample was loaded into the lane, and electrophoresis was performed on a Mini-PROTEAN Tetra electrophoresis system (Bio-Rad) at a constant potential of 200 V for 20 min with 0.5× TBE (pH 8.0) as running buffer. SYBR green I (Thermo Fisher) was used as DNA stain. The gel was visualized under UV light.

5.3 Results and discussion

5.3.1 Principle of HRCA-amplified TG-FRET

The principle of miRNA detection by HRCA-amplified TG-FRET is shown in **Figure 5.2**. We designed padlock-DNA template using miR-21 as target and one reverse primer for HRCA (**Table 5.1**). First, target miR-21 is specifically hybridized by the two ends of the linear padlock-DNA that circularizes upon target recognition. Then, the padlock nick is ligated over the target splint, which makes the target a primer for a polymerase to synthesize complementary DNA around the circular probe DNA, producing a long DNA strand with repeated sequences (rolling circle product). Meanwhile, the reverse primer may specifically bind to the complementary region of the RCA product to initiate the HRCA reaction. It produces large amounts of single-stranded DNAs with various lengths, which can hybridize with Tb-labeled reporter probes (donor DNA probes) and QD705-sAv-Biot-DNA adapter probes (acceptor DNA probes). The close distance of Tb and QD705 allows for Tb-to-QD705 FRET, which is not possible if both are free in solution (no hybridized to HRCA product). Ratiometric TG-FRET signal is used to quantify target miRNA, which measures the ratio of FRET-sensitized QD705 PL and FRET-quenched Tb PL within a specific time-window after pulsed excitation (to suppress autofluorescence).

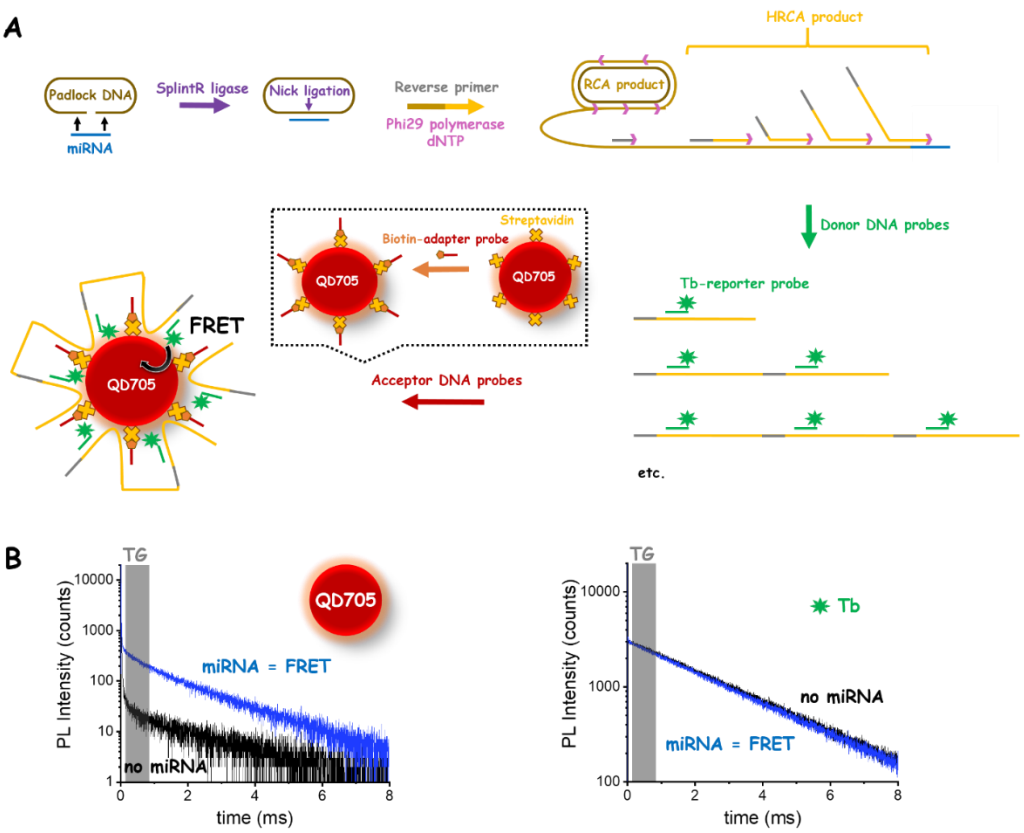

Figure 5.2 The principle of miRNA detection by HRCA-amplified TG-FRET. (A) After specific recognition of miRNA by a linear padlock-DNA, the padlock-DNA nick is ligated over the miRNA target splint using SplintR ligase, and the miRNA becomes a primer for a phi29 polymerase to synthesize and displace complimentary DNA around the circularized padlock-DNA, producing a long DNA strand (RCA product). The reverse primers specifically bind to the complementary region of the RCA product to initiate the HRCA reaction, producing large amounts of single-stranded DNAs with various lengths (HRCA products). The HRCA products are incubated with Tb donor (reporter ssDNA probes labeled with Tb) and QD705 acceptor DNA probes (adapter ssDNA probes conjugated to QD705 via streptavidin-biotin interaction), and the close distance of Tb and QD705 allows for Tb-to-QD705 FRET. Thus, the TG-FRET signal can be used for quantifying miRNA without any washing or separation steps. (B) Ratiometric TG-FRET, which measures the ratio of FRET-sensitized QD705 PL and FRET-quenched Tb PL within a specific time-window after pulsed excitation (to suppress autofluorescence), is used to quantify the miRNA target in a 140 µl microwell. Black/blue decay curves present signals without/with target miRNA. The FRET-sensitized QD-acceptor intensity strongly increases with the presence of target, whereas

the overall Tb-donor signal is not significantly quenched (also free Tb DNA probes in solution emit PL).

5.3.2 Feasibility of HRCA-amplified TG-FRET

To verify the products of the HRCA products, we performed gel electrophoresis (**Figure 5.3**). The gel showed two main bands, one for the padlock-DNA and another for the HRCA products. Lane 1 only contained the padlock-DNA without any HRCA steps as control. Lane 2 contained the padlock and reverse primer, and HRCA steps were performed as the description **in Section 5.2.3** in the absence of miR-21. Notably, for the same padlock-DNA, the molecular weight in lane 1 (weak band around 100 bp, DNA ladder marker as control in lane M) was different than in lane 2 (weak band around 75 bp). This difference was caused by the differences in padlock conformation. Lane 1 contains only the padlock and self-hybridization within the padlock sequence can make the DNA slightly more coiled or and/or less charged such that it migrates less in the gel. In lane 2, the RCA step heated and then slowly cooled down the padlock, such that the padlock conformation was opened to better hybridize to the target. This "actual" ssDNA conformation of the padlock should therefore be closer to its actual sequence length. In the presence of padlock and miR-21 but absence of reverse primer (lane 3), a strong band with high molecular weight appeared, which presents the long ssDNA RCA product. When padlock, miR-21, and the reverse primer were present (lane 4), a broad band with different molecular weights became visible, indicating the miRNA-specific formation of HRCA ssDNA products of different lengths.

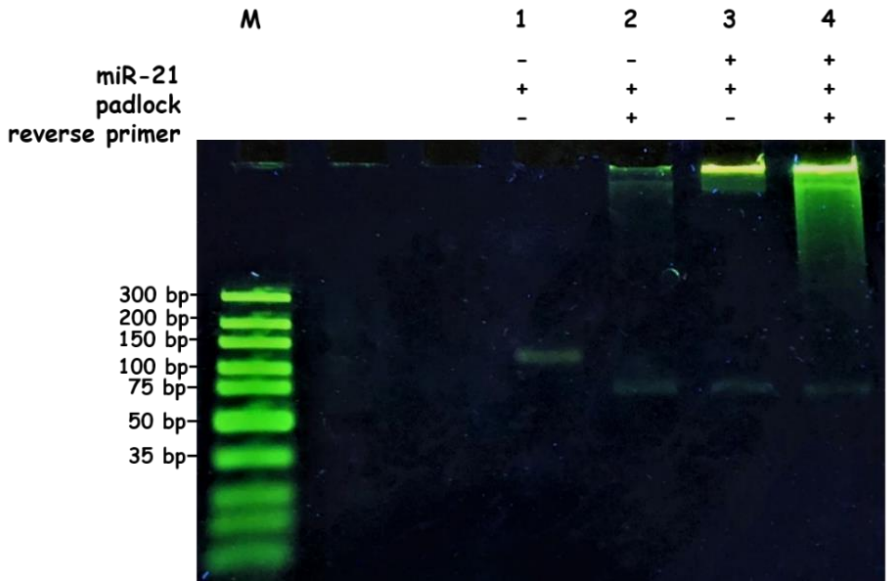

Figure 5.3 Electrophoresis gel for DNA ladder marker (lane M), padlock (lane 1), HRCA product in the absence (lane 2) and presence (lane 4) of target miR-21, HRCA product in the absence of reverse primer (lane 3).

We further measured the time-resolved PL decay curves of FRET-sensitized QD705 and FRET-quenched Tb (**Figure 5.4A**) with different target miR-21 concentrations (between 0 pM and 500 pM). With increasing miR-21 concentrations, the intensities of FRET-sensitized QD705 significantly increased and the intensities of FRET-quenched Tb slightly decreased, which confirms the target concentration-dependent HRCA production and the possibility for miRNA quantification. **Figure 5.4B** shows the calibration curve of miR-21 over a larger concentration range which spanned around 2 orders of magnitude (from 3 pM to 500 pM) to assess the dynamic range of HRCA-amplified TG-FRET assays. The ratiometric PL intensity (FRET-ratio) increases as a function of miR-21 concentration in that concentration range and shows a linear correlation with the miR-21 concentration in the range from 0 pM to ~10 pM. In **Chapter 3**, we presented a RCA-amplified TG-FRET technology for absolute quantification of miRNAs (miR-21, miR-132 and miR-146a). Compared to the quadratic calibration curve, the linear calibration curve (in the lower concentration range) of this study provides the capability of multiplexed miRNA detection from a single sample.

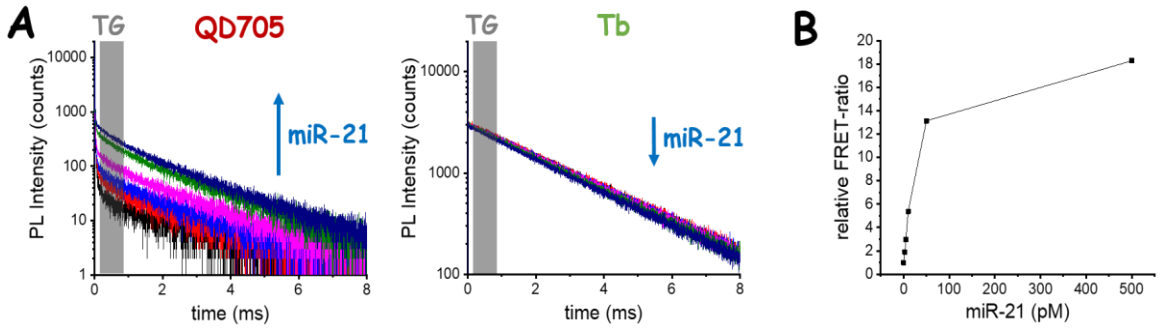

Figure 5.4 (A) Time-resolved PL decay curves of FRET-sensitized QD705 and FRET-quenched Tb, and (B) calibration curve of miR-21 over a lager concentration range from 0 pM to 500 pM within 140 µl solutions per microwell.

5.3.3 Optimization of HRCA-amplified TG-FRET

We optimized the experimental conditions including the concentrations of padlock and reverse primer, HRCA reaction time, and concentration ratio of adapter probes per QD705. As shown in **Figure 5.5A**, the relative FRET-ratio improved with increasing concentration of padlock from 0.1 to 5 nM, whereas it decreased at the concentration of 50 nM. A high concentration of padlock can lead to high HRCA efficiency, but the excess padlock may hybridize with RCA products, adapter probes and reporter probes. This might increase the HRCA background signal and prevent the formation of Tb-DNA-QD705 complexes that are the prerequisite for FRET. In contrast, a low concentration of padlock can decrease the background, but it might induce low amplification efficiency due to the lack of padlock templates. Thus, 5 nM was selected as the optimum concentration of padlock for HRCA reaction. For the concentration of reverse primers, the FRET-ratio significantly increased at a concentration of 5 µM, followed by a decrease at higher concentration (**Figure 5.5B**), which was most probably caused by primer dimerization and nonspecific amplification. Thus, 5 µM reverse primer was selected as the optimum concentration for subsequent experiments. Then we optimized the HRCA reaction time, and the results showed that the relative FRET-ratio value increased with increasing reaction time (**Figure 5.5C**). As a compromise between high but not too long amplification, we selected 2h as the HRCA

reaction time for subsequent experiments. As shown in **Figure 5.5D**, the relative FRET-ratio increased when the concentration ratio between adapter probe and QD705 increased from 1:1 to 20:1, but it tended to saturate beyond the ratio of 20:1 and even decrease for 60:1. Thus, 20:1 (10 nM : 0.5 nM) was used as the optimum concentration ratio between adapter probe and QD705.

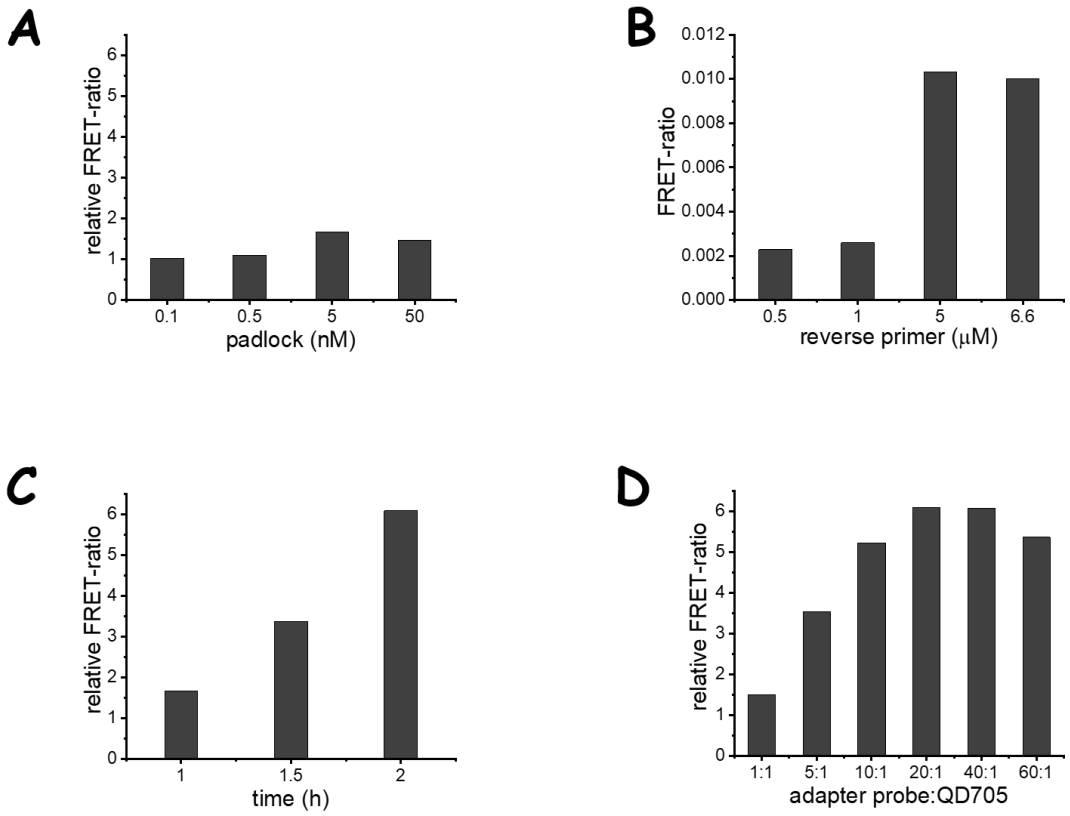

Figure 5.5 Optimization for padlock concentration (A), reverse primer concentration (B), HRCA reaction time (C) and concentration ratio between adapter probe and QD705 (adapter probe:QD705) (D) in the presence of 50 pM miR-21.

5.3.4 Sensitivity and specificity

Under the optimized experimental conditions, I further investigated the sensitivity of the proposed method for miR-21 quantification. To quantify miRNA, TG PL intensities (I^{TG}) of the QD705 acceptor and Tb donor were determined in a specific time window (from the corresponding PL decay curves between 0.1 and 0.9 ms). These TG PL intensities were then used to calculate a $\Delta FRET\text{-}ratio$ (the FRET-ratio subtracted by the FRET-ratio without target) for each target concentration $c = x$ (**Equation 5.1**):

$$\Delta FRET\text{-}ratio = \frac{I_{QD705}^{TG}(c=x)}{I_{Tb}^{TG}(c=x)} - \frac{I_{QD705}^{TG}(c=0)}{I_{Tb}^{TG}(c=0)} \quad (5.1)$$

The concentration-dependent $\Delta FRET\text{-}ratio$ values were used to determine the calibration curves for the miRNA target. The calibration curve (**Figure 5.6A**) showed increasing $\Delta FRET\text{-}ratio$ values with increasing miR-21 concentrations in a concentration range between 0 pM and 15 pM. The LOD was estimated (three standard deviations over the blank sample calculated from n = x measurements) to be 11 ± 4 attomole (80 ± 30 fM).

The target specificity of HRCA-amplified TG-FRET was evaluated against miR-20b (**Figure 5.6B**). Concentration-dependent increasing $\Delta FRET\text{-}ratio$ values exclusively occured for target miR-21. Taking into account our previous study on specificity of RCA-amplified TG-FRET miRNAs detection in **Chapter 3**, it showed excellent specificity against precursor miRNA (pre-miRNA) and miRNAs with single nucleotide variations. The versatility of the padlock design can overcome the mismatch-caused positive offset. Besides, the 3' to 5' exonucleolytic activity and highly accurate replication of phi29 DNA polymerase can also correct errors caused by incorporation of mismatched deoxyribonucleotides as well as pre-miRNAs which have two 3' and 5' overhangs. Overall, HRCA-amplified TG-FRET quantification of miRNA provided excellent performance concerning sensitivity and specificity.

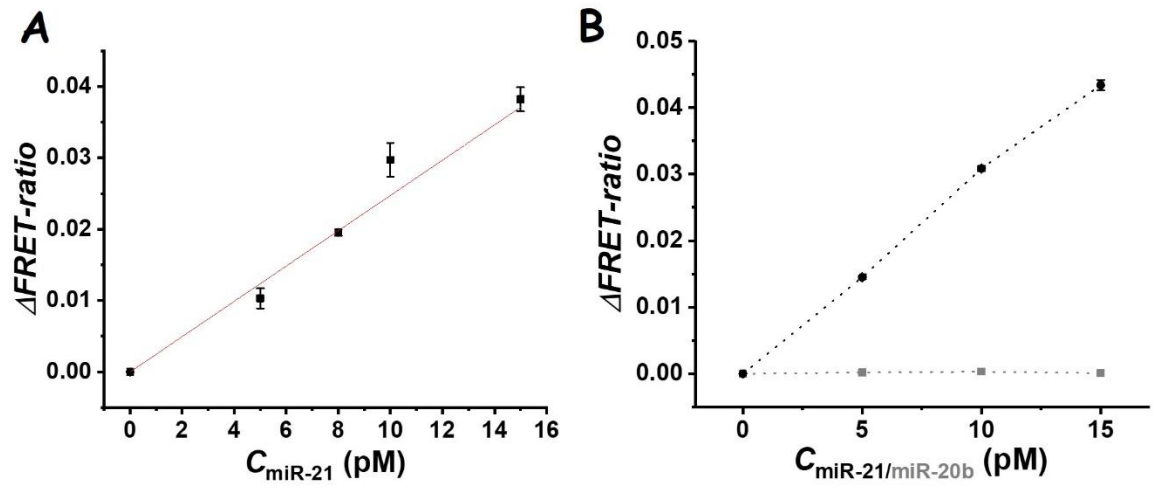

Figure 5.6 (A) Assay calibration curve showed linearly increasing $\Delta FRET\text{-}ratio$ values (the FRET-ratio subtracted by the FRET-ratio without target) over target miR-21 concentration with a LOD of 11 ± 4 attomole (80 ± 30 fM). (B) Target specificity was demonstrated against various amounts of miR-20b.

5.4 Conclusion

In summary, we have demonstrated a nanosensor with the integration of HRCA and TG-FRET for sensitive detection of miRNA based on QD as acceptor and Tb as donor. The exponential amplification efficiency of HRCA and the autofluorescence-suppressed TG-FRET measurement ensure the high sensitivity with a detection limit of 11 ± 4 attomole (80 ± 30 fM) for the target hsa-miR-21. In addition, the versatility of the target miRNA-specific padlock design that can overcome the mismatch-caused positive offset and the specific hybridization of HRCA products with both capture probes and reporter probes guarantee the high selectivity of the proposed method. More importantly, it has great potential for multiplexing miRNA diagnostics because of the flexible design of padlocks toward different miRNAs and the multiplexing capability of QDs without any crosstalk corrections. As the proposed proof-of-concept is a promising and ongoing project, in which the multiplexing adaption to actual clinical samples remained to be demonstrated, we expect that the proposed HRCA-amplified Tb-to-QD nanosensor can become a very useful alternative to current miRNA diagnostic approaches.

6. Summary and outlook

This thesis presents three successful LTCs-based FRET biosensors for miRNA biomarker diagnostics based on isothermal amplification methods and TG measurements. To overcome the analytical challenges arising from the unique characteristics of miRNAs (small size, low abundance, sequence similarity, *etc.*), three different isothermal amplification methods (RCA, CHA, HRCA) were exploited and carefully designed into individual biosensors. TG measurement in combination with long-lived LTCs as donor and short-lived Cy5.5 or QD as acceptors was used to avoid the background interferences including auto-fluorescence of the biological matrix as well as the light scattering from the excitation source. By collecting both FRET-sensitized and FRET-quenched donor PL intensities from individual detection channels, the ratiometric output (the ratio of the time-gated PL intensities of the FRET-sensitized acceptor and FRET-quenched donor) was calculated to quantify the target miRNAs. All of these biosensors provide a homogeneous and one-step assay format, and benefits of sensitivity, selectivity, simplicity, and robustness. All assays were designed to be detected on a clinically approved fluorescence plate reader, which allows the analysts to perform direct clinical application without introducing new instruments.

In the first work, we took the advantages of RCA method, developing an extremely sensitive and specific biosensor for quantifying miRNAs, which was verified to have better performance than TaqMan RT-qPCR. By altering the design of the padlocks toward different miRNAs (miR-21, miR-132 and miR-146a), three miRNAs-specific RCA-amplified biosensors were constructed based on the same strategy, demonstrating the flexibility and versatility of this concept. More importantly, the ability to quantify different miRNAs from various types of clinically relevant samples (human plasma, tissues, and cells), and to obtain significant pathological information from these measurements, indicate that this strategy can be used for advanced miRNA-based diagnostics and research. In another study [171], multiplexing detection for DNAs was realized based on the same

strategy. We combined spectral multiplexing (by introducing different dyes) with temporal multiplexing (by tuning the distances between Tb-to-different dyes), and realized high-order multiplexed detection for four different DNAs.

As the defined structure of dsDNA and the site-specific modifications are available for nucleic acids, it is more straightforward to locate small molecular FRET pairs (LTCs or dyes) and control their distances, which is highly important for temporal multiplexing. In the second work, temporal multiplexed miRNAs detection was achieved by tuning the Tb-to-Cy5.5 distances in two distinct signaling duplexes, resulting in distinct PL decay times of the same FRET pair. We selected two different TG windows to collect PL intensities that fulfill the following prerequisites: i) different target miRNAs have distinct contributions, and ii) there are enough photons in the selected time windows to provide sensitive determination of the targets. The contributions of different miRNAs in different TG windows were deconstructed by a simple matrix calculation, realizing the simultaneous quantification of two distinct miRNAs in a single sample. Unlike other multiplexing strategies that utilize different parameters (*e.g.*, different colors or polarizations), the proposed biosensor only needs one single measurement to distinguish different miRNAs, which will decrease the consumption of analytical reagents and the amounts of clinical samples needed. However, compared to other two-enzyme-involved amplified (RCA, HRCA) biosensors, this CHA-amplified biosensor suffers from the relatively lower sensitivity. While it is still sufficient to detect directly in tissue samples, the lower sensitivity limits its application in plasma samples that contain extremely low amounts of miRNAs. Nevertheless, it is superior in simplify, rapidity, cost-effectiveness, and multiplexing capability.

QDs are excellent FRET acceptor candidates owing to their intrinsic photophysical properties. Especially, their narrow emission bands and size-tunable emission peaks make them superior in multiplexing then dyes. In the third work, we developed a HRCA-amplified nanosensor based on Tb-to-QD FRET. Unfortunately, the implementation of amplification technology with QD-based FRET sensor is not as straightforward as with

dye-based FRET sensor. The compatibility and affinity effectiveness of amplified DNA products and QD are uncertain and often unpredictable. For realizing a sensitive detection we tried different strategies, such as using various endonucleases for obtaining different formats of amplified DNA products, QDs with different size, different padlocks and experimental conditions and, not all attempts could led to the expected results. Nevertheless, I finally managed to develop a highly sensitive miRNA assay based on Tb-to-QD FRET and HRCA. The proof-of-concept was successful but further steps, such as actrual multiplexing and adaption to real clinical samples, are still necessary to translate this nanosensor into clinical diagnostics. Nevertheless, it presents a promising alternative for sensitive miRNA diagnostic and has a strong potential to achieve spectral multiplexing with several different QD colors, or even high-order spectrotemporal multiplexing by tuning distances between each Tb-to-QD FRET pair.

7. Appendix

7.1 Abbreviations

miRNA	microRNA
RT-qPCR	reverse transcription quantitative polymerase chain reaction
NGS	next-generation sequencing
ISH	in situ hybridization
NB	northern blotting
LTCs	luminescent Tb complexes
FRET	Förster resonance energy transfer
TG-FRET	time-gated FRET
QD	quantum dot
PL	photoluminescence
RCA	rolling circle amplification
LOD	limit of detection
THP-1 cells	acute monocytic leukemia cells
CHA	catalytic hairpin assembly
HRCA	hyperbranched rolling circle amplification
PCR	polymerase chain reaction
cDNA	complementary DNA
ssDNA	single-stranded DNA
dsDNA	double-stranded DNA
DSNSA	duplex-specific nuclease signal amplification
LAMP	loop-mediated isothermal amplification
SDA	strand-displacement amplification
HCR	hybridization chain reaction
MB	molecular beacon
BPs	binary probes

LLCs	luminescent lanthanide complexes
NHS	N-hydroxysuccinimide
VB	valence band
CB	conduction band
pre-miRNA	precursor miRNA
Tb	Lumi4-Tb
RCP	rolling circle product
LPS	lipopolysaccharide

7.2 Instrument

Time-resolved FRET measurements were performed by two fluorescence plate readers. **Figure 7.1a** is a modified KRYPTOR compact PLUS (Thermo Fisher Scientific, France) using 500 detection bins of 2 µs integration time. The system has an integrated pulsed nitrogen laser with an excitation wavelength of 337 nm and a repetition rate of 20 Hz. **Figure 7.1b** is a prototype from Edinburgh Instruments (UK) developed during a joined project and referred in this work as plate reader. The system allows time-resolved FRET assay measurements using 4000 detection bins of 2 µs integration time. The excitation source was a pulsed nitrogen laser (MNL 100, LTB Berlin) with an excitation wavelength of 337 nm and a repetition rate of 20 Hz.

The instrumental construction for all used plate readers is shown in **Figure 7.1c**. After sample excitation, a dichroic mirror is used to separate the emission signals from the sample into two individual detection channels. This separation allows the simultaneous measurement of the FRET acceptor signals (ChA) and the FRET donor signals (ChD) using two photomultiplier tubes (PMTs). A further selection of the emission wavelengths inside the channels is obtained by the use of bandpass filters (Semrock), which are optimized for the emission detection of the LTCs and for the Cy5.5 dyes or QD.

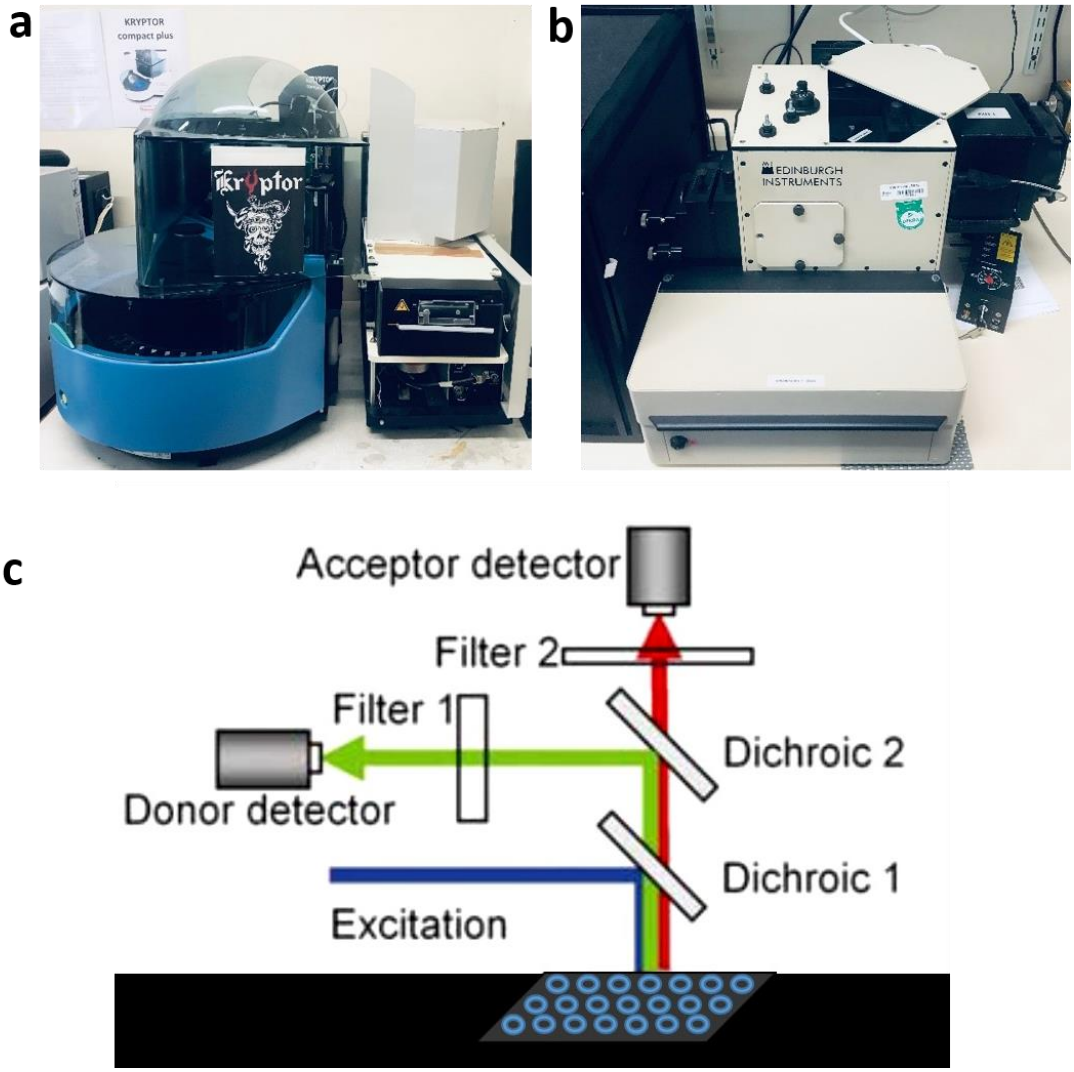

Figure 7.1 Two fluorescence plate readers used in this thesis. (**a**) Modified KRYPTOR compact plus (Thermo Fisher Scientific. (**b**) Prototype from Edinburgh Instruments developed during a joined project. (**c**) Simplified schematic instrumental construction.

8. Bibliography

[1] B. Wightman, I. Ha, and G. Ruvkun, “Posttranscriptional regulation of the heterochronic gene lin-14 by lin-4 mediates temporal pattern formation in C. elegans,” *Cell*, vol. 75, no. 5, pp. 855–862, 1993.

[2] J. Winter, S. Jung, S. Keller, R. I. Gregory, and S. Diederichs, “Many roads to maturity: MicroRNA biogenesis pathways and their regulation,” *Nat. Cell Biol.*, vol. 11, no. 3, pp. 228–234, 2009.

[3] M. Ha and V. N. Kim, “Regulation of microRNA biogenesis,” *Nat. Rev. Mol. Cell Biol.*, vol. 15, no. 8, pp. 509–524, 2014.

[4] S. Lin and R. I. Gregory, “MicroRNA biogenesis pathways in cancer,” *Nat. Rev. Cancer*, vol. 15, no. 6, pp. 321–333, 2015.

[5] R. M. Graybill and R. C. Bailey, “Emerging Biosensing Approaches for microRNA Analysis,” 2016.

[6] H. Dong, J. Lei, L. Ding, Y. Wen, H. Ju, and X. Zhang, “MicroRNA: Function, detection, and bioanalysis,” *Chem. Rev.*, vol. 113, no. 8, pp. 6207–6233, 2013.

[7] B. C. Bernardo, F. J. Charchar, R. C. Y. Lin, and J. R. Mcmullen, “A MicroRNA Guide for Clinicians and Basic Scientists : Background and Experimental Techniques,” *"Heart, Lung Circ.*, vol. 21, no. 3, pp. 131–142, 2012.

[8] G. A. Calin and C. M. Croce, “MicroRNA signatures in human cancers,” *Nat. Rev. Cancer*, vol. 6, no. 11, pp. 857–866, 2006.

[9] A. Esquela-Kerscher and F. J. Slack, “Oncomirs - MicroRNAs with a role in cancer,” *Nat. Rev. Cancer*, vol. 6, no. 4, pp. 259–269, 2006.

[10] N. Pencheva and S. F. Tavazoie, “Control of metastatic progression by microRNA regulatory networks,” *Nat. Cell Biol.*, vol. 15, no. 6, pp. 546–554, 2013.

[11] J. M. Raser and E. K. O’Shea, “Control of stochasticity in eukaryotic gene expression,” *Science*, vol. 304, no. 5678, pp. 1811–1814, 2004.

[12] F. Tang, P. Hajkova, S. C. Barton, K. Lao, and M. A. Surani, “MicroRNA expression profiling of single whole embryonic stem cells,” *Nucleic Acids Res.*, vol. 34, no. 2, pp. 1–7, 2006.

[13] J. Lu *et al.*, “MicroRNA expression profiles classify human cancers,” *Nature*, vol. 435, no. 7043, pp. 834–838, 2005.

[14] X. Chen *et al.*, “Characterization of microRNAs in serum: A novel class of biomarkers for diagnosis of cancer and other diseases,” *Cell Res.*, vol. 18, no. 10, pp. 997–1006, 2008.

[15] P. S. Mitchell *et al.*, “Circulating microRNAs as stable blood-based markers for cancer detection,” *Proc. Natl. Acad. Sci. U. S. A.*, vol. 105, no. 30, pp. 10513–10518, 2008.

[16] K. Wang, S. Zhang, J. Weber, D. Baxter, and D. J. Galas, “Export of microRNAs and microRNA-protective protein by mammalian cells,” *Nucleic Acids Res.*, vol. 38, no. 20, pp. 7248–7259, 2010.

[17] J. D. Arroyo *et al.*, “Argonaute2 complexes carry a population of circulating microRNAs independent of vesicles in human plasma,” *Proc. Natl. Acad. Sci. U. S. A.*, vol. 108, no. 12, pp. 5003–5008, 2011.

[18] J. Skog *et al.*, “Glioblastoma microvesicles transport RNA and proteins that promote tumour growth and provide diagnostic biomarkers,” *Nat. Cell Biol.*, vol. 10, no. 12, pp. 1470–1476, 2008.

[19] Y. Zhang *et al.*, "Secreted Monocytic miR-150 Enhances Targeted Endothelial Cell Migration," *Mol. Cell*, vol. 39, no. 1, pp. 133–144, 2010.

[20] M. P. Caby, D. Lankar, C. Vincendeau-Scherrer, G. Raposo, and C. Bonnerot, "Exosomal-like vesicles are present in human blood plasma," *Int. Immunol.*, vol. 17, no. 7, pp. 879–887, 2005.

[21] H. Valadi, K. Ekström, A. Bossios, M. Sjöstrand, J. J. Lee, and J. O. Lötvall, "Exosome-mediated transfer of mRNAs and microRNAs is a novel mechanism of genetic exchange between cells," *Nat. Cell Biol.*, vol. 9, no. 6, pp. 654–659, 2007.

[22] M. Weiland, X. H. Gao, L. Zhou, and Q. S. Mi, "Small RNAs have a large impact: Circulating microRNAs as biomarkers for human diseases," *RNA Biol.*, vol. 9, no. 6, pp. 850–859, 2012.

[23] N. Rosenfeld *et al.*, "MicroRNAs accurately identify cancer tissue origin," *Nat. Biotechnol.*, vol. 26, no. 4, pp. 462–469, 2008.

[24] S. L. Yu *et al.*, "MicroRNA Signature Predicts Survival and Relapse in Lung Cancer," *Cancer Cell*, vol. 13, no. 1, pp. 48–57, 2008.

[25] G. A. Calin *et al.*, "Human microRNA genes are frequently located at fragile sites and genomic regions involved in cancers," *PNAS*, vol. 101, no. 9, pp. 2999–3004, 2004.

[26] J. Wang, J. Chen, and S. Sen, "MicroRNA as Biomarkers and Diagnostics," *J. Cell. Physiol.*, vol. 231, no. 1, pp. 25–30, 2016.

[27] M. Esteller, "Non-coding RNAs in human disease," *Nat. Rev. Genet.*, vol. 12, no. 12, pp. 861–874, 2011.

[28] G. A. Calin *et al.*, "MicroRNA Profiling Reveals Distinct Signatures in B Cell Chronic Lymphocytic Leukemias," *PNAS*, vol. 101, no. 32, pp. 11755-11760, 2004.

[29] M. V. Iorio *et al.*, "MicroRNA gene expression deregulation in human breast cancer," *Cancer Res.*, vol. 65, no. 16, pp. 7065–7070, 2005.

[30] N. Yanaihara *et al.*, "Unique microRNA molecular profiles in lung cancer diagnosis and prognosis," *Cancer Cell*, vol. 9, no. 3, pp. 189–198, 2006.

[31] M. V. Iorio *et al.*, "MicroRNA signatures in human ovarian cancer," *Cancer Res.*, vol. 67, no. 18, pp. 8699–8707, 2007.

[32] K. P. Porkka, M. J. Pfeiffer, K. K. Waltering, R. L. Vessella, T. L. J. Tammela, and T. Visakorpi, "MicroRNA expression profiling in prostate cancer," *Cancer Res.*, vol. 67, no. 13, pp. 6130–6135, 2007.

[33] J. Wang and S. Sen, "MicroRNA functional network in pancreatic cancer: From biology to biomarkers of disease," *J. Biosci.*, vol. 36, no. 3, pp. 481–491, 2011.

[34] Y. H. Lee and G. G. Song, "Circulating microRNAs (cmiRNAs) as novel potential biomarkers for hepatocellular carcinoma," *Neoplasma*, vol. 60, no. 5, pp. 607–616, 2013.

[35] X. J. Chen *et al.*, "Clinical value of integrated-signature miRNAs in colorectal cancer: miRNA expression profiling analysis and experimental validation," *Oncotarget*, vol. 6, no. 35, pp. 37544–37556, 2015.

[36] S. A. Melo *et al.*, "A TARBP2 mutation in human cancer impairs microRNA processing and DICER1 function," *Nat. Genet.*, vol. 41, no. 3, pp. 365–370, 2009.

[37] M. S. Kumar, J. Lu, K. L. Mercer, T. R. Golub, and T. Jacks, “Impaired microRNA processing enhances cellular transformation and tumorigenesis,” *Nat. Genet.*, vol. 39, no. 5, pp. 673–677, 2007.

[38] D. A. Hill *et al.*, “DICER1 mutations in familial pleuropulmonary blastoma,” *Science*, vol. 325, no. 5943, p. 965, 2009.

[39] S. A. Melo *et al.*, “A genetic defect in exportin-5 traps precursor MicroRNAs in the nucleus of cancer cells,” *Cancer Cell*, vol. 18, no. 4, pp. 303–315, 2010.

[40] J. T. Huang, J. Wang, V. Srivastava, S. Sen, and S. M. Liu, “MicroRNA machinery genes as novel biomarkers for cancer,” *Front. Oncol.*, vol. 4 MAY, no. May, pp. 1–10, 2014.

[41] M. Matsuoka and M. Ashikari, “A quantitative trait locus regulating rice grain width,” *Nat. Genet.*, vol. 39, no. 5, pp. 583–584, 2007.

[42] Y. Hu, W. Lan, and D. Miller, “Bioinformatics in MicroRNA Research, Methods in Molecular Biology,” vol. 1617, pp. 169–177, 2017.

[43] V. S. Nair, L. S. Maeda, and J. P. A. Ioannidis, “Clinical outcome prediction by MicroRNAs in human cancer: A systematic review,” *J. Natl. Cancer Inst.*, vol. 104, no. 7, pp. 528–540, 2012.

[44] J. A. Chan, A. M. Krichevsky, and K. S. Kosik, “MicroRNA-21 is an antiapoptotic factor in human glioblastoma cells,” *Cancer Res.*, vol. 65, no. 14, pp. 6029–6033, 2005.

[45] F. Meng, R. Henson, H. Wehbe-Janek, K. Ghoshal, S. T. Jacob, and T. Patel, “MicroRNA-21 Regulates Expression of the PTEN Tumor Suppressor Gene in Human Hepatocellular Cancer,” *Gastroenterology*, vol. 133, no. 2, pp. 647–658, 2007.

[46] S. Zhu, M. L. Si, H. Wu, and Y. Y. Mo, "MicroRNA-21 targets the tumor suppressor gene tropomyosin 1 (TPM1)," *J. Biol. Chem.*, vol. 282, no. 19, pp. 14328–14336, 2007.

[47] J. R. M. Sophie Mokas *et al.*, "Uncoupling Stress Granule Assembly and Translation Initiation Inhibition," *Mol. Biol. Cell*, vol. 20, no. August, pp. 2673–2683, 2009.

[48] P. P. Medina, M. Nolde, and F. J. Slack, "OncomiR addiction in an in vivo model of microRNA-21-induced pre-B-cell lymphoma," *Nature*, vol. 467, no. 7311, pp. 86–90, 2010.

[49] B. J. Reinhart *et al.*, "The 21-nucleotide let-7 RNA regulates developmental timing in Caenorhabditis elegans," *Nature*, vol. 403, no. 6772, pp. 901–906, 2000.

[50] G. Adrian *et al.*, "Human MicroRNA Genes Are Frequently Located at Fragile Sites and Genomic Regions Involved in Cancers," *PNAS*, vol. 101, no. 9, pp. 2999–3004, 2004.

[51] S. M. Johnson *et al.*, "RAS is regulated by the let-7 microRNA family," *Cell*, vol. 120, no. 5, pp. 635–647, 2005.

[52] I. Medicine, "MicroRNAs in medicine," *In Medicine*. 2008.

[53] H. M. Heneghan, N. Miller, R. Kelly, J. Newell, and M. J. Kerin, "Systemic miRNA-195 Differentiates Breast Cancer from Other Malignancies and Is a Potential Biomarker for Detecting Noninvasive and Early Stage Disease," *Oncologist*, vol. 15, no. 7, pp. 673–682, 2010.

[54] J. Wang *et al.*, "MicroRNAs in plasma of pancreatic ductal adenocarcinoma patients as novel blood-based biomarkers of disease," *Cancer Prev. Res.*, vol. 2, no. 9, pp. 807–813, 2009.

[55] Z. Huang, D. Huang, S. Ni, Z. Peng, W. Sheng, and X. Du, “Plasma microRNAs are promising novel biomarkers for early detection of colorectal cancer,” *Int. J. Cancer*, vol. 127, no. 1, pp. 118–126, 2010.

[56] L. Mengual, J. J. Lozano, M. Ingelmo-Torres, C. Gazquez, M. J. Ribal, and A. Alcaraz, “Using microRNA profiling in urine samples to develop a non-invasive test for bladder cancer,” *Int. J. Cancer*, vol. 133, no. 11, pp. 2631–2641, 2013.

[57] J. Wang *et al.*, “Next generation sequencing of pancreatic cyst fluid microRNAs from low grade-benign and high grade-invasive lesions,” *Cancer Lett.*, vol. 356, no. 2, pp. 404–409, 2015.

[58] J. Wang *et al.*, “Circulating microRNAs in pancreatic juice as candidate biomarkers of pancreatic cancer,” *J. Cancer*, vol. 5, no. 8, pp. 696–705, 2014.

[59] L. Xing, N. W. Todd, L. Yu, H. Fang, and F. Jiang, “Early detection of squamous cell lung cancer in sputum by a panel of microRNA markers,” *Mod. Pathol.*, vol. 23, no. 8, pp. 1157–1164, 2010.

[60] L. B. Nielsen *et al.*, “Circulating levels of MicroRNA from children with newly diagnosed type 1 diabetes and healthy controls: Evidence that miR-25 associates to residual beta-cell function and glycaemic control during disease progression,” *Exp. Diabetes Res.*, vol. 2012, 2012.

[61] Y. Liu *et al.*, “The role of circulating microRNA-126 (miR-126): A novel biomarker for screening prediabetes and newly diagnosed type 2 diabetes mellitus,” *Int. J. Mol. Sci.*, vol. 15, no. 6, pp. 10567–10577, 2014.

[62] Z. Yang *et al.*, “Serum miR-23a, a potential biomarker for diagnosis of pre-diabetes and type 2 diabetes,” *Acta Diabetol.*, vol. 51, no. 5, pp. 823–831, 2014.

[63] C. Zhao *et al.*, “Early second-trimester serum miRNA profiling predicts gestational diabetes mellitus,” *PLoS One*, vol. 6, no. 8, 2011.

[64] X. Cao, G. Yeo, A. R. Muotri, T. Kuwabara, and F. H. Gage, “Noncoding RNAs in the Mammalian Central Nervous System,” *Annu. Rev. Neurosci.*, vol. 29, no. 1, pp. 77–103, 2006.

[65] C. Zhao, G. Sun, S. Li, and Y. Shi, “A feedback regulatory loop involving microRNA-9 and nuclear receptor TLX in neural stem cell fate determination,” *Nat. Struct. Mol. Biol.*, vol. 16, no. 4, pp. 365–371, 2009.

[66] G. M. Schratt *et al.*, “A brain-specific microRNA regulates dendritic spine development,” *Nature*, vol. 439, no. 7074, pp. 283–289, 2006.

[67] M. F. Mehler and J. S. Mattick, “Noncoding RNAs and RNA editing in brain development, functional diversification, and neurological disease,” *Physiol. Rev.*, vol. 87, no. 3, pp. 799–823, 2007.

[68] W. X. Wang *et al.*, “The expression of microRNA miR-107 decreases early in Alzheimer’s disease and may accelerate disease progression through regulation of β-site amyloid precursor protein-cleaving enzyme 1,” *J. Neurosci.*, vol. 28, no. 5, pp. 1213–1223, 2008.

[69] R. Margis, R. Margis, and C. R. M. Rieder, “Identification of blood microRNAs associated to Parkinsonós disease,” *J. Biotechnol.*, vol. 152, no. 3, pp. 96–101, 2011.

[70] L. E. Philippen, E. Dirkx, P. A. da Costa-Martins, and L. J. De Windt, “Non-coding RNA in control of gene regulatory programs in cardiac development and disease,” *J. Mol. Cell. Cardiol.*, vol. 89, pp. 51–58, 2015.

[71] A. Zampetaki and M. Mayr, “MicroRNAs in vascular and metabolic disease,” *Circ. Res.*, vol. 110, no. 3, pp. 508–522, 2012.

[72] S. P. R. Romaine, M. Tomaszewski, G. Condorelli, and N. J. Samani, “MicroRNAs in cardiovascular disease: An introduction for clinicians,” *Heart*, vol. 101, no. 12, pp. 921–928, 2015.

[73] J. Ai *et al.*, “Circulating microRNA-1 as a potential novel biomarker for acute myocardial infarction,” *Biochem. Biophys. Res. Commun.*, vol. 391, no. 1, pp. 73–77, 2010.

[74] G. K. Wang *et al.*, “Circulating microRNA: A novel potential biomarker for early diagnosis of acute myocardial infarction in humans,” *Eur. Heart J.*, vol. 31, no. 6, pp. 659–666, 2010.

[75] A. Zampetaki *et al.*, “Prospective study on circulating microRNAs and risk of myocardial infarction,” *J. Am. Coll. Cardiol.*, vol. 60, no. 4, pp. 290–299, 2012.

[76] A. Zampetaki *et al.*, “Circulating miRNAs as marker for liver injury in HIV patients,” *Hepatology*, vol. 61, no. 1, pp. 46–55, 2014.

[77] I. Z. Ben-Dov *et al.*, “Urine microRNA as potential biomarkers of autosomal dominant polycystic kidney disease progression: Description of miRNA profiles at baseline,” *PLoS One*, vol. 9, no. 1, pp. 1–8, 2014.

[78] Y. Zhang *et al.*, “Plasma microRNA-122 as a biomarker for viral-, alcohol-, and chemical-related hepatic diseases,” *Clin. Chem.*, vol. 56, no. 12, pp. 1830–1838, 2010.

[79] Z. Zhao *et al.*, “Circulating microRNA miR-323-3p as a biomarker of ectopic pregnancy,” *Clin. Chem.*, vol. 58, no. 5, pp. 896–905, 2012.

[80] A. J. Qavi, J. T. Kindt, and R. C. Bailey, “Sizing up the future of microRNA analysis,” *Anal. Bioanal. Chem.*, vol. 398, no. 6, pp. 2535–2549, 2010.

[81] L. P. Lim *et al.*, “The microRNAs of,” *Genes Dev.*, pp. 991–1008, 2003.

[82] D. P. Bartel, “MicroRNAs: Genomics, Biogenesis, Mechanism, and Function,” *Cell*, vol. 116, no. 2, pp. 281–297, 2004.

[83] R. C. Friedman, K. K. H. Farh, C. B. Burge, and D. P. Bartel, “Most mammalian mRNAs are conserved targets of microRNAs,” *Genome Res.*, vol. 19, no. 1, pp. 92–105, 2009.

[84] S. Wu *et al.*, “Multiple microRNAs modulate p21Cip1/Waf1 expression by directly targeting its 3′ untranslated region,” *Oncogene*, vol. 29, no. 15, pp. 2302–2308, 2010.

[85] C. Chen, R. Tan, L. Wong, R. Fekete, and J. Halsey, “PCR Protocols-Chapter 8: Quantitation of MicroRNAs by Real-Time RT-qPCR,” *Methods Mol. Biol*, vol. 687, no. 4, pp. 113–134, 2011.

[86] A. R. Chandrasekaran, J. A. Punnoose, L. Zhou, P. Dey, B. K. Dey, and K. Halvorsen, “DNA nanotechnology approaches for microRNA detection and diagnosis,” *Nucleic Acids Res.*, vol. 47, no. 20, pp. 10489–10505, 2019.

[87] M. L. Metzker, “Sequencing technologies the next generation,” *Nat. Rev. Genet.*, vol. 11, no. 1, pp. 31–46, 2010.

[88] P. T. Nelson, D. A. Baldwin, W. P. Kloosterman, S. Kauppinen, R. H. A. Plasterk, and Z. Mourelatos, “RAKE and LNA-ISH reveal microRNA expression and localization in archival human brain,” *RNA*, vol. 12, no. 2, pp. 187–191, 2006.

[89] M. O. Urbanek, A. U. Nawrocka, and W. J. Krzyzosiak, “Small RNA detection by in situ hybridization methods,” *Int. J. Mol. Sci.*, vol. 16, no. 6, pp. 13259–13286, 2015.

[90] V. P. Dave *et al.*, “MicroRNA amplification and detection technologies: opportunities and challenges for point of care diagnostics,” *Lab. Investig.*, vol. 99, no. 4, pp. 452–469, 2019.

[91] S. Streit, C. W. Michalski, M. Erkan, J. Kleeff, and H. Friess, “Northern blot analysis for detection and quantification of RNA in pancreatic cancer cells and tissues,” *Nat. Protoc.*, vol. 4, no. 1, pp. 37–43, 2009.

[92] C. C. Pritchard, H. H. Cheng, and M. Tewari, “MicroRNA profiling: Approaches and considerations,” *Nat. Rev. Genet.*, vol. 13, no. 5, pp. 358–369, 2012.

[93] P. Mestdagh *et al.*, “Evaluation of quantitative miRNA expression platforms in the microRNA quality control (miRQC) study,” *Nat. Methods*, vol. 11, no. 8, pp. 809–815, 2014.

[94] H. T. Allawi *et al.*, “Quantitation of microRNAs using a modified Invader assay,” *RNA*, vol. 10, pp. 1153–1161, 2004.

[95] R. Deng, K. Zhang, and J. Li, “Isothermal Amplification for MicroRNA Detection: From the Test Tube to the Cell,” *Acc. Chem. Res.*, vol. 50, no. 4, pp. 1059–1068, 2017.

[96] A. Fire and S. Q. Xu, “Rolling replication of short DNA circles,” *PNAS*, vol. 92, no. 10, pp. 4641–4645, 1995.

[97] D. Liu, S. L. Daubendiek, M. A. Zillman, K. Ryan, and E. T. Kool, “Rolling circle DNA synthesis: Small circular oligonucleotides as efficient templates for DNA polymerases,” *J. Am. Chem. Soc.*, vol. 118, no. 7, pp. 1587–1594, 1996.

[98] J. Sp, K. J, and K. J. A, “microRNA detection system based on padlock probes and rolling circle amplification,” *RNA*, vol. 12, pp. 1747–52, 2006.

[99] Y. Zhou, Q. Huang, J. Gao, J. Lu, X. Shen, and C. Fan, “A dumbbell probe-mediated rolling circle amplification strategy for highly sensitive microRNA detection,” *Nucleic Acids Res.*, vol. 38, no. 15, 2010.

[100] J. Chen *et al.*, "Isothermal Amplification on a Structure-Switchable Symmetric Toehold Dumbbell-Template: A Strategy Enabling MicroRNA Analysis at the Single-Cell Level with Ultrahigh Specificity and Accuracy," *Anal. Chem.*, vol. 90, no. 1, pp. 859–865, 2018.

[101] Y. Long, X. Zhou, and D. Xing, "An isothermal and sensitive nucleic acids assay by target sequence recycled rolling circle amplification," *Biosens. Bioelectron.*, vol. 46, pp. 102–107, 2013.

[102] P. M. Lizardi, X. Huang, Z. Zhu, P. Bray-Ward, D. C. Thomas, and D. C. Ward, "Mutation detection and single-molecule counting using isothermal rolling-circle amplification," *Nat. Genet.*, vol. 19, no. 3, pp. 225–232, 1998.

[103] L. Yan *et al.*, "Isothermal amplified detection of DNA and RNA," *Mol. Biosyst.*, vol. 10, no. 5, pp. 970–1003, 2014.

[104] H. L. Chen *et al.*, "Nucleic acid amplification-based methods for microRNA detection," *Anal. Methods*, vol. 7, no. 6, pp. 2258–2263, 2015.

[105] Y. Cheng, X. Zhang, Z. Li, X. Jiao, Y. Wang, and Y. Zhang, "Highly Sensitive Determination of microRNA Using Target-Primed and Branched Rolling-Circle Amplification," *Angew. Chemie*, vol. 121, no. 18, pp. 3318–3322, 2009.

[106] G. J. S. Lohman, Y. Zhang, A. M. Zhelkovsky, E. J. Cantor, and T. C. Evans, "Efficient DNA ligation in DNA-RNA hybrid helices by Chlorella virus DNA ligase," *Nucleic Acids Res.*, vol. 42, no. 3, pp. 1831–1844, 2014.

[107] J. Jin, S. Vaud, A. M. Zhelkovsky, J. Posfai, and L. A. McReynolds, "Sensitive and specific miRNA detection method using SplintR Ligase," *Nucleic Acids Res.*, vol. 44, no. 13, pp. e116, 2016.

[108] V. E. Anisimova, D. V. Rebrikov, P. A. Zhulidov, D. B. Staroverov, S. A. Lukyanov, and A. S. Shcheglov, “Renaturation, activation, and practical use of recombinant duplex-specific nuclease from Kamchatka crab,” *Biochem.*, vol. 71, no. 5, pp. 513–519, 2006.

[109] T. Tian *et al.*, “Sensitive and convenient detection of microRNAs based on cascade amplification by catalytic dnazymes,” *Chem. Eur. J.*, vol. 19, no. 1, pp. 92–95, 2013.

[110] S. Wang *et al.*, “Novel amplex red oxidases based on noncanonical DNA structures: Property studies and applications in microRNA detection,” *Anal. Chem.*, vol. 86, no. 6, pp. 2925–2930, 2014.

[111] B. C. Yin, Y. Q. Liu, and B. C. Ye, “One-step, multiplexed fluorescence detection of microRNAs based on duplex-specific nuclease signal amplification,” *J. Am. Chem. Soc.*, vol. 134, no. 11, pp. 5064–5067, 2012.

[112] Y. Wang, C. Lau, and J. Lu, “Target-initiated labeling for the dual-amplified detection of multiple microRNAs,” *Anal. Chim. Acta*, vol. 992, pp. 76–84, 2017.

[113] T. Notomi *et al.*, “Loop-mediated isothermal amplification of DNA,” *Nucleic Acids Res.*, vol. 28, no. 12, p. e63, 2000.

[114] J. Ye, M. Xu, X. Tian, S. Cai, and S. Zeng, “Research advances in the detection of miRNA,” *J. Pharm. Anal.*, vol. 9, no. 4, pp. 217–226, 2019.

[115] Y. S. Jiang, S. Bhadra, B. Li, Y. R. Wu, J. N. Milligan, and A. D. Ellington, “Robust Strand Exchange Reactions for the Sequence-Specific, Real-Time Detection of Nucleic Acid Amplicons,” *Anal. Chem.*, vol. 87, no. 6, pp. 3314–3320, 2015.

[116] Y. Sun, H. Tian, C. Liu, Y. Sun, and Z. Li, “One-step detection of microRNA with high sensitivity and specificity: Via target-triggered loop-mediated isothermal

amplification (TT-LAMP)," *Chem. Commun.*, vol. 53, no. 80, pp. 11040–11043, 2017.

[117] W. Liu *et al.*, "Establishment of an accurate and fast detection method using molecular beacons in loop-mediated isothermal amplification assay," *Sci. Rep.*, vol. 7, no. January, 2017.

[118] R. Duan *et al.*, "Lab in a tube: Ultrasensitive detection of MicroRNAs at the single-cell level and in breast cancer patients using quadratic isothermal amplification," *J. Am. Chem. Soc.*, vol. 135, no. 12, pp. 4604–4607, 2013.

[119] B. Z. Chi, R. P. Liang, W. Bin Qiu, Y. H. Yuan, and J. D. Qiu, "Direct fluorescence detection of microRNA based on enzymatically engineered primer extension poly-thymine (EPEPT) reaction using copper nanoparticles as nano-dye," *Biosens. Bioelectron.*, vol. 87, pp. 216–221, 2017.

[120] A. Chen, S. Ma, Y. Zhuo, Y. Chai, and R. Yuan, "In Situ Electrochemical Generation of Electrochemiluminescent Silver Naonoclusters on Target-Cycling Synchronized Rolling Circle Amplification Platform for MicroRNA Detection," *Anal. Chem.*, vol. 88, no. 6, pp. 3203–3210, 2016.

[121] P. Yin, H. M. T. Choi, C. R. Calvert, and N. A. Pierce, "Programming biomolecular self-assembly pathways," *Nature*, vol. 451, no. 7176, pp. 318–322, 2008.

[122] X. Chen, N. Briggs, J. R. McLain, and A. D. Ellington, "Stacking nonenzymatic circuits for high signal gain," *PNAS.*, vol. 110, no. 14, pp. 5386–5391, 2013.

[123] Y. S. Jiang, S. Bhadra, B. Li, and A. D. Ellington, "Mismatches improve the performance of strand-displacement nucleic acid circuits," *Angew. Chemie - Int. Ed.*, vol. 53, no. 7, pp. 1845–1848, 2014.

[124] Y. Zhang *et al.*, "A simple electrochemical biosensor for highly sensitive and specific detection of microRNA based on mismatched catalytic hairpin assembly," *Biosens. Bioelectron.*, vol. 68, pp. 343–349, 2015.

[125] J. Li *et al.*, "An enzyme-free surface plasmon resonance biosensor for real-time detecting microRNA based on allosteric effect of mismatched catalytic hairpin assembly," *Biosens. Bioelectron.*, vol. 77, pp. 435–441, 2016.

[126] X. Li *et al.*, "A novel surface plasmon resonance biosensor for enzyme-free and highly sensitive detection of microRNA based on multi component nucleic acid enzyme (MNAzyme)-mediated catalyzed hairpin assembly," *Biosens. Bioelectron.*, vol. 80, pp. 98–104, 2016.

[127] R. M. Dirks and N. A. Pierce, "Triggered amplification by hybridization chain reaction," *PNAS*, vol. 101, no. 43, pp. 15275–15278, 2004.

[128] Y. X. Chen, K. J. Huang, and K. X. Niu, "Recent advances in signal amplification strategy based on oligonucleotide and nanomaterials for microRNA detection-a review," *Biosens. Bioelectron.*, vol. 99, no. August 2017, pp. 612–624, 2018.

[129] J. Franck, "The theory of Klein and Rosseland applied to fluorescence, photochemical processes and the electron emission from hot substances," *ZPhys-e.A: Hadrons Nucl.*, vol. 9, pp. 259–266, 1922.

[130] G. Cario and J. Franck, "The dissociation of hydrogen molecules by means of excited mercury atoms," *ZPhys-e.A: Hadrons Nucl.*, vol. 11, pp. 161–166, 1922.

[131] J. Perrin, C. R. Hebd, "Fluorescence and molecular Induction by resonance," *Seances Acad. Sci.*, vol. 184, pp. 1097–1100, 1927.

[132] F. Perrin, "Interaction entre atomes normal et activé. Transferts d'activation. Formation d'une molécule activée," *Ann. Phys.*, vol. 12, pp. 283–314, 1932.

[133] J. Frenkel, “Über quantenmechanische Energieübertragung zwischen atomaren Systemen,” *Zeitschrift für Phys.*, vol. 58, no. 11–12, pp. 794–804, 1929.

[134] T. Förster, “Energiewanderung und Fluoreszenz,” *Naturwissenschaften*, vol. 33, pp. 166–175, 1946.

[135] C. Schaefer and F. Reiche, “Ein Beitrag zur Theorie der Gitterinversion,” *Ann. Phys.*, vol. 337, no. 8, pp. 577–588, 1910.

[136] T. Förster, “Zwischenmolekulare Energiewanderung und Fluoreszenz,” *Ann. Phys.*, vol. 437, no. 1–2. pp. 55–75, 1948.

[137] T. Förster, “Experimentelle und theoretische Untersuchung des zwischenmolekularen Übergangs von Elektronenanregungsenergie,” *Zeitschrift fur Naturforsch. - Sect. A J. Phys. Sci.*, vol. 4, no. 5, pp. 321–327, 1949.

[138] T. Mechanisms and O. F. Electronic, “Transfer Mechanisms of Electronic Excitation,” *10th Spiers Memorial. Lectrure*, no. 10, pp. 7–17, 1959.

[139] R. M. Clegg, “The history of FRET : From conception through the labors of birth,” *Rev. Fluoresc.*, vol. 3, pp. 1–45, 2006.

[140] N. Hildebrandt, “How to Apply FRET: From Experimental Design to Data Analysis,” *FRET - Förster Reson. Energy Transf. From Theory to Appl.*, pp. 105–163, 2013.

[141] N. Hildebrandt *et al.*, “Energy transfer with semiconductor quantum dot bioconjugates: A versatile platform for biosensing, energy harvesting, and other developing applications,” *Chem. Rev.*, vol. 117, no. 2, pp. 536–711, 2017.

[142] D. Shrestha, A. Jenei, P. Nagy, G. Vereb, and J. Szöllősi, “Understanding FRET as a Research Tool for Cellular Studies,” *Int. J. Mol. Sci.*, vol. 16, no. 4, pp. 6718-6756, 2015.

[143] J. R. Lakowicz, *Principles of fluorescence spectroscopy*. 2006.

[144] H. Sahoo, “Förster resonance energy transfer - A spectroscopic nanoruler: Principle and applications,” *J. Photochem. Photobiol. C Photochem. Rev.*, vol. 12, no. 1, pp. 20–30, 2011.

[145] V. V. Didenko, “DNA probes using fluorescence resonance energy transfer (FRET): Designs and applications,” *Biotechniques*, vol. 31, no. 5, pp. 1106–1121, 2001.

[146] J. Guo, J. Ju, and N. J. Turro, “Fluorescent hybridization probes for nucleic acid detection,” *Anal. Bioanal. Chem.*, vol. 402, no. 10, pp. 3115–3125, 2012.

[147] K. Binnemans, “Lanthanide-based luminescent hybrid materials,” *Chem. Rev.*, vol. 109, no. 9, pp. 4283–4374, 2009.

[148] E. G. Moore, A. P. S. Samuel, and K. N. Raymond, “From antenna to assay: lessons learned in lanthanide luminescence,” *Acc. Chem. Res.*, vol. 42, no. 4, pp. 542–552, 2009.

[149] J. C. G. Bünzli and C. Piguet, “Taking advantage of luminescent lanthanide ions,” *Chem. Soc. Rev.*, vol. 34, no. 12, pp. 1048–1077, 2005.

[150] I. Hemmilä and V. Laitala, “Progress in lanthanides as luminescent probes,” *J. Fluoresc.*, vol. 15, no. 4, pp. 529–542, 2005.

[151] M. C. Heffern, L. M. Matosziuk, and T. J. Meade, “Lanthanide probes for bioresponsive imaging,” *Chem. Rev.*, vol. 114, no. 8, pp. 4496–4539, 2014.

[152] J. C. G. Bünzli, “Luminescent lanthanide probes as diagnostic and therapeutic tools,” *Met. Ions Biol. Syst.*, vol. 42, pp. 39–75, 2004.

[153] O. Chau, D. Goeleven, and R. Oujja, “Spectroscopic properties and design of highly luminescent lanthanide coordination complexes,” *Coord. Chem. Rev.*, vol. 196, no. 2000, pp. 165–195, 2014.

[154] J. Kido, H. Hayase, K. Hongawa, K. Nagai, and K. Okuyama, “Bright red light-emitting organic electroluminescent devices having a europium complex as an emitter,” *Appl. Phys. Lett.*, vol. 65, no. 17, pp. 2124–2126, 1994.

[155] J. C. G. Bünzli, “Lanthanide luminescence for biomedical analyses and imaging,” *Chem. Rev.*, vol. 110, no. 5, pp. 2729–2755, 2010.

[156] J. Rocha, L. D. Carlos, F. A. A. Paz, and D. Ananias, “Luminescent multifunctional lanthanides-based metal-organic frameworks,” *Chem. Soc. Rev.*, vol. 40, no. 2, pp. 926–940, 2011.

[157] V. V. Zherdeva and A. P. Savitsky, “Using lanthanide-based resonance energy transfer for in vitro and in vivo studies of biological processes,” *Biochemistry (Moscow)*, vol. 77, no. 13, pp. 1553–1574, 2012.

[158] S. I. Weissman, “Intramolecular energy transfer the fluorescence of complexes of Europium,” *J. Chem. Phys.*, vol. 10, no. 4, pp. 214–217, 1942.

[159] J. C. G. Bünzli, “Lanthanide light for biology and medical diagnosis,” *J. Lumin.*, vol. 170, pp. 866–878, 2016.

[160] G. A. Crosby, R. E. Whan, and R. M. Alire, “Intramolecular energy transfer in rare earth chelates. Role of the triplet state,” *J. Chem. Phys.*, vol. 34, no. 3, pp. 743–748, 1961.

[161] C. Andraud, “Efficient sensitization process of europium, ytterbium and neodymium through charge-transfer excited state,” *Inorg. Chem.*, vol. 47, no. 22, pp. 10258–10268, 2008.

[162] S. V. Eliseeva and J. C. G. Bünzli, “Lanthanide luminescence for functional materials and bio-sciences,” *Chem. Soc. Rev.*, vol. 39, no. 1, pp. 189–227, 2010.

[163] O. A. Goryacheva, N. V. Beloglazova, A. M. Vostrikova, M. V. Pozharov, A. M. Sobolev, and I. Y. Goryacheva, “Lanthanide-to-quantum dot Förster resonance energy transfer (FRET): Application for immunoassay,” *Talanta*, vol. 164, no. September 2016, pp. 377–385, 2017.

[164] C. Chen *et al.*, “Single-Nanoparticle Cell Barcoding by Tunable FRET from Lanthanides to Quantum Dots,” *Angew. Chemie - Int. Ed.*, vol. 57, no. 41, pp. 13686–13690, 2018.

[165] I. Hemmilii, “Luminescent lanthanide chelates-a way to more sensitive diagnostic methods,” *J. Alloys Compd.*, vol. 225, pp. 480–485, 1995.

[166] J. Yuan and G. Wang, “Lanthanide-based luminescence probes and time-resolved luminescence bioassays,” *Trends Analyt. Chem.*, vol. 25, no. 5, pp. 490–500, 2006.

[167] J. Guo *et al.*, “Conformational Details of Quantum Dot-DNA Resolved by Förster Resonance Energy Transfer Lifetime Nanoruler,” *ACS Nano*, vol. 13, no. 1, pp. 505–514, 2019.

[168] K. E. Sapsford, L. Berti, and I. L. Medintz, “Materials for fluorescence resonance energy transfer analysis: Beyond traditional donor-acceptor combinations,” *Angew. Chemie - Int. Ed.*, vol. 45, no. 28, pp. 4562–4589, 2006.

[169] N. Hildebrandt, K. D. Wegner, and W. R. Algar, “Luminescent terbium complexes: Superior Förster resonance energy transfer donors for flexible and sensitive multiplexed biosensing,” *Coord. Chem. Rev.*, vol. 273–274, pp. 125–138, 2014.

[170] Z. W. Jin *et al.*, "A Rapid, Amplification-Free, and Sensitive Diagnostic Assay for Single-Step Multiplexed Fluorescence Detection of MicroRNA," *Angew. Chemie - Int. Ed*, vol. 54, pp. 10024 –10029, 2015.

[171] X. Qiu, J. Guo, J. Xu, and N. Hildebrandt, "Three-Dimensional FRET Multiplexing for DNA Quantification with Attomolar Detection Limits," *J. Phys. Chem. Lett.*, vol. 9, no. 15, pp. 4379–4384, 2018.

[172] D. V. Nguyen, A. B. Arpat, N. Wang, and R. J. Carroll, "DNA microarray experiments: Biological and technological aspects," *Biometrics*, vol. 58, no. 4, pp. 701–717, 2002.

[173] U. Schobel, H. J. Egelhaaf, A. Brecht, D. Oelkrug, and G. Gauglitz, "New donor acceptor pair for fluorescent immunoassays by energy transfer," *Bioconjug. Chem.*, vol. 10, no. 6, pp. 1107–1114, 1999.

[174] M. Bates, B. Huang, G. T. Dempsey, and X. Zhuang, "Multicolor super-resolution imaging with photo-switchable fluorescent probes," *Science*, vol. 317, no. 5845, pp. 1749–1753, 2007.

[175] A. Waggoner, "Fluorescent labels for proteomics and genomics," *Curr. Opin. Chem. Biol.*, vol. 10, no. 1, pp. 62–66, 2006.

[176] L. D. Lavis and R. T. Raines, "Bright ideas for chemical biology," *ACS Chem. Biol.*, vol. 3, no. 3, pp. 142–155, 2008.

[177] T. Ueno and T. Nagano, "Fluorescent probes for sensing and imaging," *Nat. Methods*, vol. 8, no. 8, pp. 642–645, 2011.

[178] G. Y. Wiederschain, "The Molecular Probes handbook. A guide to fluorescent probes and labeling technologies," *Biochem.*, vol. 76, no. 11, pp. 1276–1276, 2011.

[179] P. G. Wu and L. Brand, “Resonance energy transfer: Methods and applications,” *Anal. Biochem.*, vol. 218, no. 1. pp. 1–13, 1994.

[180] R. M. De Lorimier *et al.*, “Construction of a fluorescent biosensor family,” *Protein Sci.*, vol. 11, no. 11, pp. 2655–2675, 2009.

[181] V. Buschmann, K. D. Weston, and M. Sauer, “Spectroscopic study and evaluation of red-absorbing fluorescent dyes,” *Bioconjug. Chem.*, vol. 14, no. 1, pp. 195–204, 2003.

[182] B. Juskowiak, “Nucleic acid-based fluorescent probes and their analytical potential,” *Anal. Bioanal. Chem.*, vol. 399, no. 9, pp. 3157–3176, 2011.

[183] F. Khakbaz and M. Mahani, “Micro-RNA detection based on fluorescence resonance energy transfer of DNA-carbon quantum dots probes,” *Anal. Biochem.*, vol. 523, pp. 32–38, 2017.

[184] H. Ren *et al.*, “Sandwich DNA Hybridization Fluorescence Resonance Energy-Transfer Strategy for miR-122 Detection by Core-Shell Upconversion Nanoparticles,” *ACS Appl. Mater. Interfaces*, vol. 10, no. 30, pp. 25621–25628, 2018.

[185] H. Zhang *et al.*, “Universal Fluorescence Biosensor Platform Based on Graphene Quantum Dots and Pyrene-Functionalized Molecular Beacons for Detection of MicroRNAs,” *ACS Appl. Mater. Interfaces*, vol. 7, no. 30, pp. 16152–16156, 2015.

[186] A. P. Alivisatos, “Semiconductor Clusters, Quantum Nanocrystals , and Quantum dots,” *Adv. Sci.*, vol. 271, no. 5251, pp. 933–937, 2010.

[187] E. Petryayeva, W. R. Algar, and I. L. Medintz, “Quantum dots in bioanalysis: A review of applications across various platforms for fluorescence spectroscopy and imaging,” *Appl. Spectrosc.*, vol. 67, no. 3, pp. 215–252, 2013.

[188] F. O. R. T. W. Orth, T. Exas, and Q. Aprimer, “Quantum Dots: A Primer.” vol. 56, no. 1, pp. 16A–27A, 2002.

[189] K. F. Chou and A. M. Dennis, “Förster resonance energy transfer between quantum dot donors and quantum dot acceptors,” *Sensors (Switzerland)*, vol. 15, no. 6, pp. 13288–13325, 2015.

[190] W. R. Algar, K. Susumu, J. B. Delehanty, and I. L. Medintz, “Semiconductor quantum dots in bioanalysis: Crossing the valley of death,” *Anal. Chem.*, vol. 83, no. 23, pp. 8826–8837, 2011.

[191] U. Resch-Genger, M. Grabolle, S. Cavaliere-Jaricot, R. Nitschke, and T. Nann, “Quantum dots versus organic dyes as fluorescent labels,” *Nat. Methods*, vol. 5, no. 9, pp. 763–775, 2008.

[192] M. Chern, J. C. Kays, S. Bhuckory, and A. M. Dennis, “Sensing with photoluminescent semiconductor quantum dots,” *Methods Appl. Fluoresc.*, vol. 7, no. 1, p. 12005, 2019.

[193] D. Wu *et al.*, “A two-dimensional molecular beacon for mRNA-activated intelligent cancer theranostics,” *Chem. Sci.*, vol. 6, no. 7, pp. 3839–3844, 2015.

[194] J. Hu, M. H. Liu, and C. Y. Zhang, “Integration of isothermal amplification with quantum dot-based fluorescence resonance energy transfer for simultaneous detection of multiple microRNAs,” *Chem. Sci.*, vol. 9, no. 18, pp. 4258–4267, 2018,.

[195] A. Shahmuradyan, M. Moazami-Goudarzi, F. Kitazume, G. S. Espie, and U. J. Krull, “Paper-based platform for detection by hybridization using intrinsically labeled fluorescent oligonucleotide probes on quantum dots,” *Analyst*, vol. 144, no. 4, pp. 1223–1229, 2019.

[196] S. Huang, H. Qiu, Q. Xiao, C. Huang, W. Su, and B. Hu, “A simple QD-FRET bioprobe for sensitive and specific detection of hepatitis B virus DNA,” *J. Fluoresc.*, vol. 23, no. 5, pp. 1089–1098, 2013.

[197] Y. Wang *et al.*, “Duplex-Specific Nuclease-Amplified Detection of MicroRNA Using Compact Quantum Dot − DNA Conjugates,” *ACS Appl. Mater. Interfaces*, vol. 10, no. 34, pp. 28290-28300, 2018.

[198] N. Hildebrandt, L. J. Charbonnière, M. Beck, R. F. Ziessel, and H. G. Löhmannsröben, “Quantum dots as efficient energy acceptors in a time-resolved fluoroimmunoassay,” *Angew. Chemie - Int. Ed.*, vol. 44, no. 46, pp. 7612–7615, 2005.

[199] X. Qiu, K. D. Wegner, Y. T. Wu, P. M. P. Van Bergen En Henegouwen, T. L. Jennings, and N. Hildebrandt, “Nanobodies and antibodies for duplexed EGFR/HER2 immunoassays using terbium-to-quantum dot FRET,” *Chem. Mater.*, vol. 28, no. 22, pp. 8256–8267, 2016.

[200] X. Qiu and N. Hildebrandt, “Rapid and Multiplexed MicroRNA Diagnostic Assay Using Quantum Dot-Based Förster Resonance Energy Transfer,” *ACS Nano*, vol. 9, no. 8, pp. 8449–8457, 2015.

[201] D. Gustafson, K. Tyryshkin, and N. Renwick, “microRNA-guided diagnostics in clinical samples,” *Best Pract. Res. Clin. Endocrinol. Metab.*, vol. 30, no. 5, pp. 563–575, 2016.

[202] A. Kappel and A. Keller, “MiRNA assays in the clinical laboratory: Workflow, detection technologies and automation aspects,” *Clin. Chem. Lab. Med.*, vol. 55, no. 5, pp. 636–647, 2017.

[203] K. W. Witwer, “Circulating MicroRNA biomarker studies: Pitfalls and potential solutions,” *Clin. Chem.*, vol. 61, no. 1, pp. 56–63, 2015.

[204] S. A. Bustin *et al.*, “The MIQE guidelines: Minimum information for publication of quantitative real-time PCR experiments,” *Clin. Chem.*, vol. 55, no. 4, pp. 611–622, 2009.

[205] P. Verma, R. K. Pandey, P. Prajapati, and V. K. Prajapati, “Circulating microRNAs: Potential and emerging biomarkers for diagnosis of human infectious diseases,” *Front. Microbiol.*, vol. 7, no. AUG, pp. 1–7, 2016.

[206] J. E. Zhang, “microRNA: Emerging biomarkers in human disease and profiling challenges,” *Biochem.*, vol. 38, no. 2, pp. 26–29, 2016.

[207] P. Shah *et al.*, “Locking-to-unlocking system is an efficient strategy to design DNA/silver nanoclusters (AgNCs) probe for human miRNAs,” Nucleic Acids Res., vol. 44, no. 6, 2015.

[208] F. Xu *et al.*, “Ultrasensitive and Multiple Disease-Related MicroRNA Detection Based on Tetrahedral DNA Nanostructures and Duplex-Specific Nuclease-Assisted Signal Amplification,” *ACS Appl. Mater. Interfaces*, vol. 8, no. 49, pp. 33499–33505, 2016.

[209] C. Hong, A. Baek, S. S. Hah, W. Jung, and D. E. Kim, “Fluorometric Detection of MicroRNA Using Isothermal Gene Amplification and Graphene Oxide,” *Anal. Chem.*, vol. 88, no. 6, pp. 2999–3003, 2016.

[210] Y. Zhao, F. Chen, Q. Li, L. Wang, and C. Fan, “Isothermal Amplification of Nucleic Acids,” *Chem. Rev.*, vol. 115, no. 22, pp. 12491–12545, 2015.

[211] H. X. Jiang, Z. Z. Liang, Y. H. Ma, D. M. Kong, and Z. Y. Hong, “G-quadruplex fluorescent probe-mediated real-time rolling circle amplification strategy for highly sensitive microRNA detection,” *Anal. Chim. Acta*, vol. 943, pp. 114–122, 2016.

[212] X. Wu, S. Zhu, P. Huang, and Y. Chen, "Highly specific quantification of microRNA by coupling probe-rolling circle amplification and Förster resonance energy transfer," *Anal. Biochem.*, vol. 502, pp. 16–23, 2016.

[213] X. Zhang, H. Liu, R. Li, N. Zhang, Y. Xiong, and S. Niu, "Chemiluminescence detection of DNA/microRNA based on cation-exchange of CuS nanoparticles and rolling circle amplification," *Chem. Commun.*, vol. 51, no. 32, pp. 6952–6955, 2015.

[214] J. K. Chan *et al.*, "The inhibition of miR-21 promotes apoptosis and chemosensitivity in ovarian cancer," *Gynecol. Oncol.*, vol. 132, no. 3, pp. 739–744, 2014.

[215] C. Zhang *et al.*, "MiR-21: A gene of dual regulation in breast cancer," *Int. J. Oncol.*, vol. 48, no. 1, pp. 161–172, 2016.

[216] K. D. Taganov, M. P. Boldin, K. J. Chang, and D. Baltimore, "NF-κB-dependent induction of microRNA miR-146, an inhibitor targeted to signaling proteins of innate immune responses," *PNAS*, vol. 103, no. 33, pp. 12481–12486, 2006.

[217] X. Qiu, J. Guo, Z. Jin, A. Petreto, I. L. Medintz, and N. Hildebrandt, "Multiplexed Nucleic Acid Hybridization Assays Using Single-FRET-Pair Distance-Tuning," *Small*, vol. 13, no. 25, pp. 1–6, 2017.

[218] A. Lagunavicius, Z. Kiveryte, V. Zimbaite-Ruskuliene, T. Radzvilavicius and A. Janulaitis, "Duality of polynucleotide substrates for Phi29 DNA polymerase: 3'→5' RNase activity of the enzyme," *RNA*, vol. 14, pp. 503–513, 2008.

[219] P. Mestdagh *et al.*, "Evaluation of quantitative miRNA expression platforms in the microRNA quality control (miRQC) study," *Nat. Methods*, vol. 11, no. 8, pp. 809–815, 2014.

[220] C. P. Bracken, H. S. Scott, and G. J. Goodall, “A network-biology perspective of microRNA function and dysfunction in cancer,” *Nat. Rev. Genet.*, vol. 17, no. 12, pp. 719–732, 2016.

[221] Y. Fan, S. Wang, and F. Zhang, “Optical Multiplexed Bioassays for Improved Biomedical Diagnostics,” *Angew. Chemie - Int. Ed.*, vol. 58, no. 38, pp. 13208–13219, 2019.

[222] F. L. Guest, P. C. Guest, and D. Martins-De-Souza, “The emergence of point-of-care blood-based biomarker testing for psychiatric disorders: Enabling personalized medicine,” *Biomark. Med.*, vol. 10, no. 4, pp. 431–443, 2016.

[223] M. Kaufmann, M. Keppens, and E. D. Blair, “A perspective analysis: Companion diagnostics: An evolving paradigm in 21st century healthcare,” *Per. Med.*, vol. 12, no. 4, pp. 389–402, 2015.

[224] R. Duncan, M. Kourout, E. Grigorenko, C. Fisher, and M. Dong, “Advances in multiplex nucleic acid diagnostics for blood-borne pathogens: Promises and pitfalls,” *Expert Rev. Mol. Diagn.*, vol. 16, no. 1, pp. 83–95, 2016.

[225] B. Hötzer, I. L. Medintz, and N. Hildebrandt, “Fluorescence in nanobiotechnology: Sophisticated fluorophores for novel applications,” *Small*, vol. 8, no. 15, pp. 2297–2326, 2012.

[226] X. Qiu and N. Hildebrandt, “A clinical role for Förster resonance energy transfer in molecular diagnostics of disease,” *Expert Rev. Mol. Diagn.*, vol. 19, no. 9, pp. 767–771, 2019.

[227] J. Guo, C. Mingoes, X. Qiu, and N. Hildebrandt, “Simple, Amplified, and Multiplexed Detection of MicroRNAs Using Time-Gated FRET and Hybridization Chain Reaction,” *Anal. Chem.*, vol. 91, no. 4, pp. 3101–3109, 2019.

[228] miRCancer - microRNA Cancer Association Database http://mircancer.ecu.edu/.

[229] M. Mandelkern, J. G. Elias, D. Eden, and D. M. Crothers, "The dimensions of DNA in solution," *J. Mol. Biol.*, vol. 152, no. 1, pp. 153–161, 1981.

[230] B. Xie, Q. Ding, H. Han, and D. Wu, "MiRCancer: A microRNA-cancer association database constructed by text mining on literature," *Bioinformatics*, vol. 29, no. 5, pp. 638–644, 2013.

[231] X. Zhang *et al.*, "Ligation-promoted hyperbranched rolling circle amplification enables ultrasensitive detection of microRNA in clinical specimens," *Sensors Actuators, B Chem.*, vol. 277, no. September, pp. 634–639, 2018.

[232] B. Zou, Y. Ma, H. Wu, and G. Zhou, "Signal amplification by rolling circle amplification on universal flaps yielded from target-specific invasive reaction," *Analyst*, vol. 137, no. 3, pp. 729–734, 2012.

[233] Y. Zhang, L. Chen, K. Hsieh, and T. H. Wang, "Ratiometric Fluorescence Coding for Multiplex Nucleic Acid Amplification Testing," *Anal. Chem.*, vol. 90, no. 20, pp. 12180–12186, 2018.

[234] X. H. Li *et al.*, "Hyperbranched rolling circle amplification (HRCA)-based fluorescence biosensor for ultrasensitive and specific detection of single-nucleotide polymorphism genotyping associated with the therapy of chronic hepatitis B virus infection," *Talanta*, vol. 191, no. July 2018.

[235] L. Zhang *et al.*, "Ultrasensitive biosensing of low abundance BRAF V600E mutation in real samples by coupling dual padlock-gap-ligase chain reaction with hyperbranched rolling circle amplification," *Sensors Actuators, B Chem.*, vol. 287, no. January, pp. 111–117, 2019.

[236] H. Shi, X. Mao, X. Chen, Z. Wang, K. Wang, and X. Zhu, “The analysis of proteins and small molecules based on sterically tunable nucleic acid hyperbranched rolling circle amplification,” *Biosens. Bioelectron.*, vol. 91, no. October 2016, pp. 136–142, 2017.

[237] X. Zhu *et al.*, “An ultrasensitive aptameric sensor for proteins based on hyperbranched rolling circle amplification,” *Chem. Commun.*, vol. 49, no. 86, pp. 10115–10117, 2013.

[238] J. Chen *et al.*, “Highly sensitive fluorescent sensor for mercury based on hyperbranched rolling circle amplification,” *Analyst*, vol. 140, no. 3, pp. 907–911, 2015.

[239] Y. Zhang *et al.*, “Fluorescence aptasensor for Ochratoxin A in food samples based on hyperbranched rolling circle amplification,” *Anal. Methods*, vol. 7, no. 15, pp. 6109–6113, 2015.

[240] P. M. Lizardi, X. Huang, Z. Zhu, P. Bray-Ward, D. C. Thomas, and D. C. Ward, “Mutation detection and single-molecule counting using isothermal rolling-circle amplification,” *Nat. Genet.*, vol. 19, no. 3, pp. 225–232, 1998.

9. Résumé en français

Les microARNs (miARNs) sont impliqués dans pratiquement tous les processus physiologiques, y compris la différenciation et la prolifération, le métabolisme, l'hémostase, l'apoptose ou l'inflammation. À ce jour, plus de 30,000 miARNs ont été découverts, dont plus de 2,500 peuvent être trouvés chez l'homme. La découverte de nombreux types miARNs circulants (dans les fluides biologiques des patients, par exemple, le sérum, le plasma, l'urine, le liquide céphalorachidien, *etc.*) spécifiques aux cancers (sein, colorectal, œsophagien, gastrique, hépatique, pulmonaire, ovarien, pancréatique, *etc.*), ainsi que de nombreuses autres maladies (maladies infectieuses, troubles immunologiques, maladies cardiovasculaires, neurologiques, *etc.*), ont fortement stimulé la mise en œuvre des miARNs comme biomarqueurs de nouvelle génération pour la prédiction des maladies, la réponse au traitement ou la prédiction de la progression. D'après un nouveau rapport de BCC Research *Inc.*, le marché mondial des outils de recherche sur les miARNs, services, diagnostics et découverte de médicaments devraient atteindre près de 1.4 milliard de dollars en 2021 à un taux de croissance annuel composé de 10.5% pour 2016-2021. Compte tenu de la récente découverte des miARNs circulants, le secteur diagnostic de ce marché global est encore extrêmement petit, démontrant le besoin urgent de développer des tests de diagnostics miARNs cliniquement approuvés. Malgré leurs séquences courtes combinées à de fortes similitudes de séquence entre différents miARNs, de nombreuses types de technologies ont été utilisées pour leur détection. Les plus couramment utilisées sont la réaction en chaîne par polymérase quantitative à transcription inverse (RT-qPCR), microarray, séquençage à haut débit (NGS), hybridation in situ (ISH), northern blotting (NB). Cependant, les principales limitations sont la faible sensibilité (microarray, NB) et le débit (ISH, NB, RT-qPCR), les coûts (microarray, NGS), le manque de quantification absolue (microarray, NGS) et le multiplexage à partir d'un seul échantillon (RT-qPCR, NGS), coûteux en temps et difficultés associées à des résultats comparables sur différentes plates-formes. L'amplification isotherme est devenue une méthode puissante pour les dosages de miARNs très rapides très rapides, spécifiques et sensibles, qui possède

également la compatibilité avec des plateformes de détection diverse, telles que la fluorescence, l'électrochimie et la colorimétrie.

Le but de cette thèse est d'aborder de nouvelles voies d'outils de diagnostic de miARNs, en prenant la simplicité d'un immunodosage homogène, la capacité de multiplexage de microarrays, la sensibilité de RT-qPCR et la capacité de débit de NGS dans un seul outil de diagnostic. Le concept consiste à combiner la polyvalence et la capacité de multiplexage des complexes luminescents de Tb (LTC) basés sur la mesure du transfert d'énergie par résonance de type Förster à sélection temporelle (TG-FRET) avec la technologie d'amplification isotherme pour concevoir des biocapteurs miARNs ultra-sensibles et/ou multiplexés. Les LTC utilisés comme donneur de transfert d'énergie et possédant des avantages uniques pour la détection multiplexée en raison de leurs pics d'émission multiples, nets et distincts, ainsi que de longues durées de vie de leur état excité par rapport aux colorants organiques et aux points quantiques (QD). Les colorants organiques peuvent être utilisés dans des systèmes biologiques à faible toxicité. Ils ont été les fluorophores les plus utilisés dans la technique de FRET, et en combinaison avec les LTC en tant que donneurs, le développement de biocapteurs multiplexées sont réalisable basées sur les LTCs-colorants FRET. Notamment, une correction appropriée de l'interférence spectrale doit être prise pour le multiplexage spectral en raison des larges profils d'émission des fluorophores organiques. Bien que les QD aient des avantages uniques par rapport aux colorants organiques dans les systèmes de FRET, en particulier dans les tests FRET basés sur les donneurs de LTC, les QD ont un meilleur chevauchement spectral ainsi qu'une plus grande distance de Förster avec les LTC en raison de leur absorption très large et d'un coefficient d'extinction molaire et rendement quantique extrêmement élevé. Les bandes d'émission étroites et ajustables en taille font que les QD sont d'excellents candidats d'accepteurs de FRET pour le multiplexage. Les mesures traditionnelles de FRET sont troublées par la courte durée de vie (dans la gamme du ns) et la fluorescence de fond élevée des tampons ou des échantillons. En utilisant TG-FRET, en particulier en utilisant des LTC à longue durée de vie comme donneurs et des colorants/QD à courte durée de vie comme accepteurs, lors de l'excitation pulsée d'un échantillon, en collectant la durée de vie de la

photoluminescence (PL) dans des fenêtres temporelles beaucoup plus longue que la décroissance naturelle des colorants/QD, mais toujours pendant la durée de vie de la décroissance des LLC, l'excitation directe des colorants/QD accepteurs et toute autofluorescence peuvent être efficacement supprimées, ce qui simplifie considérablement analyse du système.

Cette thèse peut être divisée en huit chapitres. Après l'introduction, le contexte, trois études individuelles sont présentées, puis complétées par un résumé et des perspectives, une annexe et une bibliographie. Chaque étude est corroborée par l'introduction, le matériel et les méthodes, les résultats et la discussion, et la conclusion.

Dans la première étude, je présente un essai de détection de miARNs utilisant une amplification enzymatique à cercle circulaire (RCA) LTCs-à-colorant TG-FRET. Ma contribution à cette étude a été l'investigation des échantillons cliniques, en particulier, la préparation d'échantillons, les expériences RCA-FRET, les expériences RT-qPCR et l'analyse des données. Dr. Jiajia Guo a également contribué aux travaux expérimentaux et Dr. Xue Qiu a conçu les études et rédigé le manuscrit. Tous les auteurs ont contribué à l'édition et à la rédaction du manuscrit et ont approuvé sa version finale à la revue (X. Qiu, J. Xu, J. Guo, A. Yahia-Ammar, N.-I. Kapetanakis, I. Duroux-Richard, J.J. Unterluggauer, N. Golob-Schwarzl, C. Regeard, C. Uzan, S. Gouy, M. DuBow, J. Haybaeck, F. Apparailly, P. Busson, and N. Hildebrandt. *Chemical Science* **2018**, 9, 8046-8055. Troisième article de la Section **List of publications**). La combinaison de RCA avec TG-FRET entre les donneurs de LTC et les accepteurs Cy5.5 a abouti à une seule spécificité et sensibilité de la variante nucléotidique avec une limite de détection (LOD) jusqu'à 4.2 ± 0.5 attomole (30 ± 3 fM) pour miR-21, 6.8 ± 0.8 attomole (48 ± 5 fM) pour miR-132 et 14 ± 2 attomole (99 ± 10 fM) pour le miR-146a. La quantification du miR-21 à partir des tissus humains et des échantillons de plasma a révélé la pertinence pour le diagnostic du cancer du sein et de l'ovaire. Cette étude a démontré la large applicabilité à différents miARNs et à d'autres types d'échantillons cliniques. La comparaison directe avec l'étalon ou RT-qPCR a montré les avantages du TG-FRET amplifié en ce qui concerne la précision et la spécificité lors de la quantification de faibles concentrations de miARN comme requis pour les applications

diagnostiques. La mise en œuvre efficace du RCA et du TG-FRET dans une méthode de détection d'acide nucléique simple peut considérablement faire avancer les possibilités de diagnostic et de recherche sur le cancer à base de miARN.

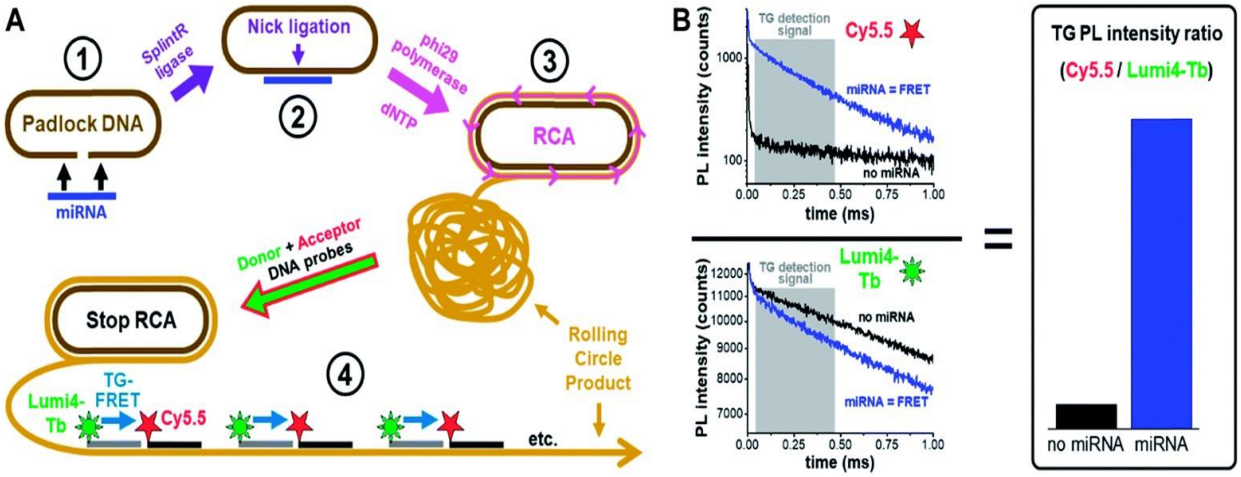

Figure 1.1 Représentation schématique du test de détection de miARN utilisant des LTCs à colorant TG-FRET amplifiés par RCA.

La deuxième étude présente un essai de multiplexage temporel pour la détection de miARN utilisant des LTCs-to-dye TG-FRET amplifiés par enzyme catalytique sans enzyme (CHA). Ma contribution à cette étude a été la conception d'étude, la réalisation d'expériences, l'analyse des données et la rédaction du manuscrit. Dr. Jiajia Guo et Dr. Xue Qiu ont également contribué à la conception d'étude. Tous les auteurs ont contribué à l'édition et à la rédaction du manuscrit et ont approuvé sa version finale à la revue (J. Xu, J. Guo, N. Golob-Schwarzl, J. Haybaeck, X. Qiu, and N. Hildebrandt. *ACS Sensors* **2020**, (accepted), DOI: 10.1021/acssensors.0c00432. Premier article de la Section **List of publications**). L'implémentation de TG-FRET dans CHA peut être utilisée pour la quantification simultanée de deux miARN (miR-21 et miR-20a) avec une seule mesure à partir d'extraits d'ARNs totaux de tissus humains. Une seule paire de FRET LTCs-à-Cy5.5 a été conjuguée à deux distances spécifiques dans les sondes en épingle à cheveux CHA spécifiques aux cibles, de sorte que chaque miARN a entraîné des PL amplifiées distinctes qui pouvaient être distinguées et quantifiées par détection d'intensité TG PL. L'amplification sans enzyme

dans un format de dosage sans séparation et l'absence d'autofluorescence permettait une détection simple, spécifique et sensible avec une LOD jusqu'à 380 ± 40 attomoles (2.7 ± 0.3 pM) pour miR-21 et 250 ± 60 attomoles (1.8 ± 0.4 pM) pour miR-20a. Une quantification fiable en duplex des deux miARNs à de faibles concentrations picomolaires a été confirmée par l'analyse des extraits d'ARN totaux de différents tissus du côlon et du rectum avec CHA-TG-FRET et RT-qPCR à cible unique et double pour comparaison. Ces tests de biomarqueurs miARN rapides, simples et multiplexés présentent une méthode efficace pour les diagnostics cliniques.

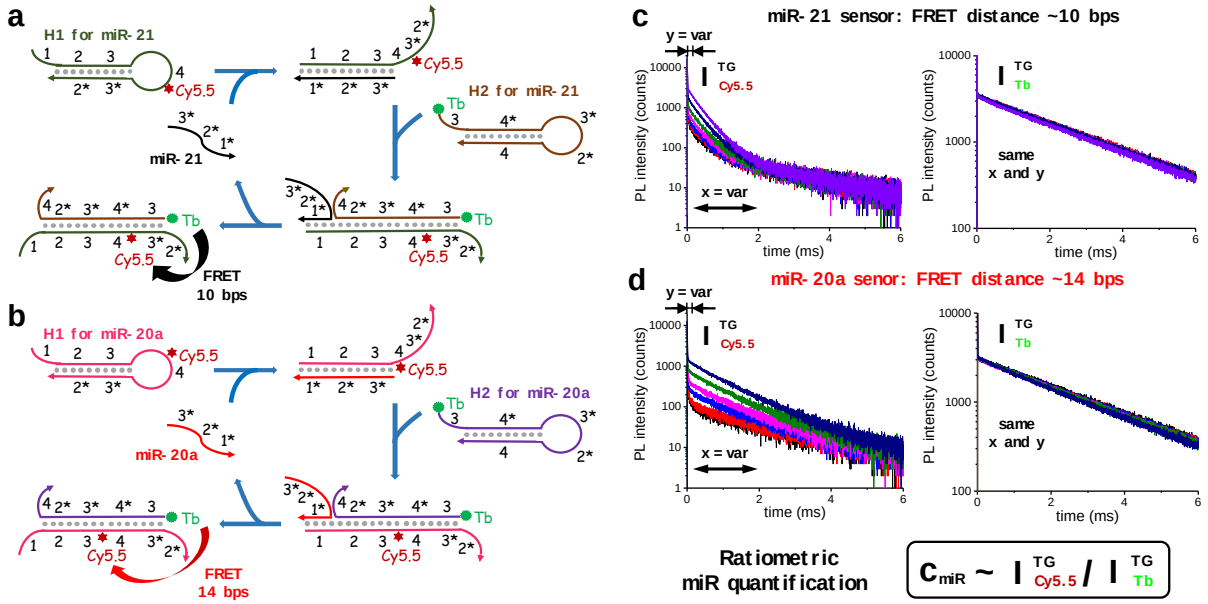

Figure 1.2 Représentation schématique pour l'analyse de détection des miARN multiplexés (miR-21 et miR-20a) à l'aide de LTC à colorant TG-FRET amplifiés par CHA.

Dans la troisième étude, j'ai étudié la détection de miARN utilisant une amplification enzymatique à cercle roulant hyperbranché (HRCA) LTCs-to-QD TG-FRET. Ma contribution à cette étude a été la conception d'étude, la réalisation d'expériences et l'analyse des données. Dr. Xue Qiu a également contribué à la conception d'étude. Le manuscrit est en préparation. En intégrant la mesure de TG dépourvue d'autofluorescence dans HRCA avec une efficacité d'amplification exponentielle, elle offre des avantages de haute

sensibilité avec une limite de détection de 11 ± 4 attomole (80 ± 30 fM) et sélectivité vis-à-vis du miR-21 cible dans un bruit de fond extrêmement faible, format de test en une seule étape rapide et simple. La réaction HRCA amorcée et amorcée par une cible peut générer une grande quantité d'ADN simple brin de différentes longueurs (produit HRCA). En s'hybridant avec des sondes d'ADN reporter marquées au Tb et des sondes d'ADN adaptatrices qui sont à la surface du QD via l'interaction biotine et streptavidine, les complexes QD-ADN-LTC pourraient se former, induisant la distance raccourcie entre les LTC, résultant en LTCs-à-QD FRET. En outre, le test proposé montre un grand potentiel pour une large applicabilité à différents miARNs et capacité de multiplexage, démontrant qu'il peut être une alternative prometteuse aux approches actuelles de diagnostic de miARNs.

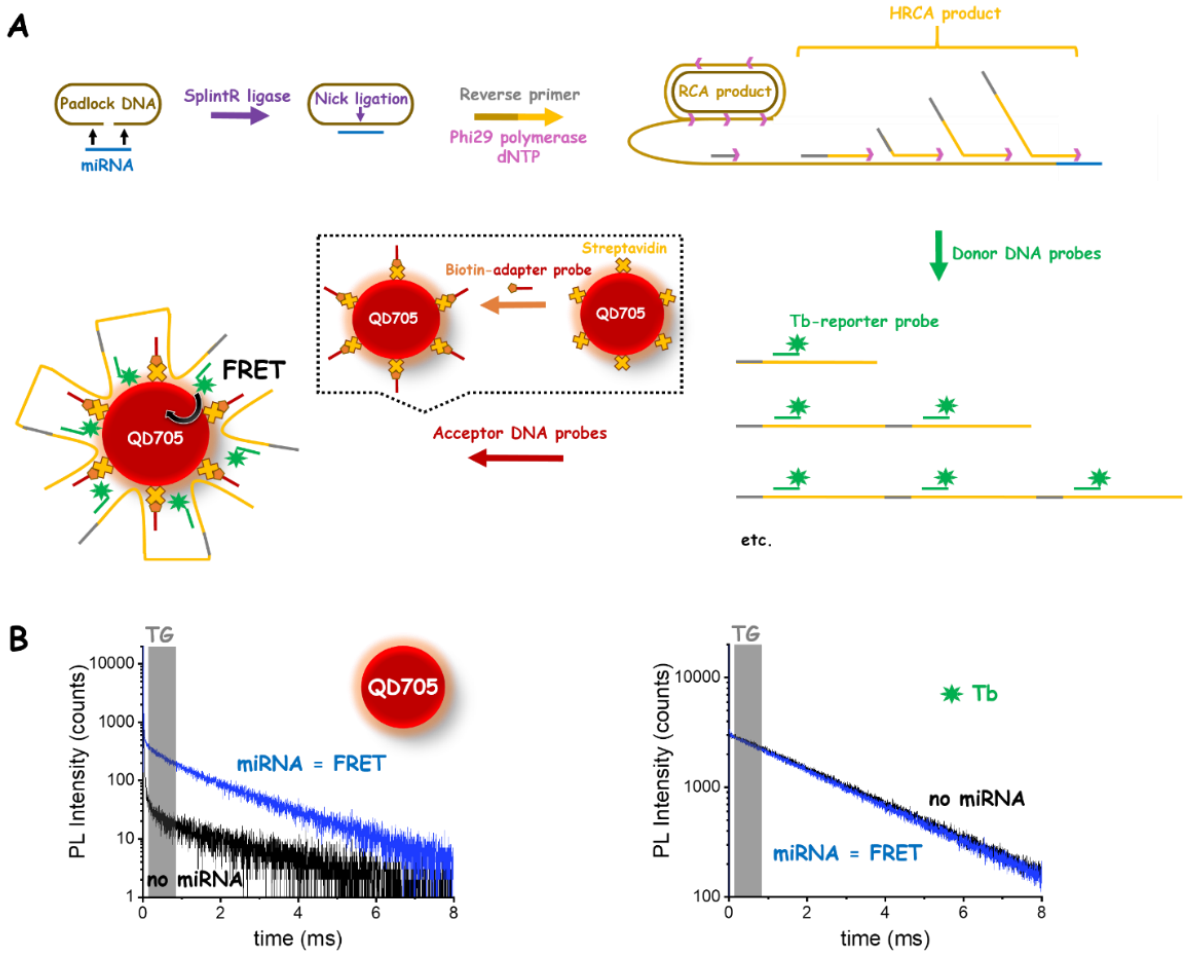

Figure 1.3 Représentation schématique pour l'analyse de détection de miARN en utilisant des LTC amplifiés HRCA en TG-FRET QD.

université PARIS-SACLAY

ÉCOLE DOCTORALE
Physique et ingénierie : Electrons, Photons, Sciences du vivant (EOBE)

Titre : Quantification sensible et mutiplexée des microARNs en utilisant le transfert d'energie par résonance de type Förster amplifié et résolu en temps

Mots clés : FRET, miARN, complexe de lanthanide, amplification isotherme, spectroscopie résolue en temps

Résumé : En tant que biomarqueurs de nouvelle génération, les microARNs sont associés à de nombreux cancers et maladies, ce qui a conduit à une forte demande pour le développement de méthodes cliniques de diagnostic des microARNs. Les technologies d'amplification isotherme, telles que l'amplification en cercle roulant et l'assemblage catalytique en épingle à cheveux, sont devenues des méthodes puissantes pour les dosages très rapides, spécifiques et sensibles des microARNs. Cette thèse se concentre sur le développement de biocapteurs de microARNs basés sur les technologies d'amplification isotherme et le transfert d'énergie par résonance de type Förster résolu en temps des complexes de lanthanide aux colorants organiques ou aux points quantiques. Les biocapteurs de microARNs amplifiés proposés ont des limites de détection très basses et sont utilisables dans des échantillons cliniques humains, révélant avec succès leurs pertinence pour le diagnostic du cancer. Comme la détection simultanée de plusieurs microARNs est très demandée, la détection temporelle multiplexée de microARNs est également effectuée basée sur les de durées de vie à l'état excité distinctes des complexes Tb et des colorants. De plus, le nanocapteur microARN amplifié basé sur des points Tb à quantique FRET, a démontré la possibilité d'une détection spectrale multiplexée de microARNs avec une sensibilité et une sélectivité élevées.

Title : Sensitive and mutiplexed microRNA quantification using amplified time-gated Förster resonance energy transfer

Keywords : FRET, miRNA, lanthanide complex, isothermal amplification, time-resolved spectroscopy

Abstract : As new generation of biomarkers, microRNAs are associated with many cancers and diseases, which has led to a great demand for developing clinical miRNA diagnostic methods. Isothermal amplification technologies, such as rolling circle amplification and catalytic hairpin assembly, have emerged as powerful methods for highly rapid, specific and sensitive microRNA assays. This thesis focuses on developing microRNA biosensors based on isothermal amplification technologies and time-resolved Förster resonance energy transfer from lanthanide complexes to organic dyes or quantum dots. The proposed amplified microRNA biosensors have very low limits of detections, and are applied to human clinical samples, successfully revealing the relevance for cancer diagnostics. As simultaneous detection of multiple microRNAs is highly demanded, temporal multiplexed detection of microRNAs is also realized based on distinguishable excited-state lifetimes of Tb complexes and dyes. Moreover, the amplified microRNA nanosensor based on Tb-to-quantum dots FRET demonstrated the possibility of spectral multiplexed detection of microRNAs with high sensitivity and selectivity.

Université Paris-Saclay
Espace Technologique / Immeuble Discovery
Route de l'Orme aux Merisiers RD 128 / 91190 Saint-Aubin, France